
Electronic Thesis and Dissertation Repository

5-30-2022 10:30 AM

Performance of Fouled Railroad Superstructure Subjected to Traversing Heavy Haul Trains

Majid Kh Touqan, *The University of Western Ontario*

Supervisor: El Naggari, M. Hesham, *The University of Western Ontario*

Co-Supervisor: Stark, Timothy D., *University of Illinois at Urbana Champaign*

A thesis submitted in partial fulfillment of the requirements for the Doctor of Philosophy degree in Civil and Environmental Engineering

© Majid Kh Touqan 2022

Follow this and additional works at: <https://ir.lib.uwo.ca/etd>



Part of the [Civil Engineering Commons](#), and the [Geotechnical Engineering Commons](#)

Recommended Citation

Kh Touqan, Majid, "Performance of Fouled Railroad Superstructure Subjected to Traversing Heavy Haul Trains" (2022). *Electronic Thesis and Dissertation Repository*. 8590.
<https://ir.lib.uwo.ca/etd/8590>

This Dissertation/Thesis is brought to you for free and open access by Scholarship@Western. It has been accepted for inclusion in Electronic Thesis and Dissertation Repository by an authorized administrator of Scholarship@Western. For more information, please contact wlsadmin@uwo.ca.

Abstract

Railway transportation offers capacity, efficiency, and safety to serve the needs of modern societies for moving freight and people. Therefore, the sustainability and safety of railroad infrastructure are of paramount importance for securing transportation needs. Freight train passby loads increase the surface deformation of railroad substructure due to cumulative plastic strains, which lead to surface deviation of the railroad tracks. Correspondingly, railroad maintenance is necessary to sustain track geometry alignment and to prevent deterioration of the sub-structure over time, which can increase operating costs significantly. Therefore, this thesis evaluates the performance of fouled railroad superstructure through laboratory testing of fouled sub-structure material, field monitoring of fouled track section at the test site and finite element analysis of the fouled track performance.

First, isotropically consolidated drained cyclic triaxial tests were conducted on fouled sub-ballast retrieved from the test site. Test results were used to assess the material shear stiffness during the loading cycles. Operational speed limits were deduced from the stress-strain behavior of the fouled sub-ballast to prolong the service life of the fouled foundation bed. Next, railroad superstructure performance due to track fouling was assessed through a field monitoring program. The normalized maximum rail-tie tensile force was employed to analyze the uplift resistance of a CWR section at the cross-tie. Results indicate that the tie-load ratio may misrepresent the superstructure efficiency in fouled ballast beds. Alternatively, the range of influence of wheels along with the uplift ratio may be used to assess fouled railroad performance using the proposed empirical models. Measured accelerations during the passage of various trains were analyzed in time and frequency domains. Train velocity guidelines are provided to minimize train-induced vibrations in the fouled tracks. Finally, a validated dynamic two-dimensional finite element model was developed to investigate the effect of train velocity on the generated positive and negative excess pore water pressures using loading time histories considering different train velocities. Results demonstrate that positive excess porewater pressure developed in the sub-structure due to cyclic loading. Undrained conditions prevailed in the sub-grade and sub-ballast. Capillary fringes were noticed to form in the sub-ballast layer.

Keywords

Cyclic triaxial tests, fouled sub-ballast, static triaxial tests, train loading conditions, railroad substructure, uplift resistance, concrete monoblock cross-tie, static track stiffness, dynamic amplification, acceleration response, supported cross-ties vibration, voided cross-tie vibration, dynamic 2D FEM analysis, train velocity, excess pore water pressures, undrained conditions.

Summary for Lay Audience

A railroad is comprised of two main components: the track and foundation. A typical modern railway track consists of the rail, fasteners, and cross-ties. The foundation bed consists of ballast, sub-ballast, and native soil. The rail made from steel carries train wheels and transmits train loads to the cross-ties. Fasteners are made from steel and hold the rail together with the cross-ties. The cross-ties (made from concrete or timber) provide support and transmit the applied train loads to the track foundation. The ballast is comprised of crushed stone and its main functions is to support train loads and drain water from the track. The sub-ballast (smaller diameter particles) acts as a diaphragm between the ballast and the native soil. The native soil is the local soil type present on the ground surface on top of which the railroad is constructed. Track fouling is a railroad condition where the ballast gets contaminated with fines (sands, silts, and clays). Progressive use of fouled track by traversing trains causes mud (fines) to be pumped and a gap to exist beneath the cross-ties a phenomenon called the voided cross-tie.

Previous studies have highlighted the relationship between increased train speed and the rate of deterioration of the foundation bed. However, these studies did not provide an insight into the extent of deterioration of railroad foundation due to heavy haul trains travelling at high speeds. Therefore, the current study has provided an understanding of the behaviour of fouled sub-ballast under train loading and proposed guidelines to operators about the train speed limits in fouled railroad segments. In addition, the current study investigated the behaviour of the track through a 6-month duration field monitoring and quantified the deflection of the railroad track due to trains travelling in adverse environmental conditions. Recommendations were provided to manage trains travelling on fouled railroad segments in critical weather conditions. Moreover, the current study has placed special emphasis on assessing the response of voided cross-ties compared with supported cross-ties. The vibration of cross-ties in the fouled segment of the track is compared with the cross-tie vibration at the clean section to elucidate the effect of ballast fouling. Lastly, using software, the current study provided a critical review focused on the effect of mud pumping in railroad foundation and the magnitudes of water pressure due to actual measured wheel loads.

Co-Authorship Statement

Significant sections of this thesis were submitted for publication to peer-reviewed technical journals. The candidate conducted all experiments, instrumented the railroad track, and analyzed the data and authored the initial versions of all papers listed below. His thesis advisors revised the documents and contributed to the development of the final version of these papers:

- (1) Touqan, M., Ahmed, A., El Naggar, M.H., & Stark, T.D. (2020). Static and cyclic characterization of fouled railroad sub-ballast layer behaviour. *Journal of Soil Dynamics and Earthquake Engineering*, 137, 106293, (Published).
- (2) Touqan, M., El Naggar, M. H., & Stark, T. D. (2022). In-situ performance assessment of track superstructure on fouled railroad. *Transportation Geotechnics*, 32, 100695, (Published)
- (3) Touqan, M., El Naggar, M.H., & Stark, T.D. (2022). In-situ Assessment of Track Borne Vibrations Induced by Freight Trains. *Journal of Soil Dynamics and Earthquake Engineering*, (Under review).
- (4) Touqan, M., El Naggar, M.H., & Stark, T.D. (2022). Evaluation of cyclically-induced track suction and excess pore water pressure in ballasted tracks using Finite Element Modelling, (to be submitted).

Acknowledgments

I would like to convey my sincere appreciation and heartfelt gratitude to my supervisors Dr. M. Hesham El Naggat and Dr. Timothy D. Stark, both of them provided nonstop support and continuous encouragement during the course of this research. Without their advice and knowledge, I would not have been able to progress through this research. Thank you both for your guidance and patience in steering this research in the correct direction. Also, I would like to thank Dr. Aly Ahmed for his kindness and advice throughout my laboratory testing work. I am likewise thankful to my supervisory committee members, Dr. Tim Newson, and Dr. Julie Shang, for their important comments to improve my research. I'll never forget the support and generosity from the Lardner family, Dr. Douglas Muzyka and the GRC at Western for honouring me with several prestigious awards during my research. A special note of thanks is given to the Burlington Northern Santa Fe (BNSF) Railway Company for their cooperation all the way through the progress of this study.

My utmost gratitude goes to my parents, Omar Touqan and Saheer Bakeer for their endless love, infinite support, and boundless inspiration. I will always be in your debt. I am grateful to my brother Karim Touqan, with his support my long journey felt shorter, and with his motivation I was able to continue. A kind thanks goes to my parents-in-law, Jafar Sadeddin and Liqa Sadeddin for their kind words of encouragement and kindness. I wish to express my sincere gratitude to my love and soulmate Farah Sadeddin, my daughter Saheer Touqan Jr. and my son Omar Touqan Jr. for their love, understanding and patience throughout this work. Without their encouragement and support this work would not have been completed. I am always thankful to God for their presence in my life.

Table of Contents

Performance of Fouled Railroad Superstructure Subjected to Traversing Heavy Haul Trains	I
Abstract	III
Summary for Lay Audience.....	V
Co-Authorship Statement.....	VI
Acknowledgments	VII
Table of Contents	VIII
List of Tables	XIII
List of Figures.....	XIV
Glossary	XIX
Chapter 1.....	1
1 Introduction.....	1
1.1 Preamble.....	1
1.2 Motivation and Problem Statement.....	3
1.3 Objectives and Scope	4
1.4 Highlights of Research Contributions	6
1.4.1 Static and Cyclic Characterization of Fouled Railroad Sub-Ballast Layer Behaviour	6
1.4.2 In-situ Performance Assessment of Track Superstructure on Fouled Railroad.....	7

1.4.3	Quantification of Cross-tie Vibrations and the Effect of Static track stiffness.....	7
1.4.4	Finite Element Modelling of Fouled Track Using Actual Loading Simulations.....	8
1.5	Research Methods and Thesis Organization	8
Chapter 2	11
2	Static and Cyclic Characterization of Fouled Railroad Sub-Ballast Layer Behaviour	11
2.1	General	11
2.2	Literature Review	11
2.3	Objective and Scope of Work	16
2.4	Materials and Methods	17
2.4.1	Parkville-Missouri Site Soil Profile	17
2.4.2	Laboratory Testing Program	19
2.4.3	Test Apparatus	20
2.4.4	Sample Preparation	22
2.4.5	Applied Static Strain-Controlled Loading	24
2.4.6	Applied Cyclic Load-Controlled Loading	24
2.5	Discussion of Static Triaxial Results	26
2.6	Analysis of Results from Laboratory Tests.....	29
2.6.1	Cyclic Axial and Volumetric Strains	29
2.6.2	Consolidation Parameters of Fouled Sub-ballast.....	33

2.6.3 Shear Modulus Corresponding to Shear Wave Velocity Measurements.....	35
2.6.4 Shear Modulus Corresponding to Cyclic Loading.....	37
2.6.5 Damping Ratio.....	40
2.7 Practical Implications.....	43
2.8 Summary.....	44
Chapter 3.....	47
3 In-situ Performance Assessment of Track Superstructure on Fouled Railroad	47
3.1 General.....	47
3.2 Objectives and Scope of Work.....	52
3.3 Site Profile and Track Instrumentation.....	53
3.3.1 Site and Soil Profile.....	53
3.3.2 Instrumentation.....	56
3.4 Local Environmental Conditions.....	62
3.4.1 Temperature Profile.....	62
3.4.2 Precipitation/Snowfall effect on Soil Moisture Regime.....	63
3.5 Fouled Track Superstructure System Response.....	67
3.5.1 Wheel load Characterization.....	67
3.5.2 Estimating Cross-Tie Reaction.....	68
3.5.3 Rail Bending Forces at the Neutral Axis.....	70

3.5.4 Effect of Fouled Static Track Stiffness on Longitudinal Range of Influence of Distant Wheel Loads.....	79
3.5.5 Statistical Analysis and Empirical Solution.....	82
3.5.6 Practical Applications	85
3.6 Summary	86
Chapter 4.....	88
4 In-situ Assessment of Cross-tie Vibrations Induced by Freight Trains.....	88
4.1 General	88
4.2 Measurement Site, Accelerometer Array, and Test Trains.....	91
4.3 Acceleration Signal Analysis.....	96
4.3.1 Time Domain Analysis	97
4.3.2 Frequency Domain.....	107
4.4 Factors Affecting Vertical Acceleration Response of Supported and Voided Cross-ties	123
4.4.1 Static Track Stiffness	124
4.4.2 Train Velocity	126
4.5 Summary	131
Chapter 5.....	133
5 Numerical Modelling of cyclically-induced track suction and excess pore water pressure in ballasted tracks.....	133

5.1	General	133
5.2	Finite Element Model	136
5.2.1	Geometry and Meshing.....	136
5.2.2	Defining elements and materials.....	138
5.2.3	Model Calibration	141
5.2.4	Input cyclic train passby loading	142
5.2.5	Analysis Stages	144
5.2.6	Model limitations.....	145
5.3	Typical FEM Dynamic Simulation Results	145
5.4	Discussion and Analysis	148
5.5	Summary.....	153
Chapter 6	155
6	Conclusions, Major Findings and Recommendations for Future work.....	155
6.1	Conclusions.....	155
6.2	Major Findings and Observations.....	157
6.2	Recommendations for Future Work.....	160
References	161
Curriculum Vitae	175

List of Tables

Table 2.1 Properties of fouled sub-ballast sample	18
Table 3.1 Characteristics of the fouled sub-ballast.....	55
Table 3.2 Railroad fouling parameters.....	56
Table 3.3 Railroad condition for selected trains crossing fouled railroad segment.....	65
Table 4.1 Characteristics of the fouled sub-ballast.....	93
Table 4.2 Railroad fouling parameters.....	93
Table 4.3 Test trains operation conditions and rail-crib stiffness data	96
Table 5.1 Sub-structure input parameters	140
Table 5.2 Super-structure input parameters	140
Table 5.3 Selected trains operational velocity at the time of crossing.....	143

List of Figures

Fig. 1.1 Illustration of Track Cross-section and Subgrade Siphoning/Mud Pumping.....	2
Fig. 1.2 Photograph of locomotive and rolling stock traversing track.....	5
Fig. 2.1 Schematic diagram of different components of fouled railroad substructure	14
Fig. 2.2 Cross-section of fouled railroad failure mechanism.....	18
Fig. 2.3 Ballast, sub-ballast, and subgrade particle size distributions	19
Fig. 2.4 GDS enterprise level dynamic triaxial testing system & sample setup.....	22
Fig. 2.5 Sample cyclic loading: (a) symmetric cyclic one-way loading, (b) typical hysteresis response.....	25
Fig. 2.6 Fouled sub-ballast loaded at a frequency of 2.5 Hz	26
Fig. 2.7 Static response of fouled sub-ballast material for $\sigma_c=45$ kPa and $\sigma_c=90$ kPa.....	27
Fig. 2.8 Stress path followed by the fouled sub-ballast specimen	28
Fig. 2.9 Effect of loading rate on axial strains	30
Fig. 2.10 Effect of loading rate on volumetric strains	32
Fig. 2.11 Void ratio variation of fouled sub-ballast with consolidation stress	33
Fig. 2.12 C_v and m_v variation of fouled sub-ballast with consolidation stress: (a) coefficient of consolidation C_v , (b) coefficient of volume compressibility m_v	35
Fig. 2.13 Shear wave velocity variation of fouled sub-ballast with consolidation stress	36
Fig. 2.14 G_0 variation of fouled sub-ballast with consolidation stress	37

Fig. 2.15 Effect of loading rate on the shear modulus degradation curves.....	39
Fig. 2.16 Effect of loading rate on the damping ratio.....	42
Fig. 2.17 Effect of Plasticity on the Damping Ratio of Soils (Vucetic and Dobry, 1991)	43
Fig. 3.1 Fines surfaced at Parkville, MO, fouled site: (a) Fines surfaced between cross-ties, (b) Close-up on fines	48
Fig. 3.2 Sioux City BNSF railway network instrumented site at Parkville, MO.....	54
Fig. 3.3 Particle size distributions of fouled ballast, fouled sub-ballast, and subgrade	55
Fig. 3.4 Instrumented railroad: (a) layout plan, (b) cross-section.....	57
Fig. 3.5 Field monitoring sensors: (a) rail strain gauges and camera target, (b) Crib circuit, (c) cross-tie circuit (d) strain gauge calibration setup, (e) longitudinal rail bending-strain due to wheel loads.....	59
Fig. 3.6 Basler high-speed camera.....	60
Fig. 3.7 Data acquisition box	61
Fig. 3.8 Site weather station.....	61
Fig. 3.9 Moisture probe installation.....	62
Fig. 3.10 Local temperature profile during study period.....	63
Fig. 3.11 Effect of precipitation on soil moisture content	64
Fig. 3.12 Variation of ground moisture with static track stiffness.....	66
Fig. 3.13 Illustration of crib-rail and rail-tie loads.....	68

Fig. 3.14 Time history of the measured wheel-rail force for Train 1 obtained from rail-crib sensor B and rail-tie sensor C located in the fouled segment	72
Fig. 3.15 Time history of measured wheel-rail force for Train 2 obtained from rail-crib sensor B and rail-tie sensor C located in the fouled segment	75
Fig. 3.16 Time history of measured wheel-rail force for Train 3 obtained from rail-crib sensor B and rail-tie sensor C located in the fouled segment	77
Fig. 3.17 Time history of measured wheel-rail Force for Train 4 obtained from rail-crib sensor B and rail-tie sensor C located in the fouled segment	77
Fig. 3.18 Rail deflection in fouled segment due to cyclic loading of locomotive front bogie	79
Fig. 3.19 Variation in fouled static track stiffness (k) for the monitored trains passing over rail-crib sensor B and rail-tie sensor C located in the fouled segment for: (a) longitudinal range of influence of distant wheels, (b) rail-tie uplift ratio	81
Fig. 3.20 Fouled ballast bed empirical model for: (a) longitudinal range of influence, (b) uplift ratio	85
Fig. 4.1 Vibrations transmittal to substructure via superstructure	89
Fig. 4.2 Cross-tie mounted accelerometer	94
Fig. 4.3 Accelerometer measurement array layout plan	94
Fig. 4.4 Response of cross-ties due to Train A crossing: (a) fouled segment, (b) clean segment	99
Fig. 4.5 Response of cross-ties due to Train D crossing.....	100
Fig. 4.6 Acceleration of cross-ties due to Train B crossing.....	101
Fig. 4.7 Acceleration of cross-ties due to Train C crossing.....	102

Fig. 4.8 Acceleration of cross-ties due to Train E crossing	103
Fig. 4.9 Acceleration of cross-ties due to Train F crossing	104
Fig. 4.10 Variation of vibration amplification factor with train velocities for: (a) $k \leq 25$ MN/m, (b) $25 \text{ MN/m} \leq k \leq 51 \text{ MN/m}$, (c) $k \geq 51 \text{ MN/m}$	107
Fig. 4.11 FFT signal analysis of cross-tie acceleration for Train A crossing: (a) fouled segment, (b) clean segment	111
Fig. 4.12 FFT signal analysis of cross-tie acceleration for Train D crossing: (a) fouled segment, (b) clean segment	113
Fig. 4.13 FFT signal analysis of cross-tie acceleration for Train B crossing: (a) voided cross-tie (b), supported cross-tie.....	117
Fig. 4.14 FFT signal analysis of cross-tie acceleration for Train C crossing: (a) voided cross-tie, (b) supported cross-tie.....	119
Fig. 4.15 FFT signal analysis of cross-tie acceleration for Train E cross: (a) voided cross-tie, (b) supported cross-tie.....	121
Fig. 4.16 FFT signal analysis of cross-tie acceleration for Train E cross: (a) voided cross-tie, (b) supported cross-tie.....	123
Fig. 4.17 Effect of static track stiffness on acceleration response of supported and voided cross-ties	125
Fig. 4.18 Acceleration response of supported and voided cross-ties at different train velocities for: (a) $k \leq 25$ MN/m, (b) $25 \text{ MN/m} \leq k \leq 51 \text{ MN/m}$, (c) $k \geq 51 \text{ MN/m}$	128
Fig. 4.19 Amplitude and frequency of peak dominant acceleration response of supported and voided cross-ties at different train velocities for: (a-b) $k \leq 25$ MN/m, (c-d) $25 \leq k \leq 51$ MN/m, (e-f) $k \geq 51$ MN/m.....	130

Fig. 5.1 Cyclic-induced suction-based mud pumping mechanism (Takatoshi, 1997).....	134
Fig. 5.2 Cross-section of constructed plane-strain model.....	138
Fig. 5.3 Typical medium element distribution mesh	138
Fig. 5.4 Typical deflection output compared with measured track deflection.....	142
Fig. 5.5 Typical train loading time history used as applied point load.....	143
Fig. 5.6 Typical total vertical displacements U_y contour diagram.....	146
Fig. 5.7 Typical total horizontal displacements U_x contour diagram.....	147
Fig. 5.8 Typical excess pore water pressure PWP_{Excess} contour diagram.....	148
Fig. 5.9 Typical effective saturation contour diagram $GWL = 0B$	148
Fig. 5.10 Profile of excess pore water pressure under cross-tie centre.....	150
Fig. 5.11 Profile of excess pore water pressure under rail seat.....	150
Fig. 5.12 Profile of excess pore water pressure under cross-tie toe.....	151
Fig. 5.13 Profile of excess pore water pressure under crest.....	152
Fig. 5.14 Profile of excess pore water pressure slope edge	152

Glossary

Term	Definition
Static loads	are monotonic forces that are characterized by continuous application on the loading point.
Dynamic loads	are forces applied in a short time interval to the structure and/or substructure where the response of the structure and/or substructure is governed by stiffness and damping properties.
Cyclic loads	are a type of dynamic loads that are specific to repetitive loads due to train wheel loads (i.e. loads with approximately equal magnitudes), such loads are sinusoidal by nature with a maximum and minimum amplitudes.
Soil static properties	are the mechanical attributes that characterise the response of soil subjected to static loads, including but not limited to the static elastic modulus (E_s), unconfined compressive strength (UCS), friction angle (ϕ), and cohesion (c).
Soil dynamic properties	are the mechanical attributes that characterise the response of soil subjected to time dependent (dynamic) loads, including but not limited to the dynamic Young's modulus (E) and dynamic shear modulus (G), damping ratio (ζ), Poisson's ratio (ν), and cyclic shearing stress ratio (CSR) and cyclic deformation (γ_{cyclic}), compression wave velocity (V_p), shear wave velocity (V_s)...etc.
Surface waves	are train-induced Rayleigh waves generated by the interaction between "P" (longitudinal waves) and "S" (shear waves) at the surface of the railroad.
Compression waves	are train-induced elastic primary body waves that distort the volume of the substructure medium where the motion of the medium particles is longitudinal to the direction of propagation.
Shear waves	are train-induced elastic secondary body waves that shear through the substructure medium where the motion of the medium particles is perpendicular to the direction of propagation.
Surface deviations	are track defects in the track geometry exhibited in terms of variations in rail: gauge, horizontal plane level, alignment (vertical plane level), cant (cross-level), and twist.
Percent fouling	is material passing sieve size No. 200 (0.075 mm) by weight.
Fouling index	is the summation of percent passing sieve No. 200 (0.075 mm) and sieve No. 4 (4.75) by weight.

Chapter 1

1 Introduction

Railway transportation systems, including heavy haul railways, are developing rapidly to meet the growing needs of modern societies to move goods over long distances. Railway systems offer several advantages in terms of efficiency, sustainability, reliability, and safety compared to other transportation systems. Correspondingly, the sustainability and safety of railroad infrastructure through maintenance and implementation of new technologies have been the focus of numerous studies. Regular maintenance of railroads is necessary in order to sustain track geometry alignment, and to prevent deterioration of the ballast and sub-ballast over time, which represents a significant portion of operating costs to the freight railway companies.

The growth in freight traversing loads and trains speed results in increased surface deformation of railroad substructure, which leads to cumulative plastic strains and surface deviation of the railroad tracks. The surface deviation (cross-level and profile) of ballasted railroad tracks is influenced primarily by the geo-mechanical characteristics of the granular substructure due to the accumulation of permanent strains in the ballast and the sub-ballast. Therefore, excessive permanent strains beyond acceptable thresholds in the granular substructure of the railroad necessitate immediate remedial action in terms of track maintenance that involves restoring both longitudinal and horizontal plane level and alignment. Alternatively, restraint in terms of train speeds and/or loads should be implemented. Therefore, this thesis is dedicated to investigating the performance of fouled railroad superstructure when subjected to train passby loading by heavy haul trains.

1.1 Preamble

In the race towards sustainable, green, and cost-effective transportation, rail wins by far because locomotives emit far fewer greenhouse gases than other modes of transportation (GlobalRailwayReview, 2021). Rail networks play major role in world economy by enabling

heavy hauling cargo and supplies between cities, states, provinces, and countries. To remain competitive and to increase its market share, the railway industry is required to improve operating efficiency, decrease maintenance costs and invest in infrastructure expansion to reach more customers (Indraratna et al., 2011).

A typical railroad is comprised of two main components: the track and foundation. A typical modern railway track consists of the rail, fasteners, and cross-ties (see Fig. 1.1). The foundation bed consists of ballast, sub-ballast, and native soil. The rail made from steel carries train wheels and transmits train loads to the cross-ties. Fasteners are made from steel and hold the rail together with the cross-ties. The cross-ties (made from concrete or timber) provide support and transmit the applied train loads to the track foundation. The ballast is comprised of crushed stone and its main functions is to support train loads and drain water from the track. The sub-ballast (smaller diameter particles) acts as a diaphragm between the ballast and the native soil. The native soil is the local soil type present on the ground surface on top of which the railroad is constructed. Track fouling is a railroad condition where the ballast gets contaminated with fines (sands, silts, and clays). Progressive use of fouled track by traversing trains causes mud (fines) to be pumped and a gap to exist beneath the cross-ties a phenomenon called the voided cross-tie.

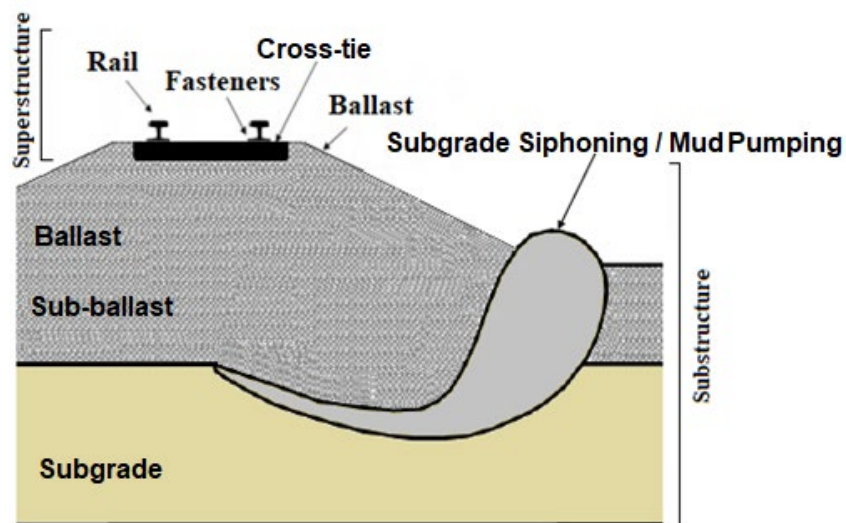


Fig. 1.1 Illustration of Track Cross-section and Subgrade Siphoning/Mud Pumping

A large percentage of ballasted track maintenance budget is spent on substructure associated problems (Indraratna et al., 2011), including ballast fouling/contamination (i.e. the presence of fine material passing sieve size No. 200 (0.075 mm) by weight in the ballast. The substructure maintenance cost can be considerably reduced, provided that a better insight of the physical properties and understanding the cyclic behaviour of fouled railroad (Indraratna and Ngo, 2018). In low relief areas where the predominant subgrade soil types are saturated clays and silts, may be pumped upwards into the ballast in the form of slurry, under cyclic wheel loading action (Selig and Waters, 1994; Raut, 2006). Subgrade siphoning is exacerbated when the sub-ballast layer fails to act as a diaphragm layer (filter and drain the saturated fine particles) due to excessive interlayering with the sub-grade.

Mechanical problems associated with subgrade pumping include increased compressibility, reduced void ratio, diminished permeability, and decreased internal friction angle (Indraratna et al., 2014). The decrease in the friction angle of fine contaminated ballast particles is attributed to the presence of fine material coating the ballast particles (i.e., decreasing the apparent angularity). In situ conditions such as the phreatic regime and surrounding environmental conditions have significant influence on the behaviour of fouled railroads (superstructure and substructure). However, there is limited long-term monitoring data available to characterize the deformational behavior of ballast in various states of static track stiffness.

1.2 Motivation and Problem Statement

The current study is part of a large research program administered by the Federal Railroad Administration (FRA) office of research, development, and technology at the U.S. Department of Transportation (USDOT) to monitor railway track, rolling stock, train control and communications, and human factors (FRA, 2021). The present research is part of the Ballast Waiver Project, in cooperation with the Association of American Railroads (AAR), which was initiated by an issued waiver from ballast requirements, regulation §213.103 of the Federal Track Safety Standards (FTSS), for designated Burlington Northern Santa Fe (BNSF) railway network subdivisions. The issued waiver meant that the designated tracks are allowed to foul

and deviate from specification. The waiver provided an opportunity to improve the understanding of the performance of the superstructure of fouled ballasted railroads. To achieve this objective, the AAR-FRA joint venture research project was initiated in November 2017 and continued to December 2019. The ultimate goal of the current study is to create baseline data for a system similar to the Positive Train Control (PTC) system. Onboard PTC is an advanced technological solution designed to stop a train before accidents happen due to track obstruction, signals/switch failure, train collisions, excessive speed, and unauthorized train movements on tracks due to human error (AAR, 2020). The proposed track control system will detect unusual behavior of the superstructure (rail and cross-ties) and substructure (sub-ballast) in response to cyclic loading and compare the response of the track against established superstructure threshold limits.

Percent fouling (material passing sieve No. 200 or 0.075 mm) of 35% is considered the highest threshold permitted and implies that immediate maintenance should take place given that track geometry issue arises (Bruzek et al., 2016). However, occurrence of track geometry issues is an unsafe operating condition and may result in train derailment. Thus, superstructure instrumentation is necessary to establish track response thresholds for track infrastructure to mitigate disasters, in a manner similar to Positive Train Control (PTC) systems onboard. The scarcity of pertinent data with regards to the performance of the superstructure components of fouled railroads, and the imprecision of performance indicators are the main drivers of the current research effort. The high variability in the response of the superstructure and the deficiency of long-term track/field measurements provided the impetus for this research endeavor. Therefore, this study is designed to develop a better understanding of the reduced performance of fouled railroad by quantifying the response of the superstructure under a range of changing weather conditions, and thus support conditions.

1.3 Objectives and Scope

The main objective of the current study is to produce relevant information about the behavior of the superstructure (rail and cross-ties) and substructure (sub-ballast) in response to cyclic loading due to traversing trains (see Fig. 1.2) . This is achieved by collecting and analyzing

long-term track performance data using in-situ instrumentation. The data were collected under a range of weather conditions to evaluate the variation of the superstructure response and its effect on the performance (rail deflection and cross-tie vibration) of fouled tracks due to subgrade intrusion.



Fig. 1.2 Photograph of locomotive and rolling stock traversing track

The following research objectives were developed within the scope of this study:

- Quantify the long-term deformational behavior (plastic axial and volumetric strains) of fouled sub-ballast material with 5 % fine contamination and its residual stress–strain behaviour.
- Evaluate the extent of deterioration and post-failure behaviour by assessing shear modulus degradation curves of railroad fouled sub-ballast due to a variety of cyclic loading frequencies as proxy of train speed.
- Propose guidelines to operators for the train speed limits in fouled railroad segments to prevent degradation of sub-ballast shear modulus.
- Quantify rail deflection and interpret static track stiffness due to heavy haul trains travelling fouled track in adverse environmental conditions by gathering long-term monitoring data throughout the four seasons to ascertain repeatability and accuracy of inferred results..
- Provide qualitative and quantitative insights with regards to the cross-tie support efficiency as a mean to assess static track stiffness and provide alternative methods to assess static track stiffness based on empirical data.

- Interpret track response of fouled railroad using analytical solutions and establish static track stiffness estimated from continuous measurement of stiffness under cyclic load inferred from high-speed deflectograph.
- Produce vertical cross-tie acceleration response charts to examine the effect of train velocity and static track stiffness on the behaviour of both voided and supported cross-ties.
- Quantify excess pore water stresses induced due to actual measured cyclic loads of trains with different loading-time histories to assess the variance in the generated positive and negative excess pore water pressures.

1.4 Highlights of Research Contributions

1.4.1 Static and Cyclic Characterization of Fouled Railroad Sub-Ballast Layer Behaviour

- The results indicate that soil plasticity, effective confining pressure, and relative density are not the only important factors in shaping the damping curves but also the loading rate, and particle size.
- It is recommended that, at fouled railroad segments, railway operators should restrict train speed exerting average wheel stress in the range of 300 kPa, to a maximum of 32 km/h unless in-situ dynamic characterization proved otherwise. The speed limit is set to preserve 80% of the shear modulus of the sub-ballast and prevent further damage to railroad substructure and to maintain railroad integrity.
- In response to the change of the loading rate, the sizes of the hysteresis loops were found to be varied, along with the shear strain amplitudes of the cyclic loading.
- Sub-ballast specimen loaded at a frequency of 2.5 Hz, simulating a train passing by over the fouled railroad segment with a speed of 32 km/h, exhibited 3 distinct shear modulus

degradation stages, due to its prolonged failure behaviour, unlike the samples loaded at 5Hz and 10Hz, which were characterized by faster failure response.

1.4.2 In-situ Performance Assessment of Track Superstructure on Fouled Railroad

- Results indicate that as the fouled track stiffness increased the influence range of wheels on superstructure increased, for concrete cross-tie supported railroad.
- The tie-load ratio may misrepresent the superstructure efficiency in fouled ballast beds. Alternatively, the range of influence of distant wheels along with the uplift ratio may be used to assess fouled railroad performance.
- Novel empirical models were proposed to evaluate the longitudinal range of influence of wheels on the superstructure and uplift ratio.

1.4.3 Quantification of Cross-tie Vibrations and the Effect of Static track stiffness

- Results showed that when crossing through soft to typical static track stiffness i.e. $k \leq 51$ MN/m, or during summer/spring seasons, the train velocity should be less than 70 km/h, so that the vertical acceleration of voided cross-ties remains below $\pm 3.0g$ (i.e. acceleration level of supported cross-ties for typical track stiffness range).
- When traversing stiff track, i.e. $k \geq 51$ MN/m, or during fall/winter seasons, the train velocity should be less than 20 km/h so that the vertical acceleration of voided cross-ties remains below $\pm 3.0g$ (i.e. acceleration level of supported cross-ties for typical track stiffness range).

1.4.4 Finite Element Modelling of Fouled Track Using Actual Loading Simulations

- Results showed that maximum negative PWP of -5 kPa developed in the vicinity of the loading zone (near the cross-tie) and the maximum positive excess PWP of 140 kPa developed at a depth of 0.5B.
- In the vicinity of the cross-tie, the excess PWP increased by 1.2 times as the train velocity increased from 67 km/h to 102 km/h.
- Maximum positive excess PWP of 95 kPa developed away from the loading zone (far from the cross-tie) at a depth of 0.5B.
- Away from the cross-tie, the excess PWP increased by 1.3 times as the train velocity increased from 67 km/h to 102 km/h.

1.5 Research Methods and Thesis Organization

This thesis comprises of three main parts to evaluate the dynamic behavior of the tested fouled railroad. The first part consists of laboratory testing to evaluate the dynamic behaviour of fouled sub-structure material retrieved for the test site. The second part involves railway monitoring, using wayside track instrumentation on the superstructure components (rail and cross-ties). In addition, the phreatic regime of the railroad substructure was monitored using ballast embedded moisture content probes. Moreover, a state-of-the-art sustainable weather station, powered by a wind turbine and solar panel, located in the vicinity of the track was employed to observe the surrounding environmental conditions. The third part utilizes finite element modeling to simulate the performance of fouled railroad under cyclic train passby loading to obtain deeper insights on the behaviour of failure of the track substructure. This thesis is authored as a compendium of four technical papers and structured as follows:

Chapter 1 presents an overview of the study and rationale behind the research efforts endeavored. It identifies the objectives and scope of the thesis and summarizes the contribution of the study to the current state of knowledge.

Chapter 2 investigates the static and cyclic characteristics of a fouled sub-ballast material using static and cyclic triaxial tests. In addition, one-dimensional oedometer tests were performed to provide quantitative results regarding the axial deformation behaviour of the fouled sub-ballast specimens. Utilizing the oedometer consolidation cell coupled with piezo-electric ring actuator system, shear wave velocity of the fouled sub-ballast material was measured in dry conditions and at a moisture content of 5 %, which is typical for wet railroad condition.

Chapter 3 assesses the dynamic behavior of the super-structure component of a freight line railway system in a fouled ballasted railroad zone using way side instruments and data collected from track measurements. Industry standard circuits sensors were positioned on rails and sleepers, respectively. Railroad super-structure response due to track fouling was analyzed for four selected trains, travelled through the fouled section. The longitudinal range of influence of distant wheel loads was analyzed by correlating the range of influence with the distance of the wheel load peaks (wavelength, “S”) on the rail-tie force induced and cross-tie bending moment generated.

Chapter 4 quantifies train induced free vibrations due surface waves traveling on fouled track surface. The concrete cross-ties acceleration response collected from track measurements was quantified and used to back-calculate the transient displacement of the superstructure to estimate the static track stiffness. The cross-tie free vibrations in the fouled segment of the track were quantified and compared with the sleeper vibration at the clean section of the railroad. Moreover, the static track stiffness obtained using the cross-tie spectral displacement at the fouled segment was compared with the static track stiffness obtained using deflection readings using the high-speed cameras mounted in the enclosure. Propagation of the in-track free vibration was discussed in the distance domain.

Chapter 5 describes the numerical study conducted using the dynamic 2D FEM software PLAXIS to study the effect of train velocity on generated positive and negative excess pore water pressures using a variety of loading time histories for different train velocities. Results presented in the form of pore water pressure charts vs depth.

Chapter 6 presents the summary of the research and conclusions of pertinent information and data backed recommendations for railway operators in addition to suggestions for future work.

Chapter 2

2 Static and Cyclic Characterization of Fouled Railroad Sub-Ballast Layer Behaviour ¹

2.1 General

Railway is an important freight transportation system, which enjoys rapid development of heavy haul railway and offers efficiency and safety compared to other transport systems. Correspondingly, the sustainability and safety of railroad infrastructure through maintenance and implementation of new technology have been the focus of numerous studies. The stability of railroads is important for ensuring safe and efficient operation of railway systems. Therefore, regular maintenance of railroads is necessary to sustain track geometry alignment, and to prevent deterioration of the ballast and the sub-ballast over time. The increase in maintenance costs is directly associated with the increase in cargo loads (Chrismer and Davis, 2000; Lee, 2009). The estimated annual cost of maintenance operations for railroad substructure amounts to \$500M for every 150,000 km of class I tracks (Chrismer and Davis, 2000).

2.2 Literature Review

Growth in freight train passby loads increases the surface deformation of railroad substructure resulting from cumulative plastic strains, which causes surface deviation in the railroad tracks (Ebrahimi et al., 2014; Bian et al., 2016). The surface deviation (horizontal plane level and alignment) of ballasted railroad tracks is influenced primarily by the geo-mechanical characteristics of the granular substructure. Esveld (1989) attributed the track longitudinal

¹ A version of this chapter has been published in the Journal of Soil Dynamics and Earthquake Engineering: Touqan, M., Ahmed, A., El Naggar, M.H., & Stark, T.D. (2020). Static and cyclic characterization of fouled railroad sub-ballast layer behaviour. Journal of Soil Dynamics and Earthquake Engineering, 137, 106293

deformation to the accumulation of permanent strains in the ballast and the sub-ballast. Therefore, excessive permanent strains beyond acceptable thresholds in the granular substructure of the railroad necessitate immediate remedial action in terms of track maintenance that involves restoring both longitudinal and horizontal plane level and alignment. Alternatively, restraint in terms of train speeds and/or loads should be implemented (Esveld, 1989; Selig and Waters, 1994; Suiker et al., 2005).

Tamping and stone blowing are maintenance procedures that are carried out mechanically to restore track longitudinal profile (Suiker et al., 2005). However, in extreme cases of recurring track fouling (i.e. excessive track deflection, multiple voided cross-ties were noticed during visual inspection), track undercutting is performed to completely replace fouled ballast with fresh one. Tamping is repeatedly carried out on irregular track segments that are in need of smoothing. Ballast tamping is performed by lifting each of the cross-ties to a prescribed height, then a tamping unit with a vibrating steel fork shakes the granular ballast material in an effort to restore the prescribed height of the cross-ties. Although the tamping process may successfully restore the cross-ties to the prescribed height, it may result in unfavorable results such as ballast attrition (Esveld, 1989; Selig and Waters, 1994; Suiker et al., 2005).

Stone blowing is a viable alternative to tamping. It involves pneumatically injecting quantities of small stones beneath the raised cross-tie, which minimizes ballast disturbance and particle attrition, hence creates an interlayered layer directly beneath the ballast (i.e. the sub-ballast). Esveld (1989) and Anderson and Key (2000) suggested that stone blowing provide a better post maintenance performance than tamping when utilizing proper size, type and quantity of injected particles to effectively fill the voids in the ballast. In extreme cases, undercutting is performed when the substructure beneath the cross-ties is fouled. It is performed by an excavator that moves fouled ballast surrounding the cross-ties and replaces the fouled ballast with a fresh ballast. However, undercutting is only performed when both tamping and stone blowing fail to restore track longitudinal profile and the failure of the sub-structure is persistent.

The deterioration of the mechanical characteristics of the granular substructure material from the original standard specification gives rise to fouling materials (0.0016mm - 12mm) within the railroad substructure as shown in Fig. 2.1 (Bailey et al., 2011). The fine material fouling has an adverse effect on the load distribution mechanism of the substructure to the underlying subgrade (Bruzek et al., 2016). The impact extends to the behavior of the railroad superstructure in terms of more excessive transient displacements and the accumulation of permanent deformations. Furthermore, the variability in the longitudinal profile of the tracks leads to variation in track substructure stiffness, which would eventually lead to excessive vibration of trains that can have a detrimental effect on track integrity and safety of train operation.

The sub-ballast is a vital, load bearing, integrity maintaining, component of the ballasted railroad substructure system. It underlies the ballast and is composed of particles finer than the ballast. The sub-ballast comprises granular material (gravel and/or sand) and should not contain cohesive material. It has three main functions: providing firm support for the ballast to transfer and diffuse cyclic loads applied from passing trains safely to the soft subgrade; preventing the mutual infiltration (slurry pumping due to rise of phreatic level) amongst the ballast and subgrade; and preventing the generation of excess pore water pressure by allowing precipitation water to drain from the ballast (Parsons et al., 2014; Su et al., 2015). Therefore, the stability of the ballast is directly related to the sub-ballast performing its three main functions. One of the main reasons for excessive deformation and eventual failure of ballasted railroads, is the weakening of the sub-ballast layer due to fines contaminating (fouling) the sub-ballast zone. Consequently, the drainage of the excess pore water pressure is slowed down (hindered). The fouling phenomenon of ballasted railroads (See Fig. 2.1) is a major cause for railway track degradation and is observed all over the world (Lazorenko et al., 2019). The hindered drainage in the ballast due to the decrease in porosity gives rise to excess pore water pressure that deters the functions and degrades the strength of the sub-ballast layer. Eventually, it causes mud pumping from the subgrade to the ballast. Consequently, water and fines accumulate in the intergranular space of all the layers forming the ballasted railroad, the track

saturates and its stability degrades leading to reduced load bearing capacity (Selig and Waters, 1994; Indraratna et al., 2010; Li et al., 2016).

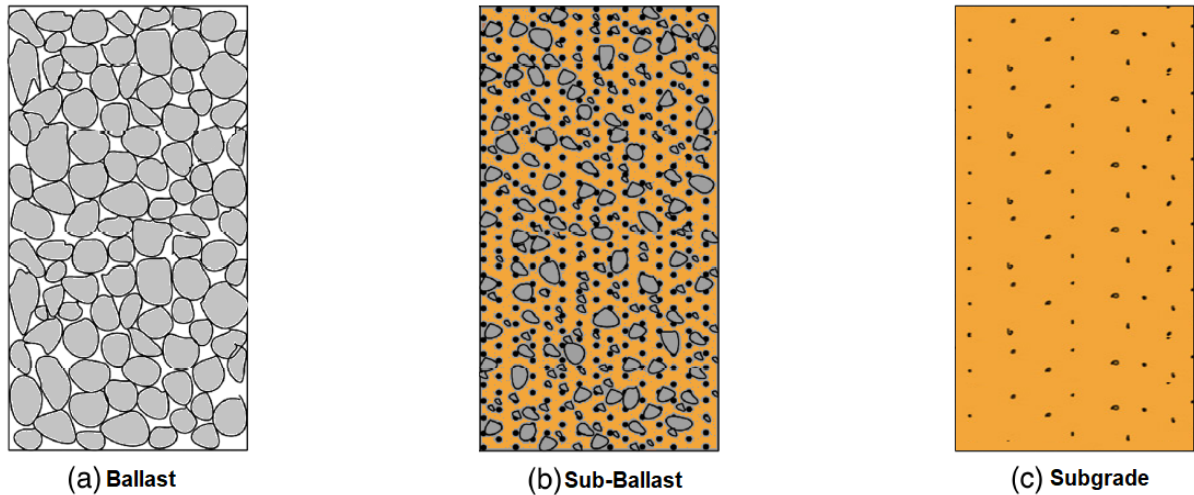


Fig. 2.1 Schematic diagram of different components of fouled railroad substructure

The degree of particle attrition and the mechanical behavior of the railroad substructure were investigated considering only the effect of in-situ confining pressure (Indraratna et al., 2005; Lackenby et al., 2007). Although, these investigations provided valuable insights on the breakage behavior and overall mechanical response of the railroad substructure, there were some important parameters in which these studies either did not investigate or did not study in depth. The effect of track fouling on the overall mechanical and dynamic behavior and particle attrition of the sub-ballast were not considered in these investigations. Also, the effect of in-situ confining pressure, rate of loading (train speed) and wheel-load induced stresses (applied cyclic load) on the performance of fouled substructure under cyclic loading were not examined in depth.

A review of the current state of knowledge revealed that most of the studies focused on examining soil material from the subgrade, sub-ballast, and ballast in order to investigate the mechanical-dynamic behaviour due to train loading. For instance, Haque et al. (2007) focused on the intrusion of fines from the sub-grade by evaluating the effect of loading frequency on the filtration performance of the sub-ballast behavior under cyclic loading. The study found

that increasing the cyclic loading caused an increase in turbidity which in turn indicated the migration of soil particles from the subgrade to the sub-ballast. However, the study only focused on the migration process of fines from the subgrade and not the dynamic behaviour of the sub-ballast. Ling et al. (2017) performed laboratory tests to characterize the permanent strain behavior of coarse-grained subgrade soils. Similarly, Liu and Xiao (2009) study investigated the stability of a silty subgrade under railroad traffic loading with increasing speed, simulated in a cyclic triaxial test. The study recommended constraints in train speeds without suggesting a maximum train speed.

Huang et al. (2009) examined fouled ballast using direct shear box tests and investigated the effect of fouling agents (clayey soil, coal dust) on the strength of railroad ballast. Bailey et al. (2011) and Ebrahimi (2011) presented results and analysis of laboratory tests related to fouled ballast from railway embankment in an effort to identify the source of fine material fouling in the studied railroad and to provide guidelines of fouled ballast laboratory testing. Indraratna et al. (2012) conducted consolidated drained cyclic triaxial tests of fouled ballast under different confining pressures and void contamination indices. In a similar context, Suiker et al. (2005) investigated the tendency of clean ballast and uncontaminated sub-ballast materials to compact under cyclic loading. The study provided valuable insight about the effect of the applied cyclic deviator stress on the behaviour of railway substructure. Nevertheless, it did not address the effect of the applied static and cyclic stresses on the behaviour of fouled (fine-contaminated) sub-ballast.

Trinh et al. (2012), Duong et al. (2014) and Bian et al. (2016) identified the track substructure interlayering (sub-ballast) zone between the ballast and the subgrade as a loading phenomenon through field monitoring. However, these studies did not examine the effect of the loading rate on the behaviour of the fouled sub-ballast. Meanwhile, Lamas-Lopez et al. (2016) found that the resilient modulus of the uncontaminated sub-ballast layer decreased by 25% as the train speed increased from 60 km/h to 200 km/h. In a similar study, Lamas-Lopez et al. (2017) reported that when the train speed was increased from 100 km/h to 200 km/h, the damping ratio (D_r) of the uncontaminated sub-ballast layer was stable at 5 %. Although both studies

gave valuable insight about the dynamic properties of the sub-ballast layer, the findings were applicable to clean uncontaminated sub-ballast in good condition. Tamrakar (2017) only focused on the impact of fines on the mechanical performance of flexible pavement base materials and railroad ballast.

Lazorenko et al. (2019) stated that the heterogeneous sub-ballast layer of the railroad substructure experiences the most deformation, where heavy haul trains travelling at high speeds often cause the degradation of railroad substructure and accelerates the deterioration of the railroad ballast. The study underscored the need to investigate the transfer of cyclic loads from heavy haul trains to fouled track substructure. In particular, they highlighted the gap in the current state of knowledge with regards to the effect of the loading frequency (train speed), magnitude of loading (applied train wheel loads), and degree of compaction, and moisture content on the mechanical-dynamic behaviour of fouled rail roads. This thesis aims to address the gap in the current state of knowledge with regards to the effect of the loading frequency (train speed) by providing insight about the mechanical-dynamic behaviour of fine-contaminated sub-ballast layer found in a typical wet fouled railroad.

2.3 Objective and Scope of Work

The previous studies highlighted the relationship between increased train speed and the rate of deterioration. However, these studies did not provide an insight on the extent of deterioration and post-failure behaviour of railroad substructure due to heavy haul trains travelling at high speeds. Therefore, the current study attempts to provide an understanding of the dynamic behaviour of fouled sub-ballast under cyclic loading and propose guidelines to operators about the train speed limits in fouled railroad segments. To achieve this objective and to cover the gap in the current state of knowledge, this study investigates the effect of train speed at fouled railroad segments to quantify the long-term deformational behavior of fouled sub-ballast material with 5 % fines contamination and its residual stress–strain behaviour. Fouled samples retrieved from a fouled track segment were subjected to cyclic isotropic loading conditions in a cyclic triaxial machine to simulate freight traffic loads. Furthermore, the plastic axial and

volumetric strains of fouled sub-ballast were quantified and the effect of loading on the propagation of shear waves was studied.

2.4 Materials and Methods

2.4.1 Parkville-Missouri Site Soil Profile

The fouled sub-ballast samples used in this study were retrieved from the Parkville-Missouri site located in the Northwestern part of the city of Parkville, Missouri, USA ($39^{\circ}11'22.6''N$ $94^{\circ}41'21.1''W$). The instrumented fouled site is a 281 m single track segment part of the 175 km -Sioux City BNSF (Burlington Northern Santa Fe) railway network. The cross-section and failure mechanism of fouled railroad are presented schematically in Fig. 2.2. The grain size distribution test for ballast and underlying sub-ballast was conducted based on the standards of ASTM D 6913 (ASTM, 2004). The railroad sub-structure samples were recovered after a thorough visual inspection of the track surface. The inspection was conducted to ensure that the samples collected are representative of the fouled segment.

Fig 2.3 shows the grain size distribution results for the tested soils and the mechanical properties of the tested soils are presented in Table 2.1. Based on the Unified soil Classification system, the fouled sub-ballast can be classified as Well Graded Gravel (GW) with sand. However, based on AASHTO M 145 system (AASHTO, 2008), the fouled sub-ballast can be classified as A-2-4(0). Whilst, the fouled Ballast can be classified as Poorly Graded Gravel (GP), and as A-1-a (stone fragments, gravel and sand) according to USCS and AASHTO, respectively. According to the USCS the sub-grade can be classified as Silty Sand (SM), and A-2-4(0) based on AASHTO.

Table 2.1 Properties of fouled sub-ballast sample

Sub-Ballast Property	Value
Maximum Dry Density, ρ_d	1.93 g/cm ³
Friction Angle, ϕ	40.00°
Plasticity Index, PI	10.00
Specific Gravity, G_s	2.65
Coefficient of Uniformity, C_u	25.10
Coefficient of Curvature, C_c	2.80
D ₁₀	0.30 mm
D ₃₀	3.10 mm
Mean Diameter, D ₅₀	7.40 mm
D ₆₀	9.50 mm

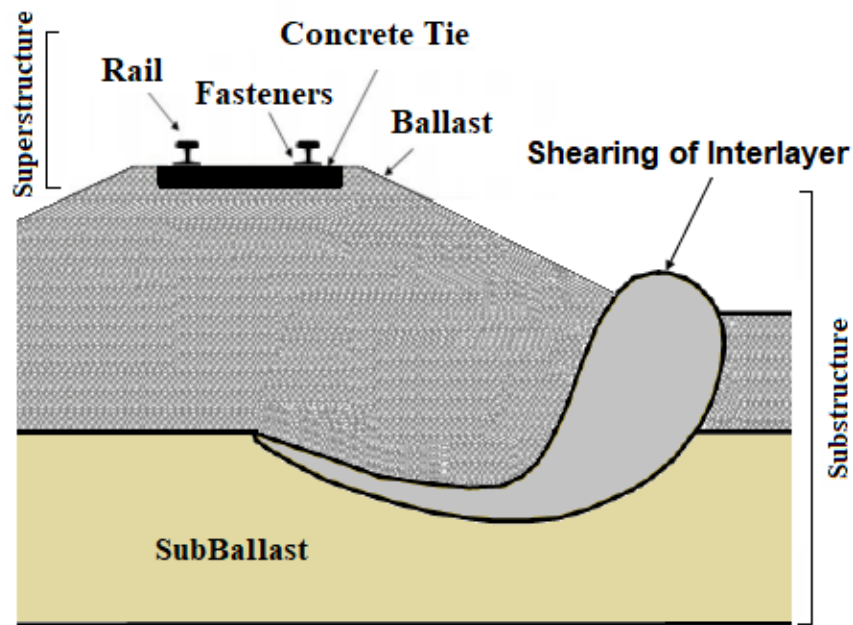


Fig. 2.2 Cross-section of fouled railroad failure mechanism

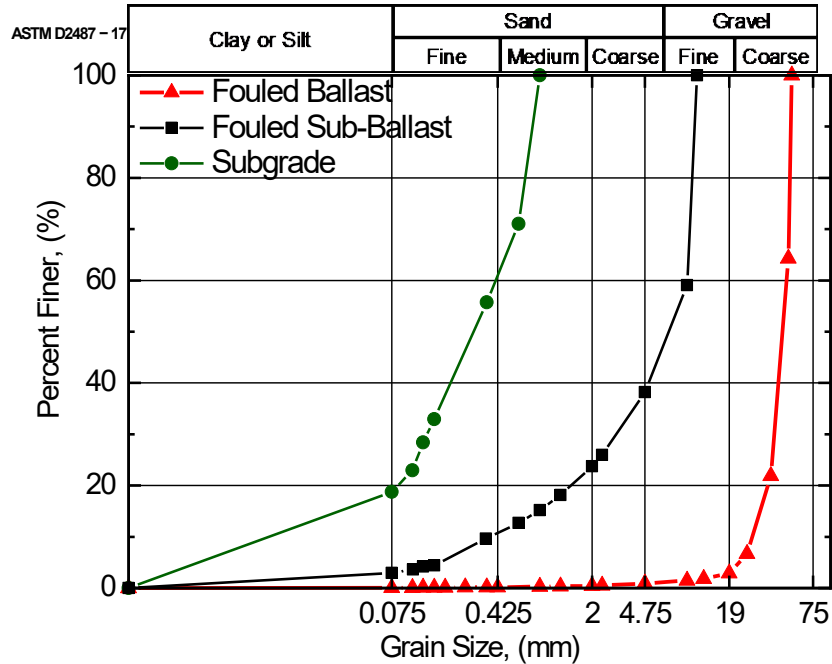


Fig. 2.3 Ballast, sub-ballast, and subgrade particle size distributions

2.4.2 Laboratory Testing Program

A laboratory testing program was conducted to evaluate the effect of loading frequency (as a proxy for train speed) on the behaviour of fouled track bed with the following two objectives. Firstly, advance the current state of knowledge on the dynamic stress-strain properties of fouled sub-ballast interlayer soil. Secondly, to provide relevant data to suggest guidelines for railway operators in terms of train speed in fouled segments of the railway network to prevent serious damage. The testing program involved strain controlled static isotropic consolidated drained (Lackenby et al.) triaxial test, and cyclic load controlled isotropically consolidated drained (Lackenby et al.) cyclic triaxial tests. The monotonic loading was used as a control in order to quantify the effect the loading rate on the behaviour of the sub-ballast.

The following parameters were controlled and maintained constant throughout the testing program: the degree of saturation (B-value), the applied axial stress (σ_a), and the confining pressure (σ_c). The degree of saturation was maintained close to unity (≈ 0.99) to ensure two-

phase soil specimen conditions, and to model the in-situ worst-case scenario, where the pumping of the subgrade and the sub-ballast would take place. The axial stress (σ_a) of 300 kPa was applied for the isotropically consolidated drained (Lackenby et al.) cyclic triaxial tests. Meanwhile, the confining pressure (σ_c) used was controlled at 90 kPa in both static and cyclic tests to mimic railroad in-situ confining pressure.

Ebrahimi et al. (2012) noted that the loading frequency is affected by both train speed and the shape of stress distribution at different depths beneath the sleepers. However, in this paper the loading frequency was varied in the cyclic triaxial tests to cover a practical range that corresponds to frequency associated with freight train speeds. The loading was applied at frequencies of 2.5 Hz, 5.0 Hz and 10 Hz to simulate trains travelling at 32 km/h, 64 km/h, and 128 km/h, respectively; which is similar to measurements reported by Indraratna et al. (2010). Ebrahimi et al. (2012) estimated the loading frequency based on the train speed and the stress distribution curve at different depths in the railroad sub-structure using finite element analysis. The loading frequency was calculated as $f = (L/V)^{-1}$, whereas L is the axel distance and V is the train speed. It is imperative to note that principal stress rotation of travelling load can hardly be simulated by conventional triaxial machine. To be able to simulate the rotation effect of the travelling load variable confining stress need to be used, which cannot be achievable using the triaxial machine used in this study.

2.4.3 Test Apparatus

Conventional triaxial machine can be problematic for testing coarse aggregate due to the relatively small size of the chamber and machine setup (Marschi et al., 1972). However, the disparity between sample and particle size can have an effect on the results if the ratio of specimen diameter to maximum particle size is less than 6 (Marschi et al., 1972; Lackenby et al., 2007). In the current experimental program, the height of the cylindrical sub-ballast specimen was equal to $H=115$ mm and the diameter was equal to $D=70$ mm, i.e. $H/D \approx 2$ according to ASTM (2011). The largest grain size in the well graded sub-ballast with sand

material was $d=11.2$ mm (see Fig. 2.3), thus the specimen diameter to maximum particle grain size ratio, $D/d = 6.3 > 6$.

The triaxial testing machine used for conducting the tests was GDS ELDYN (shown in Fig. 2.4), which is capable of applying cyclic loads at frequencies up to 10 Hz with a maximum axial load capability of ± 10 kN at cell pressure that ranges up to 2 MPa. The permanent vertical strain readings were acquired by logging the position of the piston at regular intervals. The resilient deformation was also measured for certain cycles. The triaxial pressure and volume controller measured volume change corresponding to the change in the internal piston position (due to water entering or leaving the specimen resulting in its dilation or contraction). The triaxial cell was equipped with transducers at the base of the specimen to measure the pore water pressure and back pressure, and pressure transducer at the base of the cell chamber to measure the confining pressure. These measurements were used to determine the effective stresses of the specimen during loading.

Oedometer cells utilized were 70 mm in diameter and 25.4 mm in height; the cells contained the fouled sub-ballast specimens during the test. Meanwhile, the specimens were sandwiched between two ring shaped piezoelectric elements (shear wave velocity transmitter and receiver), components of the novel Piezoelectric Ring Actuator system (Ahmad, 2016; Ethier et al., 2016). The Piezoelectric Ring Actuator system comprised of ring-shaped piezoelectric elements with inner and outer diameters $\varnothing_{\text{inner}} = 38$ mm, $\varnothing_{\text{outer}} = 44$ mm, respectively and height, $H = 3.5$ mm.

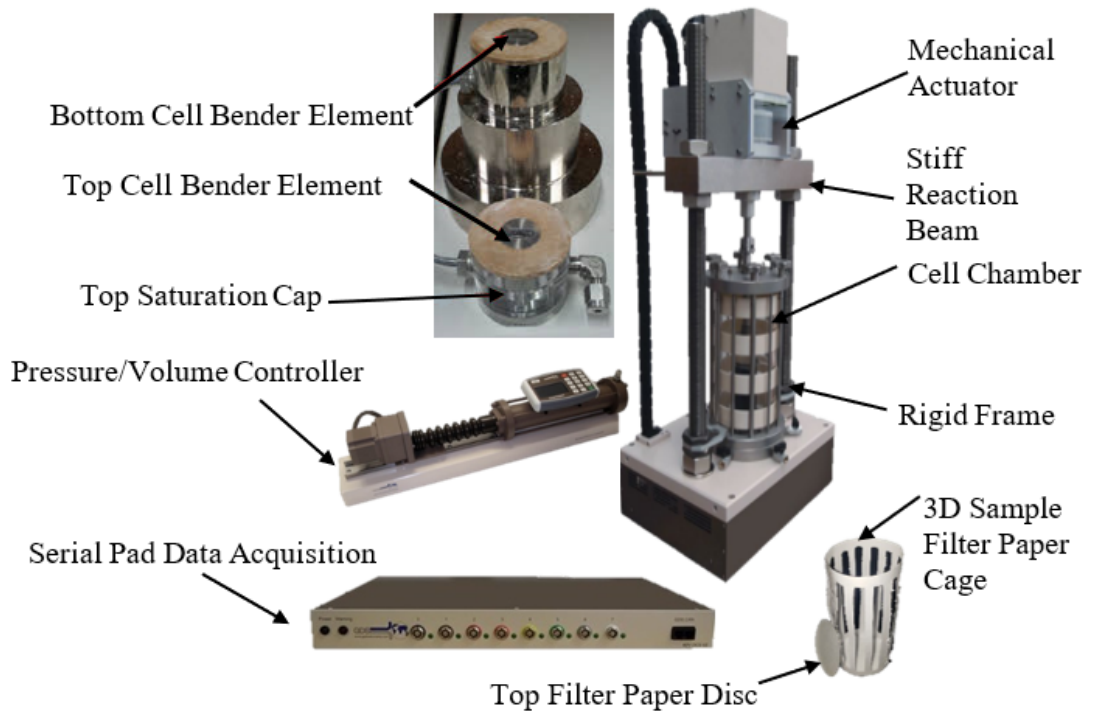


Fig. 2.4 GDS enterprise level dynamic triaxial testing system & sample setup

2.4.4 Sample Preparation

The 70 mm sub-ballast specimens were enclosed in two latex membranes, each was 0.3 mm thick. The double membrane setup provided added strength to avoid membrane puncture by the sharp edges of the sub-ballast particles. The effect of the two latex membrane layers was considered in interpreting the results by using 0.6 mm as the thickness of the membrane in the testing machine user interface. The latex membranes were held by neoprene O rings at the top cap and the base pedestal. The O rings prevented any air/and or water from entering to the sample from the triaxial chamber.

The compaction mold assembly was secured on top of the pedestal, which facilitated the compaction of the specimen into 6 lifts of equal height layers. Internal vacuum was applied during compaction to hold the latex membrane against the wall of the compaction mold. After compaction was completed, the density was calculated and to ensure uniformity of the final sample density, the top cap was placed, and the mold was removed. Meanwhile, temporary

internal vacuum was applied to prevent the specimen from collapsing. The top cap and the bottom pedestal were treated with vacuum grease to ensure a seamless connection with the latex membrane.

Specimens were prepared at the maximum dry density to simulate the in-site condition. Prior to placement, the sub-ballast specimens were thoroughly mixed to ensure consistency. The fouled sub-ballast specimen was divided into six layers with equal heights (ASTM, 2011). Each layer was placed inside the chamber and was compacted using a vibrating plate (Ebrahimi, 2011; Indraratna et al., 2012) All layers were lifted and compacted until the final height of 115 mm was reached. The specimen was then placed in the triaxial chamber and saturation commenced from the top downwards, and was completed after 48h, approximately. The tested soil samples exhibited high shear strain amplitudes in response to the applied cyclic loading, such high strain amplitudes usually accompanied with volume change propensities.

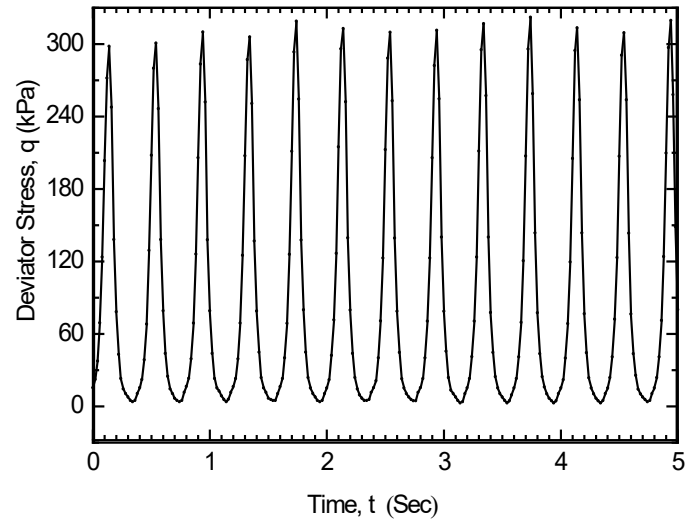
Cyclic triaxial tests were conducted under drained loading conditions to simulate long term effects. However, because of the high fouling, the tested samples had poor drainage. Therefore, 3-dimensional filter paper drainage cages bridging the top and bottom porous plates were used to facilitate sample drainage. Thus, volume change tendency was allowed to manifest as volumetric strains. The use of the 3-dimensional drainage system prevented undrained conditions from prevailing (i.e. there were no development in excess pore water pressure) confirmed from drained excess porewater pressure after using the cage. It was imperative to maintain drainage conditions throughout the cyclic triaxial tests since effective stresses govern the behaviour of the soil specimens. Moreover, accurate measurement of the dynamic soil properties at high strain levels in cyclic triaxial tests requires proper drainage to prevent development of excess pore water, and accurate measurement of volume changes inside the specimen (Kramer, 2008). It is important to note that differential drainage may take place between the core and the outer layers of the sample. Differential drainage can be quantified by local piezometers / porewater transducers placed in the core and outer surface of the sample.

2.4.5 Applied Static Strain-Controlled Loading

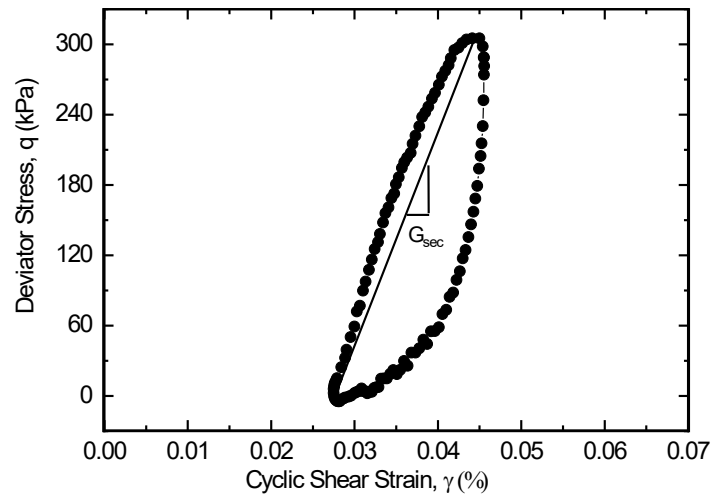
Static failure test was performed to estimate the peak strength of the fouled sub-ballast. In the static displacement-controlled test, the specimen was prepared in accordance with the provisions of ASTM (2011). The specimen was then incrementally confined isotropically to $\sigma_c = 90$ kPa and saturated to B-value ≈ 0.99 (i.e. $\Delta u \approx \Delta \sigma_3$). The sample was then sheared at a constant rate of 0.0045 mm/min.

2.4.6 Applied Cyclic Load-Controlled Loading

Applied loading scheme comprised symmetric one-way load cycles as shown in Fig. 2.5a to mimic the railroad field condition in which a typical sub-ballast soil is subjected to symmetric cyclic loading beneath the ballasted railroads. A typical plot of the measured deviator stress versus the measured cyclic strain is presented in Fig. 2.5b. The provisions of the ASTM D3999-11 (ASTM, 2013) and ASTM D5311 (ASTM, 2004) were followed to determine the secant modulus of shear (G_{sec}), and the damping coefficient (ξ), and to calculate the degradation of specimen's shear modulus (G) and resulting permanent shear strain (γ) of the soil specimen as the cyclic deviatoric stress progressed. Fig. 2.5b shows the hysteresis response obtained for a soil sample during one loading cycle. The hysteretic loop can be described by two parameters that govern its general shape: gradient and breadth. As shown in Fig. 2.5b, the gradient of the loading segment of the loop represents the secant shear modulus (G_{sec}), the breadth of the loop represents the energy dissipated in one cycle (i.e. damping). A total of 1500 cycles of loading and unloading at a rate of 2.5 Hz is shown in Fig. 2.6. The relatively large number of cycles is attributed to the low loading rate compared with the higher loading rates performed on the same soil type, which will be discussed in subsequent sections of this study.



(a)



(b)

Fig. 2.5 Sample cyclic loading: (a) symmetric cyclic one-way loading, (b) typical hysteresis response

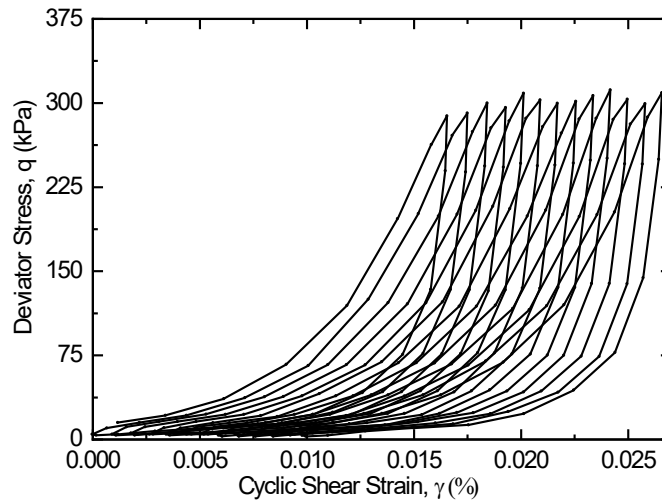


Fig. 2.6 Fouled sub-ballast loaded at a frequency of 2.5 Hz

2.5 Discussion of Static Triaxial Results

This study investigates the effect of train speed on the long-term deformational dynamic behavior of fouled sub-ballast material and the residual stress–strain behaviour of the fouled layer. In order to achieve this objective, the results from the static triaxial tests were used to determine the maximum stress that can be sustained by the specimen, which was then used in the cyclic loading tests. Moreover, the results of static triaxial tests were used to assess the shear stiffness and strength during the cyclic loading tests.

Displacement controlled static triaxial tests were conducted to estimate the peak strength of the fouled sub-ballast specimen, so it could be applied in the cyclic triaxial tests. In the static tests, the samples were prepared following the same procedure used for the cyclic loading tests. However, the load was applied monotonically until failure was achieved. The response of the specimen was monitored at constant confining pressures $\sigma_c = 90$ kPa to simulate actual railroad in situ confining pressure (Ebrahimi, 2011) and at $\sigma_c = 45$ kPa. The initial dry unit weight of the sub-ballast, obtained from the interlayered zone from the track bed of the single-track segment of the Sioux City BNSF railway network, was found to be $\gamma_{dry} = 18.9$ kN/m³.

An illustration of the peak strength of the sub-ballast material can be seen in Fig. 2.7, where the increase in the deviatoric stress with the increase in axial strain under confining pressures of 45 kPa and 90 kPa. As the deviatoric stress increased, considerable structural deformation occurred in the soil specimen, which altered the stress-strain behavior and eventually decreased the monotonic shear strength of the specimen. Thiers and Seed (1969) made similar observations. Based on the axial strain behaviour, the response of the fouled sub-ballast to the applied monotonic load can be categorized into four stages. In stage I, at $q = 100$ kPa and $\varepsilon_{\text{axial}} = 1\%$ the fouled sub-ballast sample demonstrated plastic behaviour. As the applied strain increased, the specimen exhibited almost linear behavior with reduced slope in stage II, which continued to $q = 225$ kPa and $\varepsilon_{\text{axial}} = 4\%$. In stage III, the stress-strain behaviour became clearly nonlinear, and the strain deformation rate increased. In stage IV which extended to $q = 315$ kPa and $\varepsilon_{\text{axial}} = 11\%$, the peak strength of the fouled sub-ballast was reached as the stress remained relatively constant as the strain increased. This behavior is characteristic of granular dense materials and the maximum reached strength defines the peak strength of the soil.

A decrease in slope as the strain level increased indicates the degradation of stiffness at higher strain levels from stage I to stage IV. In addition, the plastic strains occurring in Stages III and IV promote the accumulation of permanent axial strains, which leads to the destabilization of the fouled railroad.

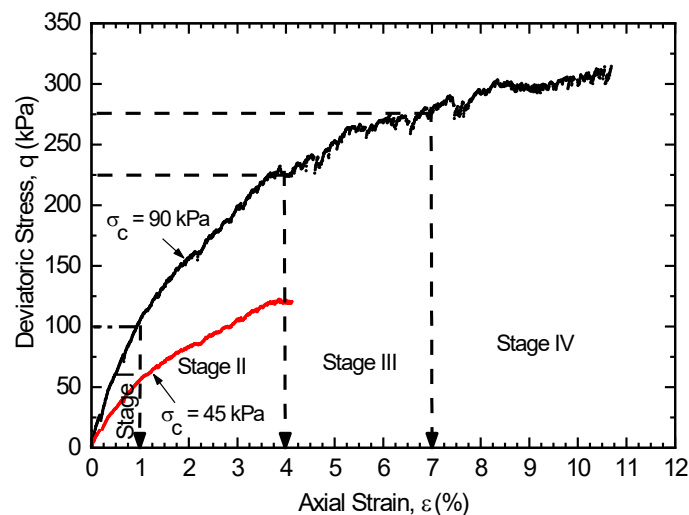


Fig. 2.7 Static response of fouled sub-ballast material for $\sigma_c=45$ kPa and $\sigma_c=90$ kPa

Stress path (q-p) behaviour of fouled sub-ballast during monotonic loading can be seen in Fig. 2.8. As it is noted, the stress path is somewhat nonlinear. It is imperative to recall that the theoretical stress path (q-p) behaviour of consolidated drained granular material is linear. The observed behaviour of the stress path (q-p) is attributed to the presence of the fines in the fouled sub-ballast sample, which hinders the drainage capability of the interlayered sub-ballast specimen. This is mainly because some of the voids between the large particles are filled with fines, which block the drainage paths. In addition, the presence of fines in the skeleton of sub-ballast specimen reduced the direct contact between the large particles, which rendered the interlayered soil specimen highly susceptible to deviatoric and volumetric creep under loading, further inhibiting the dissipation of excess pore water pressure. The results based on the stress paths obtained from the triaxial tests are shown in Fig. 2.8, indicated that the angle of internal friction of the fouled sub-ballast is approximately 40° . The peak strength of the fouled sub-ballast granular materials in triaxial compression is interpreted by the Mohr–Coulomb frictional criterion (Lambe and Whitman, 1969; Wood, 1990; Vardoulakis and Sulem, 1995). As the deviatoric strength increases linearly with the mean effective pressure, the strength due to the particle interlock as a result of the confining pressure being eliminated and the cohesion was found by the cohesion intercept which, obtained from Fig. 2.8, was estimated to be equal 20 kPa.

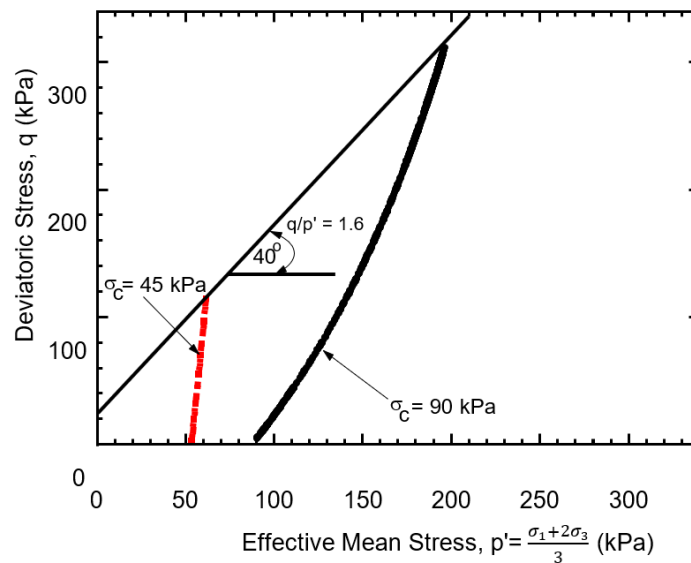


Fig. 2.8 Stress path followed by the fouled sub-ballast specimen

2.6 Analysis of Results from Laboratory Tests

2.6.1 Cyclic Axial and Volumetric Strains

Train speed influences the frequency of its cyclic loading exerted on the ballast, which affects the response of the railroad substructure. Therefore, the cyclical loading was applied at varying frequencies to simulate the loading frequency (Hz) of the train cyclic loading. The loading was applied at frequencies 2.5 Hz, 5.0 Hz and 10 Hz to simulate trains travelling at 32 km/h, 64 km/h, and 128 km/h, respectively (Indraratna et al., 2010). Fig. 2.9 shows the effect of loading frequency on the variation of maximum axial strains with number of loading cycles for the fouled sub-ballast interlayer. Under saturated stress-controlled cyclic loading conditions, an increase specimen axial strain increased, and the developed excess pore water pressure increased as the amplitude of the applied load increased, which caused the shear strain amplitude of the soil specimen to increase progressively as presented in Fig. 2.9. The permanent axial strain and increased excess pore water pressure were accompanied with structural deformations of the soil specimen as the number of cycles increased. Fig. 2.9 provides insights on both transient and permanent strains associated with cyclic loading of fouled sub-ballast material. The elasto-plastic behaviour of fouled sub-ballast is evident in the material behaviour, where simultaneous elastic and plastic strains are found to take place in response to the load applied. The elastic behaviour is demonstrated as transient axial strains which are calculated at a given cycle number and a given permanent axial strain magnitude, as can be seen in Fig. 2.9. At each permanent axial strain amplitude, a recoverable percentage of the strain can be noticed as the load was reversed during the same cycle.

On the other hand, the plastic behaviour is represented as permanent strains, which are determined at zero load crossings (i.e. when there is no load reversal). The permanent strains correspond to the magnitude of the slope of the axial strain vs number of cycle plot which are calculated per stage for a number of cycles. As the loading frequency increased from 2.5 Hz to 10 Hz, the axial transient strain decreased significantly from $\epsilon_{\text{transient}} = \pm 0.2 \%$ to $\epsilon_{\text{transient}} = \pm 0.1 \%$. On the other hand, the residual permanent strain decreased from, $\epsilon_{\text{permanent}} = 2.3 \%$

to 1.8 %. The significant decrease in transient strains and moderate decrease in permanent strain as the loading frequency increase is attributed to a prolonged failure mechanism in comparison with higher loading frequencies so that that can be categorized into three stages as presented in Fig. 2.9. At 5 Hz and 10 Hz the failure took place at 100 cycles and 600 cycles, respectively. In comparison, the sample loaded at 2.5 Hz failure was reached at 1500 cycles. In addition to that, the sample exhibited a yielding behaviour (i.e. prolonged failure mechanism), which cannot be seen in samples tested at 5 Hz and 10 Hz.

With regards the sample loaded at 2.5 Hz, three stages were noted to have distinct rate at which permanent strain increased as the number of cycles progress. For instance, the rate of distortion in axial strain in Stage I was $\delta\epsilon_{\text{permanent}} = 0.05\%$, while for stages II and III, the $\delta\epsilon_{\text{permanent}}$ was found to be 0.002% and 0.0006%. This can be explained by the strain hardening that occurs in the soil material as the numbers of cycles progressed.

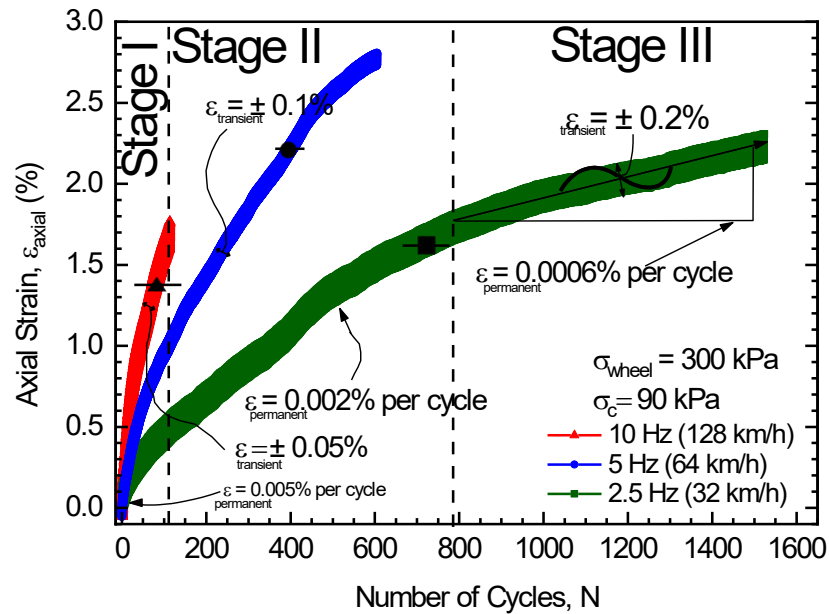


Fig. 2.9 Effect of loading rate on axial strains

The development of the volumetric strain due to the cyclic loading is plotted for the three loading rates in Fig. 2.10. It is evident that the drained conditions prevailed in the samples that were tested, since the $\delta\epsilon_{\text{vol}} > 0$, which is always the case in drained tests. During the first 50

cycles, the rate of change in volumetric strain of the samples loaded at 2.5Hz, 5 Hz and 10 Hz increased steadily at the same rate. However, the rate of change in volumetric strain for the sample loaded at 2.5 Hz started to slow down compared to the samples loaded at 5 Hz, and 10 Hz. It is observed that the increase in the loading frequency resulted in an increase in volumetric creep. This is because at a lower loading rate (i.e. 2.5 Hz) longer time was provided between the cycles for drainage.

As the loading frequency decreased, the fouled sub-ballast material exhibited smaller volumetric deformation, which resulted in increased number of cycles to failure. The soil sample loaded at a frequency of 2.5 Hz exhibited distinct evolution of volumetric strain. For the fouled sub-ballast sample cyclically tested at failure stress levels (300 kPa), with a loading rate of 2.5 Hz the volumetric strain rate is slower (smaller gradient) compared to the samples loaded at 5.0 and 10 Hz. This is because the volumetric strain reached at the end of the test where the sample that was loaded at 5 Hz was found to be -2.8 %, while the final volumetric strain resulted to be -1.8% for the sample loaded at 2.5 Hz, which is 1.5 times less than the sample loaded at 5 Hz. This can be explained by the mud pumping phenomenon (voided cross-ties) that takes place at the fouled track segments. Results indicated that trains travelling at 64 km/h are likely to initiate the mud pumping underneath the superstructure, causing sub-ballast material to be pumped out from underneath the railroad, which was observed in the fluidization of the sample post failure. Thus, the final volumetric strain for the sample that was loaded at 5 Hz is higher than the sample loaded at 2.5 Hz. This finding was confirmed by the discoloration of drained excess pore water from the sample loaded at 5 Hz.

Results indicated that as the loading frequency (which could be considered proxy for train speeds) increases, the faster is the rate of permanent damage that occurs to the infrastructure. In other words, the faster the trains are, the more likely is the irrecoverable damage that occurs to the infrastructure. However, the rate of deterioration decreased as the number of cycles progressed. Which suggests that the longer and the slower the trains are, the less the deterioration that might take place due to the mud pumping phenomenon. In addition to that, according to Suiker et al. (2005) over consolidation was noticed to take place as early as the

first cycle in the tested sub-ballast samples at various confining pressures, which was explained as the reason behind the volume reduction. However, the magnitude of the volumetric strain shown in this study exceed what have been reported by Suiker et al. (2005), where the maximum volumetric strain reported was -0.035 % for the uncontaminated sub-ballast sample confined at 69 kPa loaded at 5Hz with an applied load (which can be considered proxy for train wheel load) of an approximately 238 kPa. In this study, the cyclical behaviour of fouled railroad sub-ballast with 5 % fine contamination was investigated, the volumetric strain reached at the end of the test where the sample that was loaded at 5 Hz was found to be -8.5%. While investigating the effect of confining pressure on the volumetric strain of clean sub-ballast, Suiker et al. (2005) noted a further 28% reduction in the volumetric strain when the confining pressure was increased from 41 kPa to 69 kPa. As explained before, the high compaction susceptibility originates from the well graded particle gradation of the sub-ballast material.

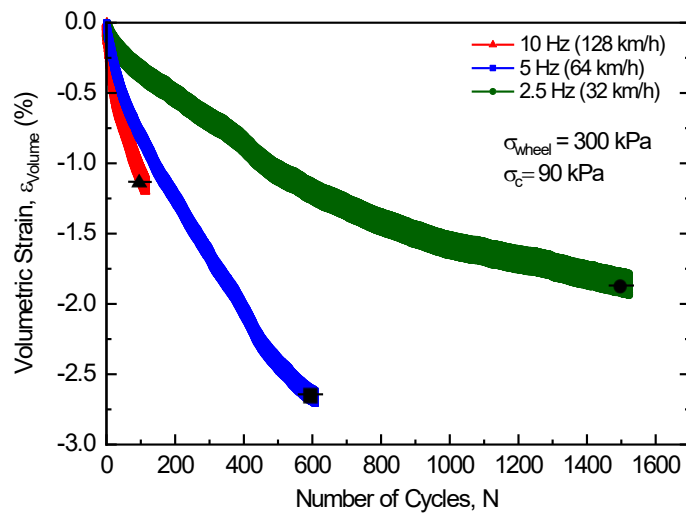


Fig. 2.10 Effect of loading rate on volumetric strains

2.6.2 Consolidation Parameters of Fouled Sub-ballast

Suiker et al. (2005) noted a significant reduction in the volumetric strain when the confining pressure was increased from 41 kPa to 69 kPa, which was attributed to the high compaction susceptibility of the sub-ballast material that originates from the well graded particle size distribution. Similarly, the fouled sub-ballast is also characterized by the well graded particle size distribution. Therefore, one-dimensional oedometer tests were performed to provide quantitative results regarding the deformation behaviour axially while the fouled sub-ballast specimens were restrained against radial strain. The provisions of the ASTM D2435-70 were followed in all performed consolidation tests. The specimen tested at 5% moisture content typical of a saturated railroad condition was allowed to drain in which the excess pore water pressure is permitted to dissipate, whilst the load is applied axially. The dissipation of excess pore water pressure was allowed due to the presence of cohesive clay fines contaminating the granular sub-ballast. Fig. 2.11 shows that the effect of the applied stress on the void's ratio of the fouled sub-ballast sample was minimal. For example, the void ratio was 0.465 for an applied stress of 5 kPa and was 0.405 for applied stress of 1600 kPa.

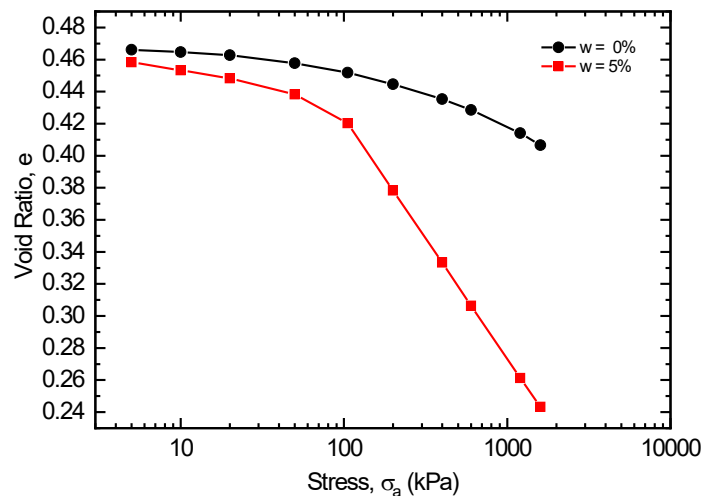


Fig. 2.11 Void ratio variation of fouled sub-ballast with consolidation stress

Consolidation parameters, coefficient of consolidation C_v and m_v , are stress dependent, which makes them important in the prediction of railroad settlement. Thus, representative consolidation parameters for determining the rate of settlement and total settlement, must be determined based on the estimated applied stress and the moisture content using Fig. 2.11. The coefficient of consolidation C_v for each loading increment is shown in Fig. 2.12a, which has been derived from Terzaghi (1925) 1-D consolidation theory. The coefficient of consolidation C_v is used to determine the percent of the total primary settlement completed at any time, and is calculated by Casagrande's log time method, i.e.:

$$C_v = \frac{0.197 H^2}{t_{50}} \dots\dots\dots \text{Equation 2.1}$$

Where, H is the maximum drainage path, and t is the time when the degree of consolidation $U = 50\%$.

In general, C_v decreases with the applied pressure for the fouled sub-ballast samples in dry and wet conditions. However, as the moisture content was increased to 5 %, typical of moisture content in fouled rail roads, C_v decreased considerably, compared to dry conditions, as the incremental application of stress progresses. The low values of C_v for the fouled sub-ballast with moisture content of 5 % are primarily due to the lower void ratios, which are evident in Fig. 2.12a. The results indicated that the smaller the change in the void ratios, initially, C_v remained constant for both wet and dry fouled sub-ballast samples. This can be explained by the notion that the coefficient of volume compressibility m_v decreases in a comparable trend so that the void ratio remains constant.

General trend noticed in Fig. 2.12b is that the fouled sub-ballast specimen with moisture content of 5 % was more compressible than dry fouled sub-ballast. In addition to that, it was also noticed that volume compressibility decreased with the applied pressure, nevertheless, at approximately 100 kPa the coefficient of compressibility m_v plateaued for both wet and dry fouled sub-ballast samples. This indicates a drastic drop in the void ratio e and the coefficient of consolidation C_v . However, beyond 100 kPa, coefficient of compressibility m_v continued to decrease but at an extremely low rate, as the increments of applied load progress, meanwhile both void ratio e and the coefficient of consolidation C_v dropped at a faster rate, this means that

the fouled sub-ballast layer was rendered almost incompressible, and the particles have reached a state of over-consolidation.

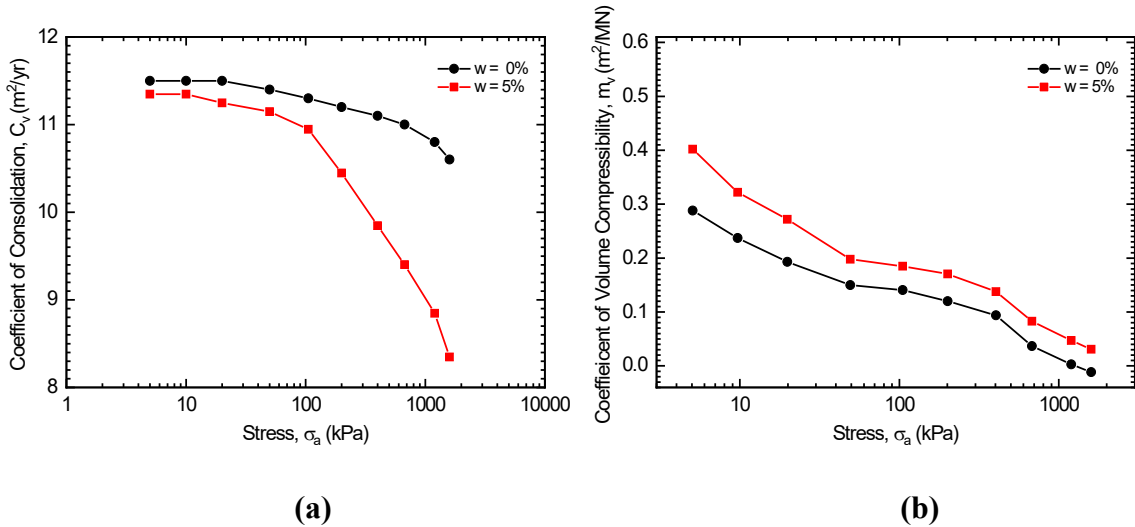


Fig. 2.12 C_v and m_v variation of fouled sub-ballast with consolidation stress: (a) coefficient of consolidation C_v , (b) coefficient of volume compressibility m_v

2.6.3 Shear Modulus Corresponding to Shear Wave Velocity Measurements

Shear wave velocity of the fouled sub-ballast material was measured in dry conditions and at a moisture content of 5 % typical to a wet railroad condition by utilizing the oedometer consolidation cell coupled with piezo-electric ring actuator system (Ahmad, 2016; Ethier et al., 2016). In general, the noticed behaviour in Fig. 2.13 is that the fouled sub-ballast with moisture content of 5 % resulted with a faster shear wave velocity measurement compared with the dry fouled sub-ballast sample, as the applied stress progressed. This is explained by the densification that occurred to the sub-ballast layer beneath the railroad as a result of the applied cyclic loading. Suiker et al. (2005) observed a similar compaction behaviour of the cyclically tested sub-ballast layer, but with rather smaller magnitudes, manifested in volume changes of the sub-ballast samples. however, there were no reference to the density attained due to the compaction. In addition to that, it was noticed that the increase in shear wave velocity in

response to the applied stress was linear up to 100 kPa, after which the non-linearity prevails until the maximum applied stress of 1600 was attained.

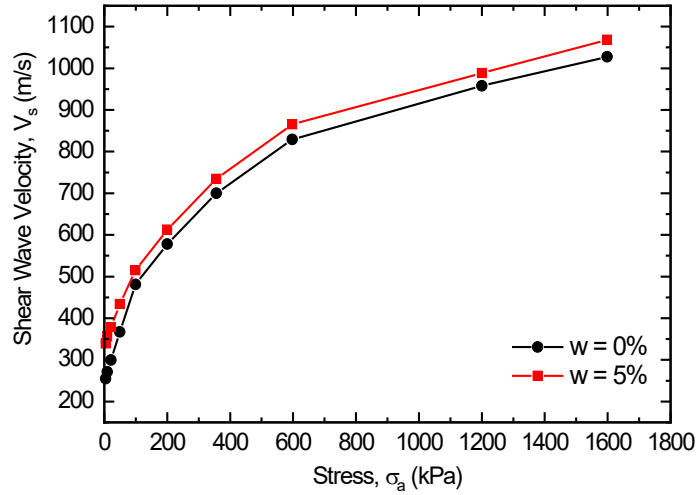


Fig. 2.13 Shear wave velocity variation of fouled sub-ballast with consolidation stress

Measured shear wave velocity values were used to estimate the maximum Shear Modulus, G_0 , of sub-ballast material, i.e.

$$G_{max} = \rho V_s^2 \dots \dots \dots \text{Equation 2.2}$$

Where, G_{max} is the soil shear modulus obtained at very low strain ($<10^{-3}$ %).

Variation of the maximum shear modulus G_0 of the fouled sub-ballast (at 5 % and 0 % moisture content) in response to various applied consolidation stress was estimated using *Equation 2.2*. The estimated maximum shear modulus of the fouled sub-ballast sample is illustrated in Fig. 2.14. The maximum shear modulus estimated using shear wave velocity measurements was in agreement with the findings regarding the coefficient of consolidation C_v , the coefficient of volume compressibility m_v , and the void ratio e . The overall behaviour of the wet and dry fouled sub-ballast samples followed an ascending trend in response to the applied consolidation stress. It was noticed that using *Equation 2.2*, the nonlinear behaviour began to affect the shear

modulus at 200 kPa. This can be explained in terms of the volumetric compressibility of the fouled sub-ballast specimen m_v . The volumetric compressibility at 200 kPa plateaus for both wet and dry fouled sub-ballast samples due to the reduction in the void ratio e . Beyond the applied consolidation stress of 200 kPa, the specimens of the fouled sub-ballast specimen were almost incompressible, and the increase in the shear modulus is said to be attributed to particle rearrangement and particle interlock.

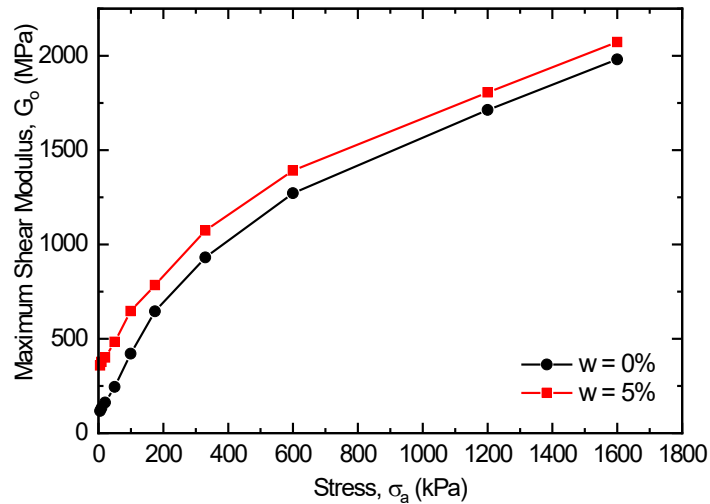


Fig. 2.14 G_0 variation of fouled sub-ballast with consolidation stress

2.6.4 Shear Modulus Corresponding to Cyclic Loading

Secant shear modulus from cyclic triaxial tests was calculated at certain shear strain amplitudes as the cyclic deviatoric stress was applied to the specimen. The measured deviator stress is plotted versus the measured cyclic strain to represent the hysteretic behavior of the sample during the cyclic loading. The analysis of the produced hysteresis loops involved two aspects: the stress path for the hysteretic loop and the general shape of the loop in terms of its inclination and breadth. The stress path followed by the loop determines the cyclic model that governs the stress-strain behavior of cyclically loaded soils. Although the equivalent linear model is limited in its applicability, it is commonly used because of its simplicity and practicality. On the other

hand, the cyclic nonlinear models and advanced constitutive models are difficult to calibrate and time consuming to apply, which renders them unusable (Kramer, 2008).

The equivalent linear model was used to calculate the dynamic properties of the ballast-sub-ballast interlayered soil as a linear viscoelastic material. The secant shear modulus (G_{sec}) was acquired from the inclination of the loops at specific cyclic strain amplitudes, where a line is drawn joining both ends of the loops (See Fig. 2.5b). The inclination of the loop defines the secant shear modulus (G_{sec}) of the soil specimen for that cycle. The secant shear modulus (G_{sec}) represents the average of all the tangent shear moduli corresponding to the shear strain amplitudes corresponding to the specific stress reversal of that cycle. The cyclic loading test results demonstrated that as the loading frequency varied from 2.5 Hz, 5.0 Hz to 10 Hz, the size of the hysteresis loops varied, along with the shear strain amplitudes in response to the cyclic loading. As the cyclic strain increases, the secant shear modulus would decrease. The shear modulus ratio was calculated by normalizing the shear modulus (G_{sec}) with respect to the maximum shear modulus (G_{max}), which was calculated from measured shear wave velocity using *Equation 2.2*. Fig. 2.15 illustrates the effect of loading rate on modulus reduction behavior of interlayered sub-ballast soil contaminated with cohesive fines. The graph shows the degradation of the normalized shear modulus of the of interlayered sub-ballast soil at the interface between fouled ballast and sub-ballast at different loading rates at an applied wheel load stress of 300 kPa, and confining pressure of 90 kPa.

Fig. 2.15 illustrates that soil plasticity and effective confining pressure are not the only important parameters that shape the shear degradation curves but also the loading rate, and particle size play a major role in determining the shear modulus of soils. Similar observations were made by Seed et al. (1986) and Kramer (2008). The linear cyclic threshold shear strain ($\gamma_{0.7}$), defined as the cyclic shear strain for the normalized shear modulus degradation factor $\frac{G}{G_{max}} = 0.7$ (Santos and A, 2000; Correia et al., 2001), is an important parameter.

Modulus reduction behavior is influenced by the loading frequency, which can be seen by its effect on the linear cyclic threshold shear strain (γ_{tl}). The linear cyclic threshold shear strain

(γ_{tl}) characterizes the degree of non-linearity for medium-high strain level of soils. The linear cyclic threshold shear strain, (γ_{tl}), is greater at high effective confining pressure than at low effective confining pressure. This is evident in Fig. 2.15, where loading frequency of 2.5 Hz resulted in a cyclic threshold shear strain twice that for a specimen loaded at a frequency of 5 Hz. This is attributed to the fact that cyclic stresses applied at a slower rate allow excess pore water pressure to dissipate, thus maintain effective confining stresses and the shear modulus as can be seen in stage II in Fig. 2.15. Kokusho et al. (1982), Dobry and Vucetic (1987), Sun et al. (1988), and Kramer (2008) suggested that the shear degradation modulus of cohesive soil is influenced by its plasticity index. However, they did not comment on the influence of the cyclic loading rate (frequency) on the shape of the shear degradation curve.

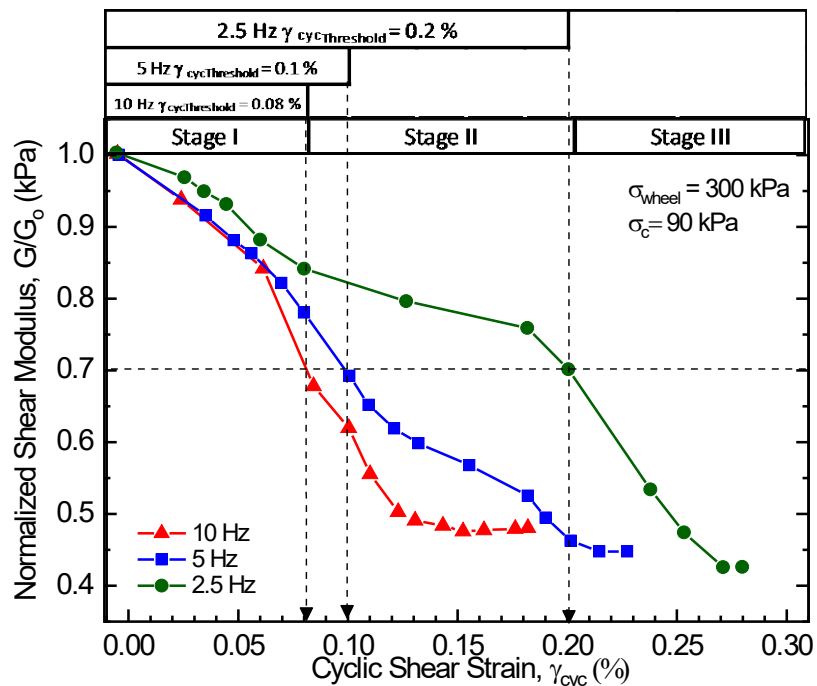


Fig. 2.15 Effect of loading rate on the shear modulus degradation curves

Soil specimen loaded at lower frequency exhibited a prolonged failure mechanism, where the shear stress amplitude was observed to decrease with the increase of number of cycles. This

illustrates the tendency of progressive cyclic loading to degrade the stiffness of the specimen. The prolonged failure criterion can be explained by the high shear resistance of the soil specimen, which is in part due to the presence of highly angular granular particles that are characterized with high internal friction angle. Similar results were reported by Liu. et al. (2014) where the shear strain buildup leads to a prolonged failure mechanism, where particle reorientation and displacement consequently leads to settlement of the sub-ballast and subgrade beneath the railroad.

Soil sample loaded at a frequency of 2.5 Hz exhibited 3 distinct shear modulus degradation stages, unlike the samples loaded at 5 Hz and 10 Hz. The lower loading frequency allowed the sample to sustain a larger number of load cycles (lower degradation rate in strength and stiffness) due to the dissipation of the developed excess pore water pressure. For example, at shear strain of 0.18 % the sample loaded at 2.5Hz has lost only 20 % of its shear strength while the sample loaded at frequency of 10 Hz has reached its residual shear modulus (which was about 50 % of its maximum shear modulus), for the same amplitude of shear strain.

A soil specimen loaded at a frequency of 2.5 Hz, exhibited the lowest residual shear modulus; 40 % of its maximum shear modulus, unlike the samples loaded at 5Hz and 10Hz, which ended with 45% and 50% residual strength. In other words, the soil specimen loaded at a frequency of 2.5 Hz, mobilized most of its shear strength to resist the effect of deviatoric stresses on the cyclic strain. This can be clearly seen in Fig. 2.15 where the soil specimen loaded at a frequency of 2.5 Hz demonstrated a prolonged failure criterion, causing it to mobilize its entire shear strength. Furthermore, results shown in Fig. 2.15 have indicated that the sample loaded at 2.5Hz, proxy for trains travelling at 32 km/h, has demonstrated the lowest degradation rate in shear modulus (at around 80% G_{max}) compared with samples loaded at 5 Hz and 10 Hz, proxy for trains travelling at 64 km/h, and 128 km/h, respectively.

2.6.5 Damping Ratio

When trains pass over the fine-contaminated ballasted railroad segments, subsequent soil layers are cyclically loaded. This cyclic loading energy is dissipated by the soil into the free-

particle matrix. As a result, the efficiency of the sub-ballast layer in energy dissipation decreased as the train cars pass over fouled railroad segments.

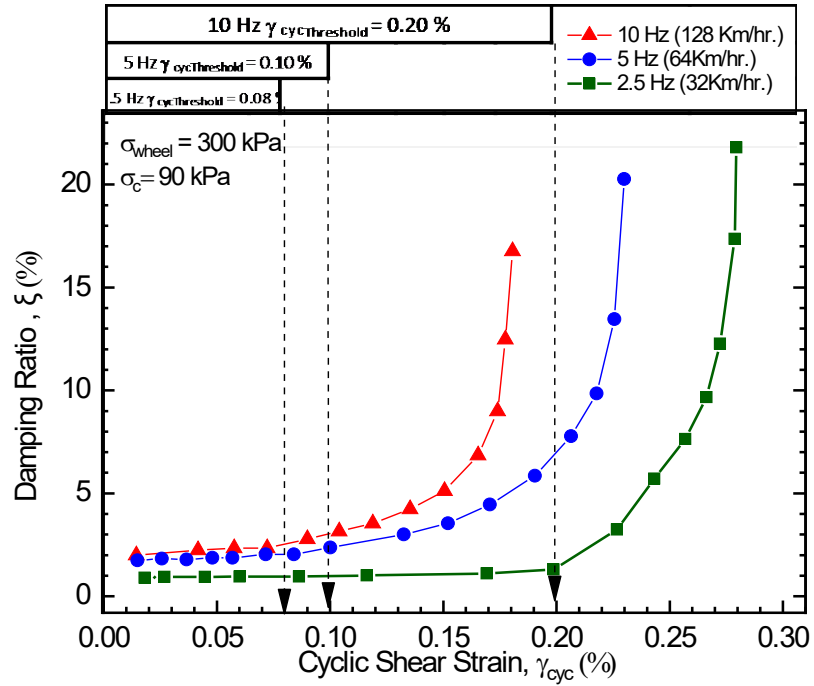


Fig. 2.16 Effect of loading rate on the damping ratio

Kramer (2008) suggested that the damping behaviour of cohesive soils is governed by the relative density, plasticity index and confining pressure. Moreover, Seed et al. (1986), Yasuda and Matsumoto (1993), and Kramer (2008) stated that the damping behaviour of granular soil (PI=0) is similar, and the damping curves in Fig. 2.17 can be applied regardless of particle size. However, results have shown that the cohesive-granular soil specimens with a non-uniform particle size distribution, and Plasticity Index = 10 exhibited a behavior different than observed in Fig. 2.17. The findings have illustrated that the particle size distribution is an important influencing parameter on the damping behaviour of cohesive-granular soils characterized with non-uniform particle size distribution.

Most importantly, results have shown that soil plasticity and effective confining pressure, and relative density are not the only important factors shaping the damping curves as stated by Seed et al. (1986), Yasuda and Matsumoto (1993), and Kramer (2008), but also the loading

rate and particle size; both parameters play a major role in determining the damping behaviour. The loading rate effects the rate of degradation in the shear strength of the fouled sub-ballast, which affects the stress path followed during loading and unloading of the specimen, resulting with a unique damping behaviour specific to that stress-strain path. On the other hand, particle size affects the interparticle behavior upon loading and unloading. In saturated conditions, when voids are filled with fines and water the friction between the larger particles is reduced, causing more energy to be dissipated. However, when the loading rate is increased, the energy dissipation process takes place at faster rate causing distortion in the sub-ballast particle matrix, decreasing the efficiency of sub-ballast in dissipating the energy produced by the train cars passing over fouled railroad segments.

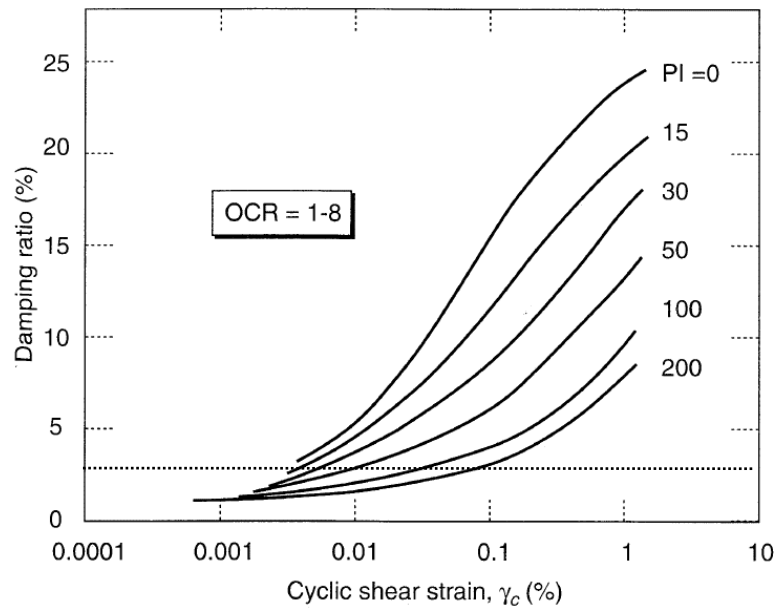


Fig. 2.17 Effect of Plasticity on the Damping Ratio of Soils (Vucetic and Dobry, 1991)

2.7 Practical Implications

At 90 kPa effective confining pressure, (typical of the track environment) with fines fouling the track with a Plasticity Index = 10, there is a significant effect on the dynamic properties of the sub-ballast, and consequently the ballast. As a result, the free-draining characteristics of the ballast is compromised, although the permeability and drainage behaviour of the sub-ballast

have not been considered within the scope of this study. It is recommended that, at fouled railroad segments, railway operators should restrict train speeds exerting average wheel stress in the range of 300 kPa, to a maximum of 32 km/h unless in-situ dynamic characterization proved otherwise. The speed limit is set to preserve 80% of the shear modulus of the sub-ballast and prevent further damage to railroad substructure and to maintain railroad integrity.

It is imperative to maintain the shear modulus of the track bed of at least 80% of G_{max} in order to minimize maintenance tamping operations to recover lost confinement, and to prevent further degradation of the stability of the tracked. This can be achieved by the help of the slow passing trains that can apply effective stresses to the railroad substructure, thus conserving the shear modulus of the track bed, consequently resulting with a higher linear cyclic threshold shear strain, (γ_{tl}). Trains travelling through fouled railroads ought to decrease their speed to a maximum of 32 km/h, so that excess pore water pressure is allowed to dissipate, thus ensuing high effective confining stresses are applied to the track bed.

2.8 Summary

A static triaxial test and a series of cyclic triaxial tests were conducted on different sub-ballast soil samples to investigate the dynamic geo-mechanical behaviour and characteristics of fouled railroad sub-ballast under static and cyclic loading. The studied operational factor (train speed) effecting the behavior of fouled railroad in terms of the response of the railroad substructure as a result of the applied cyclical loading was conducted by manipulating the loading frequency (Hz) of the ram in the triaxial machine. The magnitude of frequencies that were applied was 2.5 Hz, 5.0 Hz and 10 Hz to simulate train cars travelling at 32 km/h, 64 km/h, and 128 km/h, respectively (Indraratna et al., 2010). In addition, the cyclic responses from the parametric study were presented in the results. Results are presented in in terms of time history, strain, and number of cycles.

An important railway operational factor (train speed) influencing the stress-strain behavior during the cyclic loading of the fouled sub-ballast interlayer zone was investigated and summarized. This study focused on the role of the sub-ballast in the railroad degradation

process, by studying the effect of simulated train speed on fouled sub-ballast samples. The results of the study cautioned railway operators to practice restraint regarding train speed travelling on fouled railroad segments. It is recommended that the maximum speed of trains in fouled zones be limited to a maximum of 32 km/h. The major findings from the results of the laboratory tests are summarized:

(i) Under stress controlled cyclic loading conditions, axial strains endured by the soil specimen and the generation of excess pore water pressure (observed by the low volume of collected excess pore water) the cause the shear strain amplitude of the soil specimen to increase progressively.

(ii) Soil plasticity and confining pressure are not the only important factors shaping the damping curves, but also the loading rate, and particle size play a major role in determining the damping behaviour in the case of the sub-ballast.

(iii) Permanent axial strain and poor excess pore water pressure dissipation were accompanied with structural deformations of the soil specimen as the number of cycles was increased.

(iv) In response to the change of the loading rate, the sizes of the hysteresis loops were found to vary, along with the shear strain amplitudes of the cyclic loading.

(v) Although the sub-ballast specimen under different loading rates exhibited prolonged failure mechanism, the shear stress amplitude was observed to decrease with the increasing number of cycles.

(vi) Sub-ballast specimen loaded at a frequency of 2.5 Hz, simulating a train passing by over the fouled railroad segment with a speed of 32 km/h, exhibited 3 distinct shear modulus degradation stages, due to its prolonged failure behaviour, unlike the samples loaded at 5Hz and 10Hz, which were characterized by faster failure response.

(vii) Sub-ballast specimen loaded at a frequency of 2.5 Hz, mobilized most of its shear strength to resist the effect deviatoric stresses on its cyclic strain.

(viii) Before the threshold strain level ($\gamma_{0.7}$)= 0.08 %, 0.1 %, and 0.2 %, the Damping Ratio (ξ) ranged between 1% - 2 % for the soil specimens loaded at 2.5 Hz, 5 Hz, and 10 Hz, respectively.

(ix) Damping Ratio (ξ) was noticed to increase exponentially for the specimens loaded at 2.5Hz, 5Hz, and 10Hz.

(x) Soil plasticity and effective confining pressure, and density are not the only important factors shaping the damping curves, but also the loading rate, and particle size play a major role in determining the damping behaviour.

Chapter 3

3 In-situ Performance Assessment of Track Superstructure on Fouled Railroad²

3.1 General

Ballasted railroads are efficient load transfer infrastructures. They are typically constructed utilizing clean, angular, uniform, large grain particles in order to distribute train loads effectively to underlying subgrade (FederalRailroadAdminstration, 2020). Excellent performance of ballasted railroads ensures that heavy freight trains can safely travel through the railway network. They transmit cyclic loads from the superstructure (rails, and cross-ties) through the substructure (ballast, sub-ballast) to native soil (Selig and Waters, 1994). In addition, construction costs of ballasted railroads is lower than other roadbed foundation alternatives such as ballast-less or slab track (Esveld, 2001). Their excellent performance is attributed to the superior mechanical ballast characteristics (i.e., shear strength and permeability) and dynamic response features such as energy dissipation and reduced vibrations. Nevertheless, ballast and sub-ballast integrity could be compromised due to increased traffic demand, including heavier axle loads (Ebrahimi et al., 2014; Bian et al., 2016), faster train speeds (Lamas-Lopez et al., 2017; Lazorenko et al., 2019) and longer rolling stock (number of cycles).

Ballasted railway tracks are severely affected by hindered drainage due to fouling (Li and Selig, 1998; Selig and Cantrell, 2001). Poor drainage can be caused by ballast and sub-ballast fouling, which is caused by fines migration upwards into the sub-ballast and ballast under hydraulic pressure, filling the voids. Fouling impedes ballast permeability and reduces the system's overall load bearing capacity (Tennakoon et al., 2012; Indraratna et al., 2013;

² A version of this chapter has been published in the Journal of Transportation Geotechnics: Touqan, M., El Nagggar, M. H., & Stark, T. D. (2022). In-situ performance assessment of track superstructure on fouled railroad. *Transportation Geotechnics*, 32, 100695

Hudson et al., 2016). Fig. 3.1 shows the intrusion of clayey-silty subgrade particles into overlaying ballast. Fouling has been investigated widely (Machii, 1978; Ayres, 1986; Selig and Waters, 1994; Raymond, 1999; Sussmann et al., 2001; Burns et al., 2006; Ghataora et al., 2006; Indraratna et al., 2011; Duong et al., 2014). Several studies reported different causes for substructure fouling. For instance, Selig and Waters (1994) attributed most fouling sources to be particle attrition (category II), since the European standards require a sub-ballast layer to be placed below the ballast to prevent subgrade intrusion. Nonetheless, the study still recognized subgrade material as a source of fouling (category V), primarily through subgrade intrusion and consequent slurry pumping. Takatoshi (1997) attributed fouling to negative pore pressure developed in the ballast during cyclical loading and unloading, which causes fines to move upwards towards the ballast. Raymond (1986) suggested that freeze–thaw cycles could draw fines to the surface, especially in railroads that stretch on clayey and silty ground surfaces.

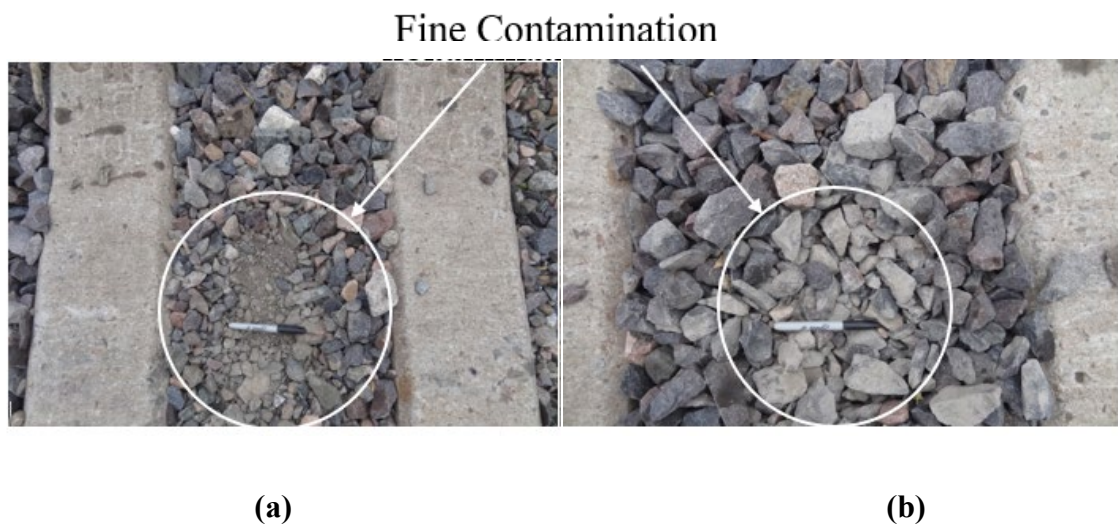


Fig. 3.1 Fines surfaced at Parkville, MO, fouled site: (a) Fines surfaced between cross-ties, (b) Close-up on fines

Inadequate performance of fouled ballast can alter track geometry and accelerate deterioration of components of the railroad superstructure, which may lead to voided cross-tie (Li and Selig, 1998; Selig and Cantrell, 2001). Voided cross-ties are caused by slurry pumping underneath due to cyclic loading on the cross-ties, which results in poor cross-tie support or even lack of

support and consequently overloads neighboring supported cross-ties. Cross-ties provide stringent gauge restraint and transmit vertical loads to the ballast. Thus, poor cross-ties support can lead to loss of alignment and severe changes in the longitudinal profile of the tracks due to plastic deformation accumulation.

Several studies investigated the effect of environmental conditions on track substructure. Trinh et al. (2012) investigated the effect of water content on the mechanical behavior of uncontaminated track bed using dynamic triaxial tests. They reported that samples with low moisture content exhibited higher shear strength, while fully saturated specimens failed after one load cycle. Duong et al. (2014) investigated the effect of moisture content on the track substructure interlayering between the ballast and sub-ballast, and the behaviour of formed interlayer through field monitoring of instrumented track segment. They demonstrated that the increase in water content reduced interlayer's shear strength and drastically increased its permanent strains. The saturated interlayer experienced a drastic drop in resilient modulus shear strength and deteriorated mechanical performance. Tamrakar (2017) evaluated the impact of fines on the moisture content of flexible pavement base materials and railroad ballast and reported that fouled ballast physical properties changed due to increased moisture content, which reduced shear strength of both flexible base materials and railroad ballast. Esmaeili et al. (2017); Esmaeili et al. (2019) investigated the mechanical behavior of sand-fouled ballast with and without TDAs (tire-derived aggregates). Results showed that for sand-fouled non-TDA samples; settlement decreased, and stiffness and damping increased at a MC of 5%. While at 10% MC, sample stiffness was lower, and settlement and damping were higher when compared with the samples at 5% MC.

A number of studies have investigated the effect of moisture on the wheel-rail interface in dew and damp conditions (Zhu et al., 2013; White et al., 2018; Wu et al., 2019). Rossetti (2002) investigated the potential impacts of climate change on the superstructure components of railroads and reported that heat kinks can cause track misalignments, and in extreme cases, train derailments. Also, direct solar radiation on railroad tracks may cause uneven thermal expansion when shade covers nearby sections, thus causing track warp to freight traffic.

However, the effect of the environmental conditions on the response of the railroad systems was not quantified.

Operational factors such as train speed and applied axle load influence the behaviour of railway substructure. Haque et al. (2007) studied the effect of cyclic loading frequency (proxy for train speed) on the sub-ballast filtration and evaluated the migration process of fines from the subgrade. They presented the results in terms of piping ratio (D_{15}/d_{85} , where D_{15} is the sub-ballast particle size corresponding to the 15th percentile finer and d_{85} is the subgrade particle size corresponding to the 85th percentile finer). The fines infiltration from subgrade decreased for a piping ratio less than 9 under cyclic loading frequency of 10 Hz and confining pressure between 70-140 kPa. Lamas-Lopez et al. (2016) found that the resilient modulus of the uncontaminated sub-ballast layer decreased by 25% as train speed increased from 60 km/h to 200 km/h. In a similar study, Lamas-Lopez et al. (2017) reported no change in damping ratio (D_r) of the uncontaminated sub-ballast layer as train speed increased from 100 km/h to 200 km/h. Although both studies gave valuable insights into the sub-ballast layer dynamic properties, they were applicable to clean uncontaminated sub-ballast. Sun et al. (2014) monitored permanent deformation mechanisms and particle breakage due to simulated train trafficking with a range of train speeds from 40 km/h to 400 km/h. Azizi et al. (2021) suggested that train speed should be limited to 70 km/h and 50 km/h to improve the comfort index for fouled ballast beds with one voided cross-tie and two voided cross-ties, respectively. Tamrakar (2017) studied the impact of fines content on the mechanical performance of flexible pavement base materials and railroad ballast. Tournay et al. (2017) quantified the rail foot stresses and associated high values with rail failure due to typical rail defects and reported higher stresses in the rails base in summer compared to winter, which was attributed to soft static track stiffness during summer and stiff condition of frozen ballast during winter.

Chapter 2 investigated static and dynamic characteristics of a fouled sub-ballast material considering train speed using static and cyclic triaxial tests. They recommended that the maximum speed of trains in severely fouled railroad segments be limited to a maximum of 32 km/h (corresponding to frequency of 2.5 Hz) to minimize the degradation rate in shear modulus

(at around 80% G_{max}). Liu et al. (2019) employed a ballast-like 3D printed battery-powered wireless smart rock to record its movement in real time at fouled spots of railroad track. Results indicated that poorly supported cross-ties in fouled section experienced higher peak accelerations and a gradual decrease in acceleration when unloaded, while cross-ties in clean sections had smaller peak accelerations.

Current onboard Vehicle Track Interaction (VTI) sensors continuously measure lateral and longitudinal track irregularities, and alert railroad operators once values reach certain thresholds. However, such systems do not capture the dynamic response of the railroad system or the superstructure due to train passby loading and unloading and can not determine railroad substructure in-situ conditions. Train mounted VTD (Vehicle Track Deflection) instruments depend on rail-bending measured to evaluate static track stiffness and bending moment. However, because rail bending is affected by environmental conditions, using only onboard (VTI) systems complicates choosing the most effective remedial measures of railroad superstructure (Wilk et al., 2016).

The dynamic response of ballasted railway tracks is typically estimated using pseudo-static approaches based on static loads obtained from field tests and then dynamic coefficients are applied from design manuals (Esveld, 2001; Kaewunruen and Remennikov, 2004; Kaewunruen and Remennikov, 2005; Kaewunruen and Remennikov, 2005; Öberg, 2006). However, these approaches are unreliable because of rail corrugations, irregularities, and cross-tie excessive localized settlement (voided cross-tie) (Esveld, 2001; Kaewunruen and Remennikov, 2007; Lichtberger, 2010). Several studies quantified the degree of cross-tie support of fouled rail tracks using tie load ratio (Chang et al., 1980; Stark et al., 2015; Wolf, 2015; Stark and Wilk, 2016; Wilk, 2017). However, their findings were limited to the instrumented tie local performance. In addition, rail deflection and static track stiffness were not assessed and the effect of surrounding conditions on superstructure performance was not studied.

In the current study, the performance of superstructure components of fouled railway track is investigated and correlated with surrounding conditions influencing fouled ballast bed

performance. Moreover, a feasible method is presented to infer the state of concrete cross-tie support conditions of the cross-tie array adjacent to the instrumented segment. The measurements from sensors attached to the rail supported by concrete cross-ties were used to provide meaningful information such as longitudinal range of influence of loads on the rail and the uplift ratio.

3.2 Objectives and Scope of Work

This study investigates dynamic behaviour of railroad substructure through field monitoring of fouled railroad segments during trains travel. The main objective is to quantify the deformational behaviour of railroad substructure due to heavy haul trains travelling in adverse environmental conditions. A total of 32 heavy haul freight trains (including rolling stock data) were monitored and corresponding superstructure response has been analyzed. However, time histories of measured responses for only four selected trains were analyzed as typical results of the measured responses. Measured data for four trains were based on front locomotives of the rolling stock. Monitored trains travelled through the section on: 20/Dec/2017-15:15, 31/Dec/2017-14:22, 20/Jan/2018-12:23 and 20/Jan/2018-16:32, hereafter referred to as: Train 1, Train 2, Train 3, and Train 4, respectively.

Superstructure response due to trains traversing fouled track was analyzed during periods of extremely high and low temperatures and relatively high/low track moisture content. Effects of environmental conditions on railroad response are analyzed by quantifying the deflection of railroad superstructure elements (rails and cross-ties) at vulnerable (fouled) segments. Critical environmental parameters are identified by studying excessive dynamic responses of these elements. The long duration of this study ensures data is gathered throughout the four seasons and ascertains repeatability and accuracy of inferred results. Qualitative and quantitative insights are provided with regards to the cross-tie support efficiency. Correspondingly, recommendations are provided to manage trains travelling on fouled railroad segments in critical weather conditions. Finally, the dynamic response of fouled railroad is compared using analytical solutions, which are then utilized to establish static track stiffness.

3.3 Site Profile and Track Instrumentation

3.3.1 Site and Soil Profile

The fouled railroad test segment was located in the North-Western part of Parkville, Missouri, USA (39°11'22.6"N 94°41'21.1"W). The instrumented fouled site was a 281m single track segment of the 175 km Sioux City BNSF railway network as shown in Fig. 3.2.

The ballast and underlying sub-ballast were characterized in a laboratory study (Chapter 2) The mechanical properties of the fouled material were evaluated following the general provisions of ASTM standard D 6913 (ASTM, 2004). Fig. 3.3 presents the initial grain size distribution for the tested soils of the fouled road after recent undercutting. It clearly shows the source of fouling is in fact subgrade intrusion and not particle attrition. However, the level of fouling changed with fluctuations in the water table. Initially, sub-ballast fouling was ~5% and ballast gradation shows ballast fouling around ~2%. Trivial amount of material passing sieve No. 4 (4.76mm or smaller, which is a measure of fouling due to particle attrition) (Li et al., 2015). Based on the Unified soil Classification system, the fouled sub-ballast is classified as Well Graded Gravel (GW) with sand. However, based on AASHTO M 145 system (AASHTO, 2008), the fouled sub-ballast was classified as A-2-4(0). The fouled ballast was classified as Poorly Graded Gravel (GP), and as A-1-a (stone fragments, gravel, and sand) according to USCS and AASHTO, respectively. According to the USCS the subgrade was classified as Silty Sand (SM), and A-2-4(0) based on AASHTO. The properties of the fouled sub-ballast layer are shown in Table 3.1.

Percent passing can be used as a measure of fouling, referred to hereafter as percent fouling (Tennakoon et al., 2012). Percent fouling is the percentage material passing sieve No. 200 (0.075 mm). However, further testing is required to understand the plasticity of fouling material which impacts the ballast performance. The percent fouling is used in this study because the amount of material passing No. 200 sieve provides a better evaluation of the influence of clay-sized fouling material on the ballast behaviour (Bruzek et al., 2016). Furthermore, experimental testing on fine contaminated ballast showed significant increase in ballast

settlement and compressibility, especially when moisture content of clay-sized material within the ballast increased (Han and Selig, 1997). Percent fouling of 35% is proposed as threshold at which immediate maintenance should be applied to prevent track geometry issues (Bruzek et al., 2016).

Track fouling changes with time, especially when the source of fouling is not particle breakage or attrition. As the water table level rises and falls, it drags the fines from the subgrade with it. For instance, during the two site visits made, as part of this study, percent fouling of the ballast ranged from 58% - 67% as shown in Table 3.2. Samples' analysis showed that as the percent fouling decreased, clay activity of fine materials also decreased.



Fig. 3.2 Sioux City BNSF railway network instrumented site at Parkville, MO

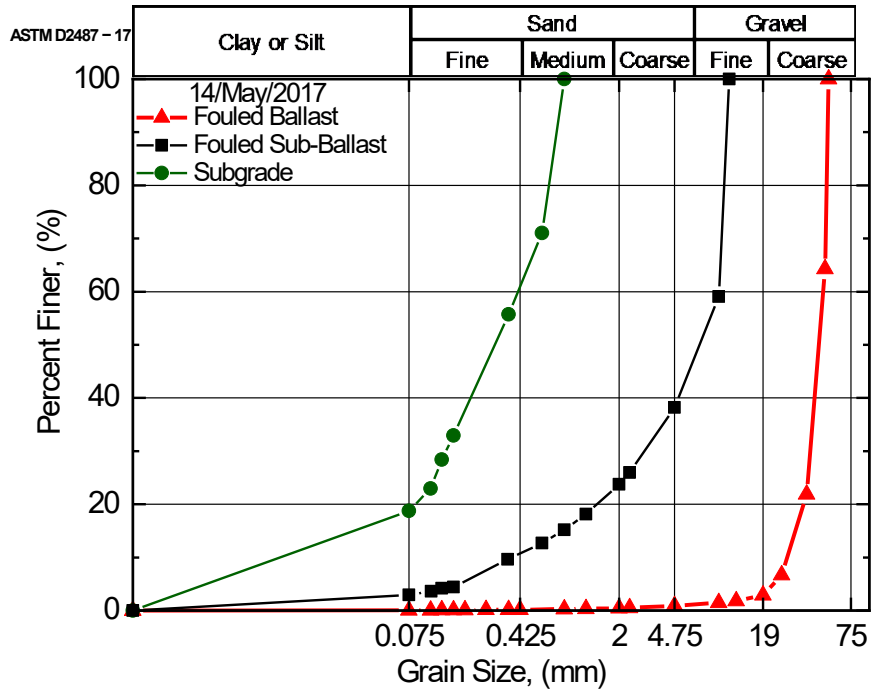


Fig. 3.3 Particle size distributions of fouled ballast, fouled sub-ballast, and subgrade

Table 3.1 Characteristics of the fouled sub-ballast

Sub-Ballast Property	Value
Maximum Dry Density, ρ_d	1.93
Friction Angle, ϕ	40.00°
Plasticity Index, PI	10.00
Specific Gravity, G_s	2.65
Coefficient of Uniformity, C_u	25.10
Coefficient of Curvature, C_c	2.80
D_{10}	0.30 mm
D_{30}	3.10 mm
Mean Diameter, D_{50}	7.40 mm
D_{60}	9.50 mm

Table 3.2 Railroad fouling parameters

Ballast Sample Date	Percent Fouling	FI	W_N	LL	PL	PI	Activity	USCS Symbol
05/Dec/2017	67	68.5	17.8	39	30	9	0.13	CL
06/Apr/2018	58	59.0	9.4	25	20	6	0.09	CL-ML

3.3.2 Instrumentation

3.3.2.1 Rail web strain gauges and high-speed cameras

Longitudinal resistance strain gauges placed at neutral axes of rail web were used to monitor continuously welded rails (CWR)(AEA-Technology-Rail, 2006; Feng et al., 2011; Feng, 2012; Askarinejad et al., 2013; Li, 2013; Askarinejad et al., 2015; Stark et al., 2015; Wang et al., 2015; Stark and Wilk, 2016; Wilk, 2017; Liu et al., 2018). Measurement of rail deflection due to applied wheel loads is widely used due to its reliability, simple equipment configuration and long-term monitoring capability (Wang et al., 2015). The current instrumentation system comprised strain gauges, moisture probes and high-speed cameras as presented in Fig. 3.4a. A typical cross-section of the railroad segment is shown in Fig. 3.4b.

Several studies have used the rail neutral-axis attached strain gauge circuits at the crib to quantify wheel loads (Rabbi et al., 2022; Thompson et al., 2022; Thompson et al., 2022) based on the Differential Shear Strain (DSS) (Ahlbeck et al., 1980). Utilising the concept of DSS, calibrated crib-rail neutral-axis sensors were used to measure vertical wheel loads. The concept is protracted to quantify vertical tie reaction forces with minor changes to the position of the strain gauges with respect to the cross-tie and with the addition of a set of strain gauges to the circuit. As the wheel load is applied between two strain measurement locations, the change in the measured crib strain is directly correlated to the applied wheel load magnitude.

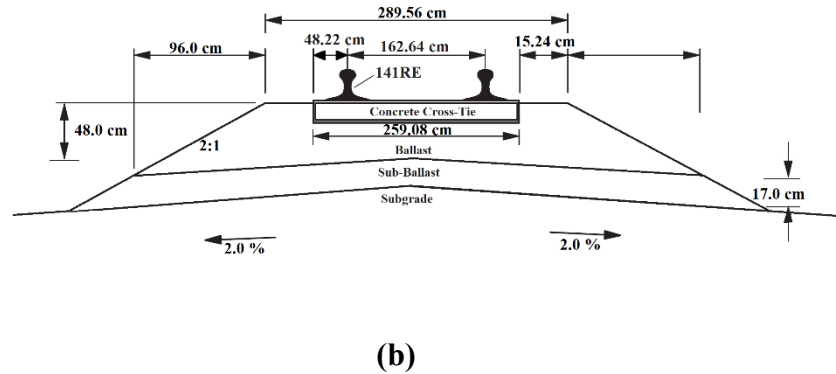
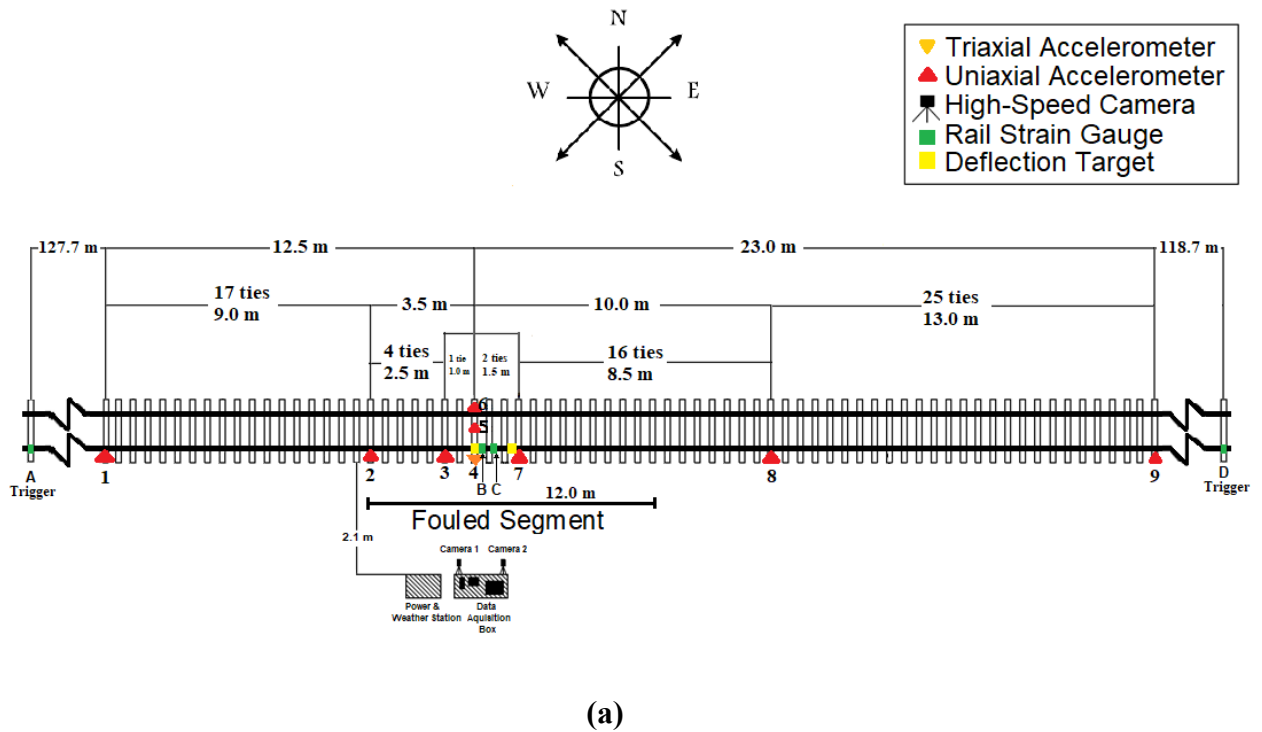
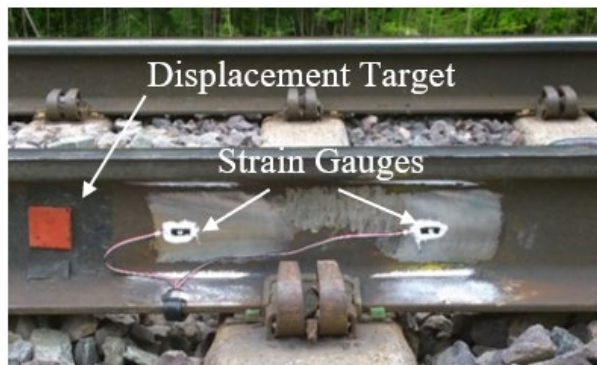


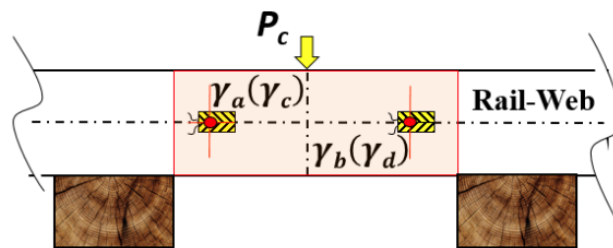
Fig. 3.4 Instrumented railroad: (a) layout plan, (b) cross-section

Four strain gauges were installed at web mid-height along the neutral axis as shown in Fig. 3.5a. They were installed in a full-bridge type I configuration to measure rail bending (National-Instruments, 2020). To ensure adhesion between rail surface and strain sensors, rail surface was sanded to remove oxidized material, and the sensors were glued to the rail web

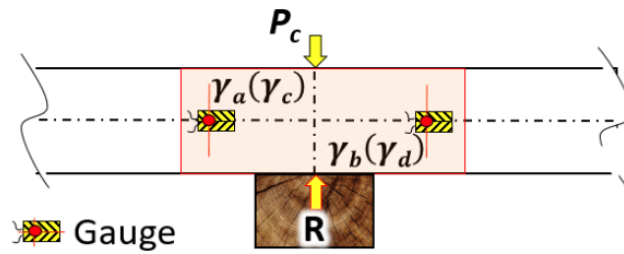
and covered with a sealant for protection from external environmental conditions. During installation, circuits were attached above the crib and above the cross-tie along the neutral axis (N.A.) where, theoretically, tension from the rail head transitions to compression at the bottom of the rail. The strain gauges were located in proximity of the deflection targets to ensure consistent collection of relevant load and deflection data, and they were calibrated using the Delta Frame (setup shown in Fig. 3.5d). Crib and rail-tie sensors measured instant longitudinal rail bending-strain developed rail mid-height under distant and proximate wheel loads as shown in Fig. 3.5e. Voltage difference measured across the sensor is used to estimate wheel load magnitudes, using calibration data. Meanwhile, direction of rail bending (positive/downward or reverse/upward) is captured by the sign of the measured voltage.



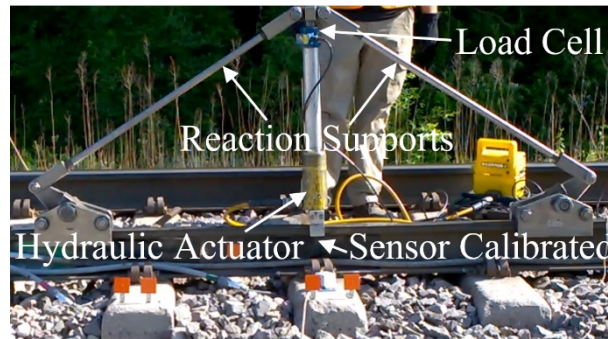
(a)



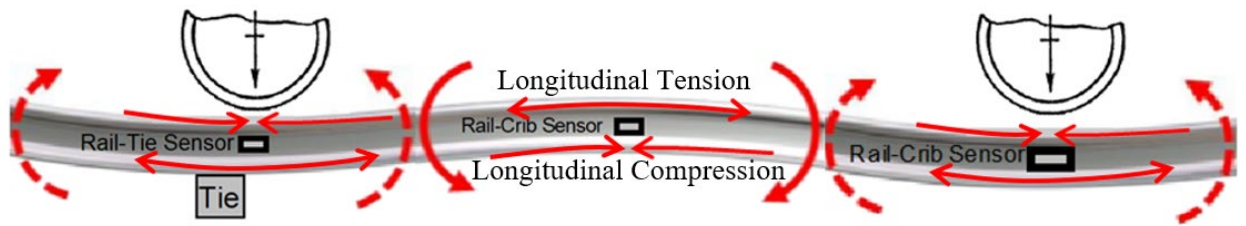
(b) (Thompson et al., 2022)



(c) (Thompson et al., 2022)



(d)



(e)

Fig. 3.5 Field monitoring sensors: (a) rail strain gauges and camera target, (b) Crib circuit, (c) cross-tie circuit (d) strain gauge calibration setup, (e) longitudinal rail bending-strain due to wheel loads

Two Basler acA800-200gc area scan Gigabit Ethernet cameras with high resolution at 240 frames per second, shown in Fig. 3.6, were utilized in the field monitoring program. Both cameras monitored mounted targets on the track and recorded the reoccurring track permanent and transient settlements. Deflection readings obtained from the cameras demonstrated a strong correlation between reoccurring track settlement and cross-tie-ballast gaps. This

instrumentation system facilitated monitoring permanent and transient responses of the railroad system.



Fig. 3.6 Basler high-speed camera

3.3.2.2 Reliable data acquisition system

Data from all sensors were collected using National Instruments (NI) 8 slot data acquisition system (cDAQ-9172) as shown in Fig. 3.7. The instrumentation system was designed to be temperature resistant in order to minimize error due to fluctuations in ambient temperature from seasonal climatic conditions, direct sunlight, and shading from traversing trains. The data acquisition system collected strain readings at a time interval of 2.4×10^{-4} second per measurement.

3.3.2.3 Ballast embedded moisture probes, robust weather station, and sustainable power source

To monitor the environmental conditions, a robust weather station was installed at the site, which comprised an anemometer to measure wind speed, a rain gauge to measure rainfall, moisture probes embedded at different depths in the railroad substructure. Fig. 3.8 shows the weather station powered by two solar panels and a wind turbine. Fig. 3.9 displays the moisture probe installation.



Fig. 3.7 Data acquisition box



Fig. 3.8 Site weather station

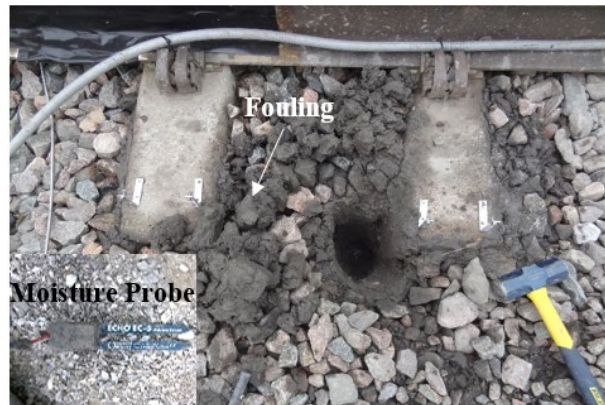


Fig. 3.9 Moisture probe installation

3.4 Local Environmental Conditions

In order to evaluate the effect of local environmental conditions on the fouled ballast bed performance, time histories of measured responses for four selected trains were analyzed as typical results of the measured responses for the winter season. Measured data of the four trains were based on the front locomotives of the rolling stock. The trains travelled through the monitoring section at the following times: 20/Dec/2017-15:15, 31/Dec/2017-14:22, 20/Jan/2018-12:23 and 20/Jan/2018-16:32, hereafter referred to as: Train 1, Train 2, Train 3, and Train 4, respectively.

3.4.1 Temperature Profile

Ambient temperature measurements (Min., Avg., Max.) for the duration of the monitoring period were obtained from the weather station installed at the Parkville, Missouri fouled site. Fig. 3.10 presents the temperature data corresponding to the dates of monitored trains. The corresponding (Min., Avg., Max.) for Trains 1, 2, 3, and 4 were (1.4, 6.9, 12.3) ° C, (-22.7,-18.2,-11.9) ° C and (1.9°, 12.0, 18.5) ° C.

3.4.2 Precipitation/Snowfall effect on Soil Moisture Regime

During freeze-thaw and precipitation cycles (January-February), the soil at different depths experienced significant variation in moisture regime. The change from lowest sub-zero temperatures recorded for the study period (-22.7°C) to the high of 10°C caused a sudden increase in soil moisture content. The high rise in temperature was also associated with rainfall precipitation as shown in Fig. 3.10 and Fig. 3.11.

Fig. 3.10 shows that data obtained from the site weather station, which represent weather conditions railroad system was exposed to during the passage of: Train 1 (positive single digit ambient temperature), Train 2 (sub-zero temperature), and Train 3 and Train 4 (double digit ambient temperature). The measurements demonstrate the high variability in temperature the railroad infrastructure and superstructure were exposed to. Fig. 3.11 presents both precipitation trends and the variation of moisture content in the railroad substructure beneath the concrete cross-tie for the period November 2017-March 2018. Fig. 3.11 shows that the soil moisture content increased significantly after each precipitation event.

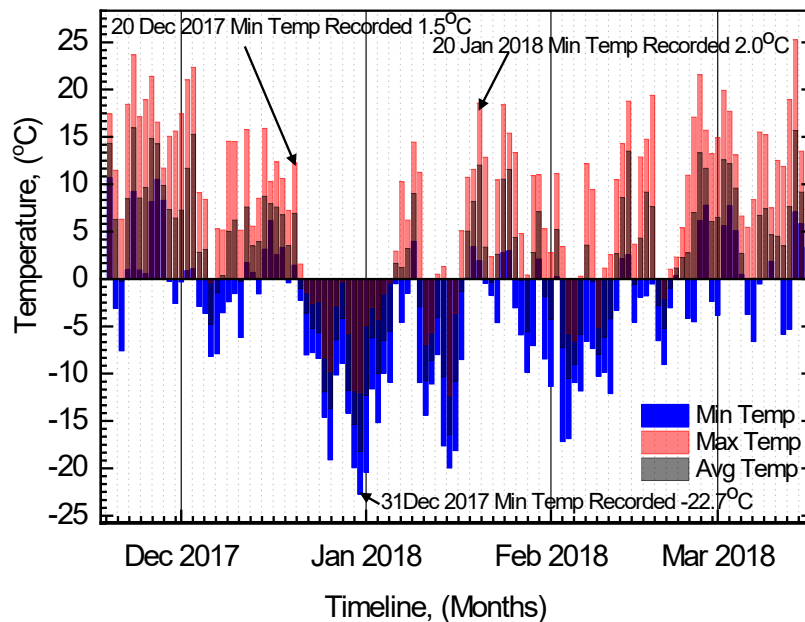


Fig. 3.10 Local temperature profile during study period

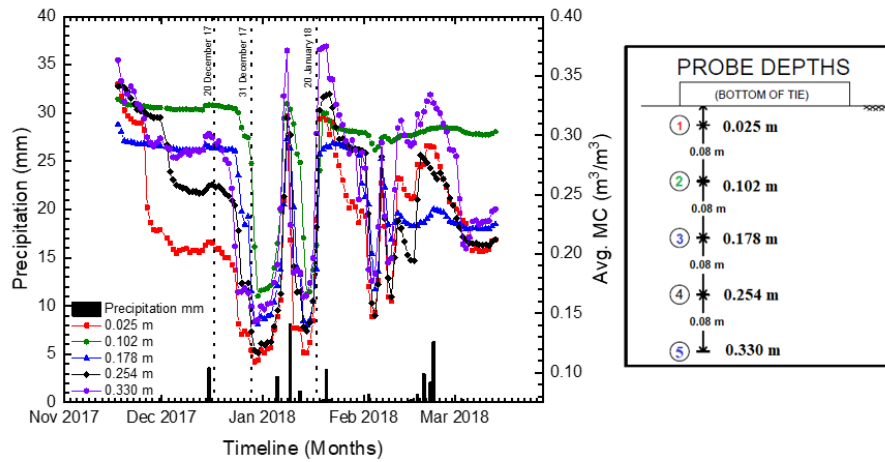


Fig. 3.11 Effect of precipitation on soil moisture content

Ballast depth of the fouled railroad segment was 0.48m and the depth of the sub-ballast was 0.17 m. Table 3.3 summarizes the readings from the moisture probes exactly at the time of passage monitored trains. Moisture probes and rain gauge readings showed that ground water was rising towards the railroad surface and was trapped at a depth of 0.102 m and 0.178 m below the cross-tie bottom (at the depth of probe 2). Data collected from the moisture probes showed that the ballast performed sub-optimally as can be noted in Table 3.3. Clean uncontaminated ballast would drain water towards the railroad shoulder regardless of the permeating water source, or direction of water flow. Generally, Table 3.3 shows that the maximum moisture content in the fouled ballast was at a depth of 0.330 m below cross-tie, which indicates the source of water was phreatic. This observation is validated by data obtained from the rain gauge, wherein 0.0 mm of rain was recorded. Moisture content gradually continued to rise from the bottom to the top. Intrusion of the sub-ballast and silty clay subgrade into the ballast was evident at depth 0.330 m below the instrumented cross-tie. Measured MC at depths of 0.102 m and 0.178 m below cross-tie were high compared to the values at depths above and below them owing to accumulation of groundwater due to hindered drainage.

Table 3.3 Railroad condition for selected trains crossing fouled railroad segment

Train #	Temperature (°C)	Moisture Probe Depth from top of Ballast					Comments
		0.025 m	0.102 m	0.178 m	0.254 m	0.330	
							Moisture Content (Duong et al.)
Train 1	4.7	20.4	32.6	28.9	25.7	29.5	High MC ballast; last precipitation 3.556 mm on 16/Dec/17
Train 2	-12.6	12.0	27.2	16.0	13.3	15.9	Low MC ballast
Train 3	10.4	20.5	20.8	18.0	19.0	36.4	Moderate MC; last precipitation event (1.02 mm) was on 13/Jan/18
Train 4	12.0	29.0	21.2	18.6	20.7	36.6	

Tamping processes to restore railroad surface and cross-tie level are not sufficient to resolve the problem of poor drainage because the tamping tines penetrate the ballast to a depth of 0.020 m below the cross-tie (Grossniklaus, 2016). This explains the relatively better drainage around moisture probe 1 (0.025 m beneath the cross-tie). However, at identified critical depths (0.102 m and 0.178 m), there would be minimal effect of vibrations induced by tamping tines.

Data presented in Fig. 3.12 was calculated by averaging moisture probe readings at different embedment depths corresponding to the average static track stiffness at the time of train passage. Average static track stiffness was estimated by averaging the load vs deflection data for the monitored 32 trains. Fig. 3.12 presents the variation of ground moisture with static track stiffness for the test trains. For soft track, (i.e. 7-15 MN/m) moisture values were higher compared to typical railroad moisture values ($\sim 0.20 \text{ m}^3/\text{m}^3$). Measured MC values at two depths (0.102 m and 0.178 m below cross-tie) were higher than the rest of fouled ballast as the

stiffness increased, which indicate that the moisture was trapped, and ballast was near saturation. Fig. 3.12 showed that moisture was mainly supplied from a depth of 0.330 m below the bottom of cross-tie, where the ballast interacts with sub-ballast and native soil. Sub-ballast at 0.330 m failed to drain the rising water because of contamination with silty-clay fines; instead, it retained water and transported it upwards by means of capillary action. Additionally, the high water-storage capacity of soil at depth 0.102 m suggests that ballast was contaminated with clay-rich fines, which could retain water (O'Geen, 2013). Hence, the fouled ballast at depth 0.102 m acted as a source of perched water providing it to the layers above and below. At the bottom of the cross-tie (0.025 m) and at a depth of 0.254 m, the water-storage capacity decreased for typical and rigid static track stiffness (i.e. $k \geq 25$ MN/m). This indicates soil from depth 0.102 m to depth of 0.178 m below the bottom of the cross-tie was highly fouled.

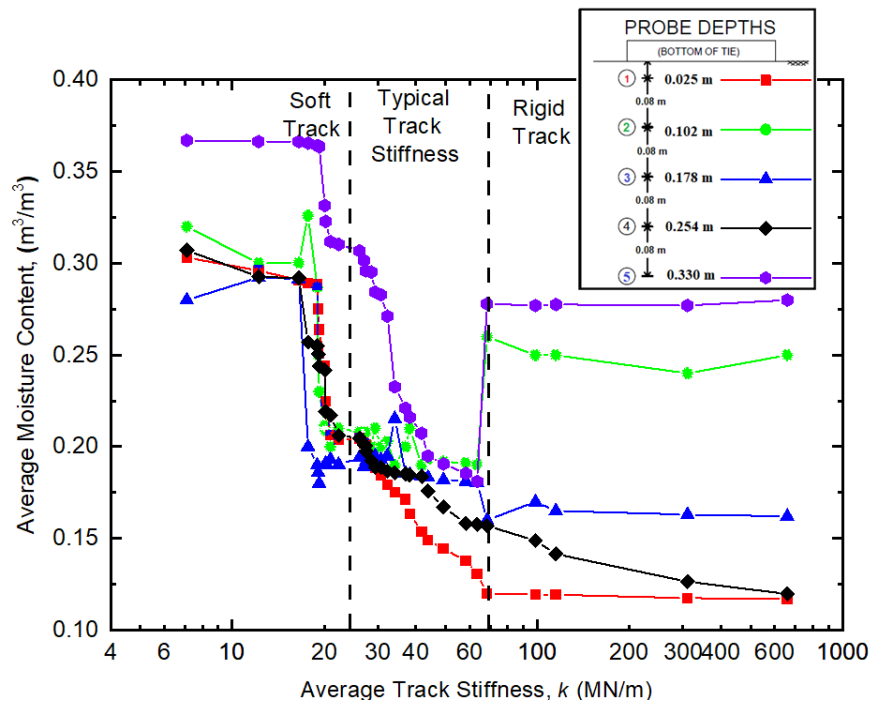


Fig. 3.12 Variation of ground moisture with static track stiffness

3.5 Fouled Track Superstructure System Response

The railroad response was monitored and recorded during trains passage. Recorded response quantified the deformational behaviour at two locations of the CWR of fouled railroad superstructure due to heavy haul trains travelling in adverse environmental conditions. Train speed was restricted throughout the entire fouled segment according to the ballast compliance waiver program. Therefore, the effect of train speed on the response of the fouled railroad is considered insignificant. Results obtained from the monitoring program and their analysis are provided for the four selected Trains 1, 2, 3, and 4.

3.5.1 Wheel load Characterization

Readings of calibrated strain gauges were used to determine the vertical wheel-rail contact loads, i.e. the wheel-rail force above the cross-tie (P), and the wheel-rail force above the crib (P_o). The efficiency of voided cross-tie support is investigated by evaluating the measurements of two strain gauges installed on the rail web, i.e. voided tie-rail SG. Wheel-rail force above the cross-tie (P) was estimated from measured instant longitudinal rail bending-strain developed under the wheel load above the voided cross-tie. Crib wheel-rail force (P_o) was determined by measuring instant longitudinal rail bending-strain generated under the wheel loads above the crib. For well-supported cross-ties, the rail loads above cross-tie (P) would be significantly less than rail loads above the crib because rail section above the crib deflects more than rail section above the cross-tie due to its support.

Strain measurements of rail sections above the crib and cross-tie are used to quantify wheel loads and to analyze the response of rail section above the voided cross-tie as shown in Fig. 3.13. When the train's engine forward wheel is directly above the rail sensor, the applied vertical load causes longitudinal bending stresses, compressive stresses at the rail head, and tensile stress at the foot of the rail. Stresses generated in the rail are mainly due to the rail bending, which is supported by elastic foundation system and cross-ties resting on ballast and sub-ballast (Johns et al., 1981). When the locomotive's foremost wheel approaches a particular point on the rail head, the vertical load causes longitudinal bending stresses. Nominal static

vertical wheel loads are a function of the railcar type (i.e. locomotives, freight cars or passenger coaches) and its weight. Vertical wheel loads due to freight cars vary significantly within the same rolling stock due to weight of the cargo onboard (loaded, unloaded). Meanwhile, the magnitude of nominal vertical loads from locomotives have the least variance (Edwards et al., 2017). Therefore, to minimize the effect of load variance and to establish a uniform base for comparison, the current analysis is focused on forward bogie of lead locomotive.

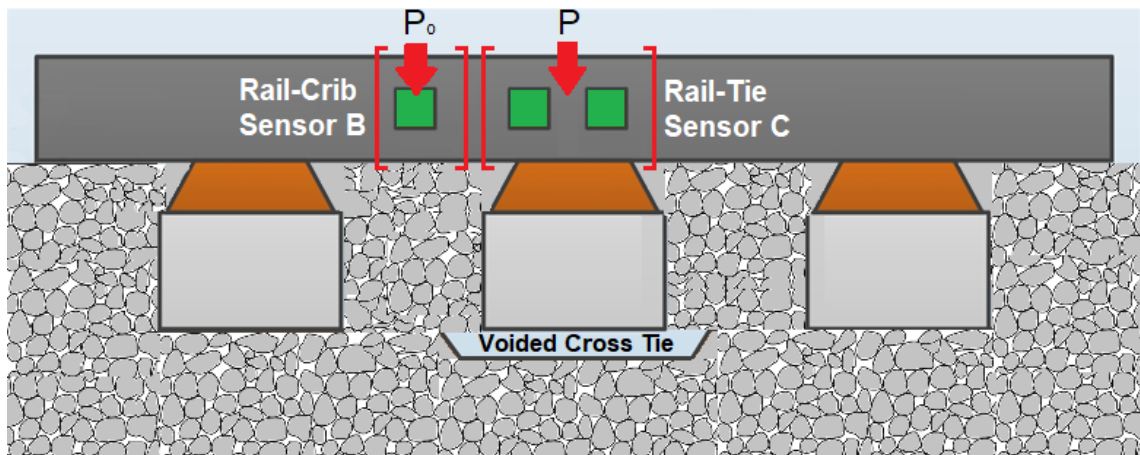


Fig. 3.13 Illustration of crib-rail and rail-tie loads

3.5.2 Estimating Cross-Tie Reaction

Measurements from strain gauges located at the rail section above the crib area (space between the cross-ties) were used to estimate wheel load (P_o) and those from strain gauges located above the cross-tie were used to estimate the loads distributed to the cross-tie (P). Cross-tie reaction was estimated by deducting wheel load magnitudes obtained from the strain gage located above the crib (P_o) from wheel loads obtained from strain gauge above the cross-tie (P), i.e. (Chang et al., 1980; AREMA, 2013; Stark et al., 2015; Stark and Wilk, 2016; Wilk, 2017):

$$Tie\ Reaction = P_o - P \dots \dots \dots Equation\ 3.1$$

Where,

P_o = peak measured wheel load above the crib

P = peak measured wheel load above the cross-tie

Rail-tie loads for good tie-ballast contact typically range from 30 % to 50% of wheel load (Frohling, 2009). A good tie-ballast contact facilitates transferring most of the wheel load on the rail directly to the ballast. Hence, the longitudinal bending strain at the rail above cross-tie would be minimal. On the other hand, unsupported cross-ties would deflect same as the rail section above the crib area, and the strain above the cross-tie would be close to the strain above the crib. Thus, the difference in wheel-rail load magnitude would be approximately zero. The tie load ratio may be used to quantify the degree of cross-tie support (Chang et al., 1980; AREMA, 2013; Stark et al., 2015; Stark and Wilk, 2016; Wilk, 2017), i.e.:

$$Tie\ Load\ Ratio = \frac{P_o - P}{P_o} \times 100 \dots \dots \dots Equation\ 3.2$$

The tie load ratio is approximately 40% for the good tie-ballast contact, and less than 30% for poor cross-tie support (AREMA, 2013; Wilk, 2017). Furthermore, a good tie-ballast contact would result in high confinement of the cross-tie, increasing its efficacy in resisting uplift forces that might occur at the connected rail section. These uplift forces arise due to the reverse bending of CWR. Fouled railroads with poor confinement, (i.e. low relative density, D_r), would resist lower uplift forces and would engage a fewer cross-ties pre-loading and post-loading (i.e. prior to bogie arrival and after its passage). The uplift forces due to reverse bending can be given by:

$$UR_{approach} = \frac{P_u\ approach}{P_o\ max} \dots \dots \dots Equation\ 3.3a$$

$$UR_{departure} = \frac{P_u\ departure}{P_o\ max} \dots \dots \dots Equation\ 3.3b$$

Where,

UR = uplift ratio in -kN/kN

P_u = peak uplift force experienced by the rail above the cross-tie

Equations 3.3a and *3.3b* were developed on the basis of *Equation 3.2* and observations from monitoring the fouled railroad behaviour.

The highest measured tensile force (P_u) in rail-tie section was developed when two bogie axles were surrounding the instrumented cross-tie (i.e. when two axels confined the cross-tie from both sides). The maximum uplift force for the approach of first wheel and departure of last wheel of front bogie was developed at the rail-tie instrumented section when the centreline of the wheel was at a distance of $0.1S$ (i.e. in the rail- crib area). In general, when the cross-tie was between the front and middle axles or the middle and rear axles, the applied wheel loads created bending moments from both sides of the cross-tie.

The total cross-tie uplift forces depend on several factors, including wheel loads, support provided by concerned cross-tie and adjacent cross-ties, number of cross-ties engaged by distant wheel load, distance between wheel location and point of measurement, and weight of cross-tie. Nonetheless, to quantify the cross-tie uplift forces upon approach, *Equation 3.3a* correlates rail-tie uplift force to maximum crib load of approaching wheel. Similarly, *Equation 3.3b* relates rail-tie uplift forces, upon departure, with maximum crib load of departing wheel. In *Equation 3.3a* and *Equation 3.3b*, tensile rail-tie forces are normalized by actual wheel load to estimate the effect of one unit (1.0 kN) of applied wheel load on the response of rail-tie section, i.e. tensile forces generated due to track uplift (reverse bending), per 1.0 kN of wheel load. As the cross-tie uplift forces generated at neutral axis increase due to track uplift, reverse bending of rail-tie section increases, and the performance of the superstructure deteriorates.

3.5.3 Rail Bending Forces at the Neutral Axis

The current practice is to estimate the behavior of wheel rail contact forces based on quasi-static calculations, ignoring dynamic effects of moving trains (Hamarat et al., 2019). However, actual train wheel load is cyclic as displayed in Fig. 3.14, which exhibits the time history of CWR wheel-rail contact forces due to Train 1. The time history is truncated to present only the first 0.7 second to highlight the rail response to the passage of front bogie of lead locomotive. This load was cyclic as demonstrated by the instantaneous bending stresses. The passing

vehicles induced vertical, lateral, and longitudinal wheel forces in addition to the reaction support provided by the cross-ties and ballast.

The passing vehicles subject the CWR to cycles of positive bending moment (M^+) and negative bending moment (M^-) (Fallah Nafari et al., 2018). Measured loads shown in Fig. 3.14 are in agreement with Fallah Nafari et al. (2018) findings based on the Winkler Model, which simulates the rail as an infinite beam on a continuous elastic foundation. Measured wheel loads are influenced by rail bending, i.e. the rail bending is directly correlated with measured load magnitude. This is clearly shown in Fig. 3.14, where the rail-tie sensor measured lower wheel magnitude in comparison with the rail-crib sensor. Well-supported cross-ties restrict the rail from deflecting, while voided cross-ties causes the rail-tie section to excessively deflect. Positive bending moments (M^+) occur directly beneath train wheels, while the negative bending moments occur away from the wheel, and between freight cars. The positive bending moment occurs with the rail deflection downwards, while the negative bending moment (M^-) occurs with reverse deflection.

Fig. 3.14 displays two typical wheel-rail contact loading patterns, and inserts showing the number of engaged ties as the wheel approached the instrumented cross-tie. Crib rail sections exhibited a consistent loading pattern (P_o), i.e. repeated loading of 150 kN dynamic contact load. On the other hand, the rail sensor aligned with cross-tie edge recorded a repeated loading (P) characterized with load reversal. Rail head experienced a three-stage stress reversal cycle under the action of one wheel. However, unlike rail head, the neutral axis experiences a one-stage stress reversal cycle under the action of one wheel. Load reversals occurred at the neutral axis only when wheel was exactly above the rail instrumented section. Stress along the rail neural axis above the cross-tie changed as wheel traversed. As the wheel approached, the stress at neutral axis was tensile due to track uplift. When the wheel was directly above the sensor, the stress reversed and became compressive. This means that the neutral axis of rail at the cross-tie would have undergone one stress reversal cycle (tension-compression-tension) under the action of one wheel.

Load reversal prevailed at the rail-tie sensor, with positive load indicating longitudinal compression initiated from the top of rail (head) to the neutral axis and negative load indicating longitudinal compression initiated from the bottom of rail (flange) to the neutral axis of rail web. In addition, the sign indicates the rail bending direction; vertical wheel compressive forces above the neutral axis (positive sign) cause downwards deflection of the rail section while tensile stresses above the neutral axis (negative sign) indicate that the rail is bending upwards, and the cross-tie is being pulled out.

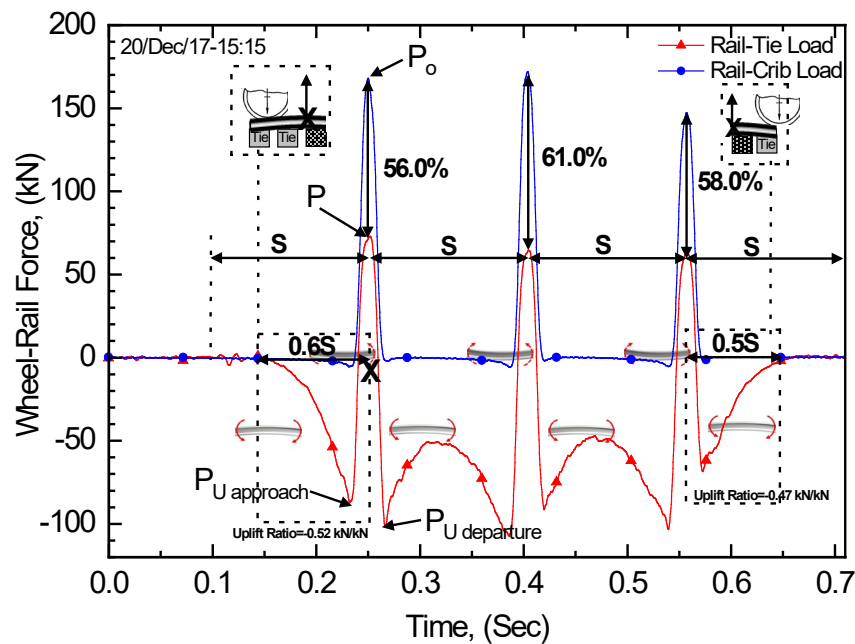


Fig. 3.14 Time history of the measured wheel-rail force for Train 1 obtained from rail-crib sensor B and rail-tie sensor C located in the fouled segment

The longitudinal range of influence of distant wheel loads can be established by correlating the range of influence with the distance of wheel load peaks (wavelength, “S”) as shown in Fig. 3.14. It can be noted from Fig. 3.14 that when the wheel was at distance $0.8S = 1.28\text{m}$ (S =bogie axle spacing =1.6 m for BNSF freight locomotives) away from the location of rail strain gauge, deflection initiated due to the distant wheel load of the train’s engine. Meanwhile, the rail crib section did not experience any bending stresses. This is mainly because the crib section, unlike

the rail-tie section, does not offer any support (only bends downwards). The difference between the forces experienced at the rail neutral axis ($P_o - P$) can be considered a measure of the ballast efficiency (static track stiffness) supporting the monoblock cross-tie against downwards forces.

Fig. 3.14 displays wheel-rail contact forces for Train 1. Time history is truncated to the first 0.7 second to focus on the rail response to the passage of the front bogie of lead locomotive. Force time history presented in Fig. 3.14 demonstrates that as the train traveled through the fouled segment and the front wheel reached at a distance of 0.6S, the rail head flexural stresses became tensile, and the rail curved upwards. For the fouled ballast bed test conditions, as the bogie arrived within the linear range of influence for the instrumented segment (0.6S from the first axle of the bogie); the rail at the crib and at cross-tie deflected upward as demonstrated by the tensile stresses at the neutral axis.

Fig. 3.14 demonstrates the effects of unfavorable environmental conditions on rail response. The moisture content of substructure (ballast and sub-ballast) was relatively high as shown in Table 3.3, associated with the positive ambient temperature (4.7°C), and consequently, cross-ties support to distant loads was limited. When the lead locomotive approached the voided cross-tie (at a distance of 0.6S), both rail-crib and rail-tie bent upwards. Meanwhile, the cross-tie beneath the instrumented rail section did not provide any support to rail bending at 1.0S from the strain gauge. Results show a 40% decrease in the longitudinal range of influence compared to the case of trains operating in favorable environmental conditions. This is explained in part by the support provided by the array of cross-ties spanning a distance of 0.6S that were in partial contact with the fouled ballast bed. This also indicates that poorly supported cross-ties are seated on a weak layer of slurry with low subgrade modulus and low confinement. Upon departure of Train 1 triple axle bogie, the voided cross-tie provided no resistance at distances further than 0.5S from the rear wheel, a 61.5 % decrease in the longitudinal range of influence, which reduced the number of cross-ties supporting CWR. The decrease in cross-tie confinement is thus attributed to increased tensile stresses associated with rail bending upward, and consequently, uplifting of the adjacent cross-tie. The longitudinal range of influence post cyclic loading was shorter compared to the preloading of the

instrumented segment indicating that the fouled railroad deteriorated due to the cyclic loading resulting in a fewer number of cross-ties engaged. This is attributed mainly to the high moisture content trapped by the fines contaminating the ballast.

For flexible track, the cross-ties resist upward bending by maintaining contact with the unfouled ballast. The rear wheel of front bogie applied $P_o = 150.0$ kN on the crib, while the rail-tie sensor measured $P = -70.0$ kN, indicating that the cross-tie system could only resist 58% of the applied tensile force. Thus, the cross-tie uplifted from the ballast creating a void beneath it. The decrease in cross-tie resistance may be attributed to its low confinement. In addition, the positive average ambient temperature (4.7°C) recorded on 20/Dec/17 resulted in increased MC in the fouled ballast, and the corresponding increase in pore water pressure decreased the soil effective stresses.

Tie load ratio ranged from 56.0 % to 61.0% of the actual applied wheel-rail force at the crib. The larger difference between P_o and P indicates higher substructure efficiency in reducing the superstructure deformation. The substructure was even more efficient in resisting wheel loads from the middle and rear axles (61.0% of wheel load) because the front and rear axles were at a distance of $1.0S$ away from the sensor on both sides, which increased the cross-tie. In addition, cross-tie uplift resistance improved slightly due to the increased confinement after the passage of front bogie. After the rear wheel departure, the support against CWR upward deflection increased slightly. The uplift ratio was -0.52 kN/kN and changed after cyclic loading to -0.47 kN/kN. Nevertheless, the overall system response was poor compared to the response to Train 2 crossing due to increased MC, which was manifested in increased tensile stresses of rail-tie section along a zone of $1.5S$ from rear wheel. When the rear wheel of front bogie departed the instrumented voided cross-tie, the post cyclic loading range of influence decreased to $0.5S$, i.e. fewer cross-ties were engaged post-loading compared to pre-cyclic loading. The fouled railroad track deteriorated and the CWR displacement increased.

Fig. 3.15 displays wheel-rail contact forces for Train 2. Wheel vertical loads at the instrumented rail-cross-tie section decreased because the cross-tie supported the applied load directly, hence limited the CWR bending. Tie load ratio ranged from 45% to 56% of the applied

wheel-rail force at the crib. The middle and rear bogie axles caused lower bending forces at the neutral axis when compared to front axle, although all three axles were loaded equally. Moreover, measured strain at the rail-tie strain gauge indicated wheel-rail bending force induced by the middle axle equivalent to the rear axle. Considering that the front and rear axles were in close proximity of the instrumented voided cross-tie, it would be expected that the front and rear axles contribute to the additional forces applied at the voided cross-tie. However, that was not the case due to the favorable weather conditions as ambient temperature was below zero (-12.6°C). Moisture trapped within the fine contaminated ballast and sub-ballast layers was frozen and the porewater pressure did not arise due to the cyclic loading. On the other hand, when the first axle of front bogie passed over the voided cross-tie, the cross-tie vibrations due to the traveling train compacted the railroad substructure. This compaction increased the effective stresses of railroad substructure and reduced bending stresses caused by the bogie middle and rear axles compared to the front axle. Furthermore, the compaction of soil surrounding the cross-tie reduced the rail deflection due to the mid-axle load to almost the same level as the rear axle.

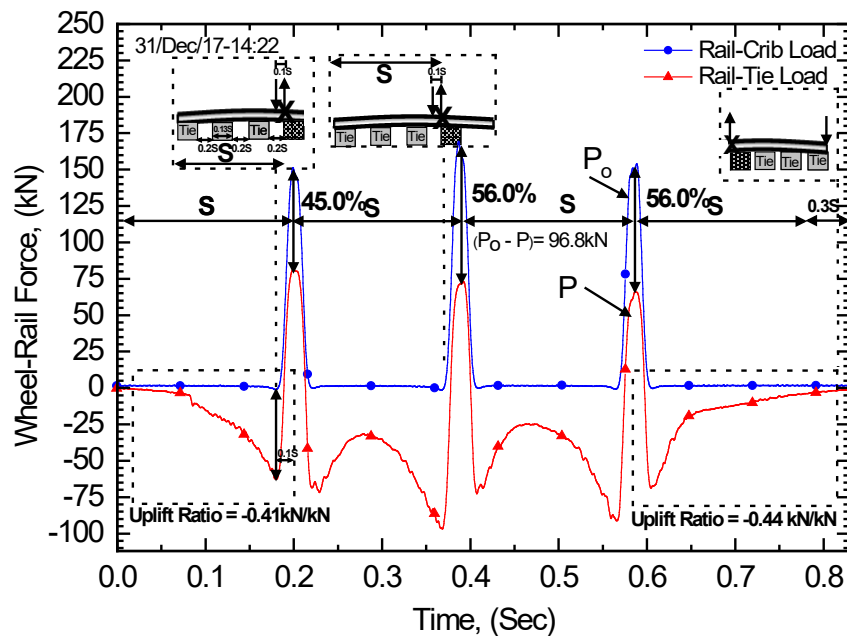


Fig. 3.15 Time history of measured wheel-rail force for Train 2 obtained from rail-crib sensor B and rail-tie sensor C located in the fouled segment

Fig. 3.15 also demonstrates that when the front wheel was at 1.0S from the strain gauge, the rail head flexural stresses became tensile, and the rail curved upwards. This observation is immensely important as tensile stress at the N.A. implies that the cross-tie was subject to uplift forces due to the upward deflection of the CWR. The high rigidity CWR resists the upward deflection due to the support of cross-ties array. Therefore, cross-ties are designed to maintain gauge, longitudinal alignment, and cross-level of the CWR by preventing excessive vertical deflection of the CWR in both directions (upwards and downwards).

Analysis of the uplift forces will be explored further by focussing on the approach of front wheel and departure of rear wheel of the lead locomotive bogie to avoid the effect of superimposed loading from multiple axles. Cross-tie uplift force increased marginally after the loading event (-0.03 kN per 1 kN of wheel load), which means the densification of the ballast during cyclic loading did not improve the rail-tie section uplift resistance. This is because the frozen railroad substructure prevented the ballast particles to reorient and densify to resist cross-tie pull-out. Nonetheless, the system response was still satisfactory. As the front bogie passed, the instrumented rail section experienced tensile forces along a zone of 1.3S from the rear wheel. When the rear wheel departed the instrumented voided cross-tie, the range of influence was 1.3S, i.e. more cross-ties were engaged in post-loading compared to pre-loading. The cross-ties were affected by the train dynamic load and vibrations; consequently, the static track stiffness changed as the substructure particles re-arranged improving contact of cross-ties with the ballast.

Fig. 3.16 and Fig. 3.17 present time histories of wheel-rail contact forces measured during passing of Train 3 and Train 4, respectively. The tie load ratio during the passage of Train 3 ranged from 45.0 % to 56.0 %, while it ranged from 41.0 % to 47.0 % for Train 4. In general, the tie load ratio was insensitive to the overall deflection behavior of the CWR. However, the longitudinal range of influence and the uplift ratio was influenced by the CWR response behavior. Fig. 3.16 shows that fouled ballast uplift ratio changed by 23.8 % (from - 0.42 kN/kN to - 0.32 kN/kN) after the passage of the Train 3 front bogie. On the other hand, the uplift ratio of the rail-tie section changed by 10 % (from -0.40 kN/kN to -0.44 kN/kN) after the passage

of the Train 4 front bogie, i.e. the fouled ballast bed performance was better during the passage of Train 3. Hence, the uplift ratio was well correlated with the deflection of the superstructure.

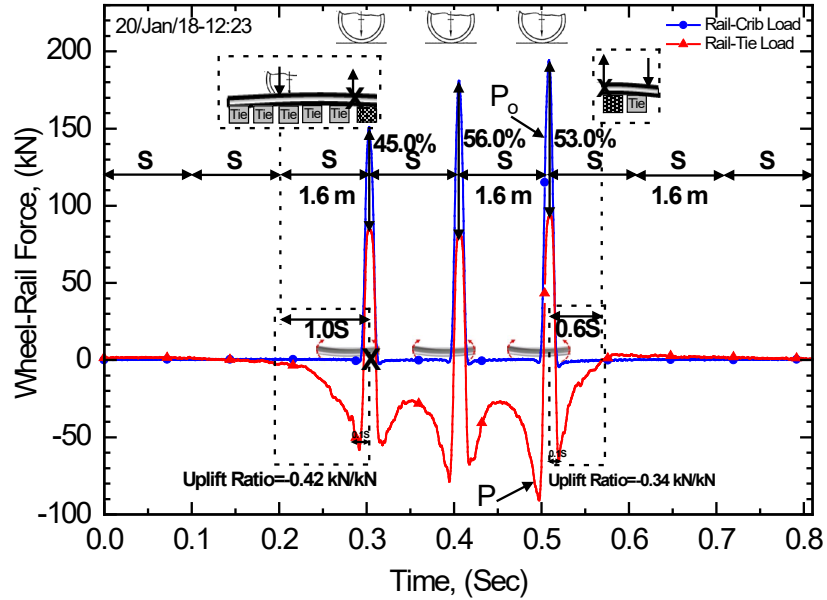


Fig. 3.16 Time history of measured wheel-rail force for Train 3 obtained from rail-crib sensor B and rail-tie sensor C located in the fouled segment

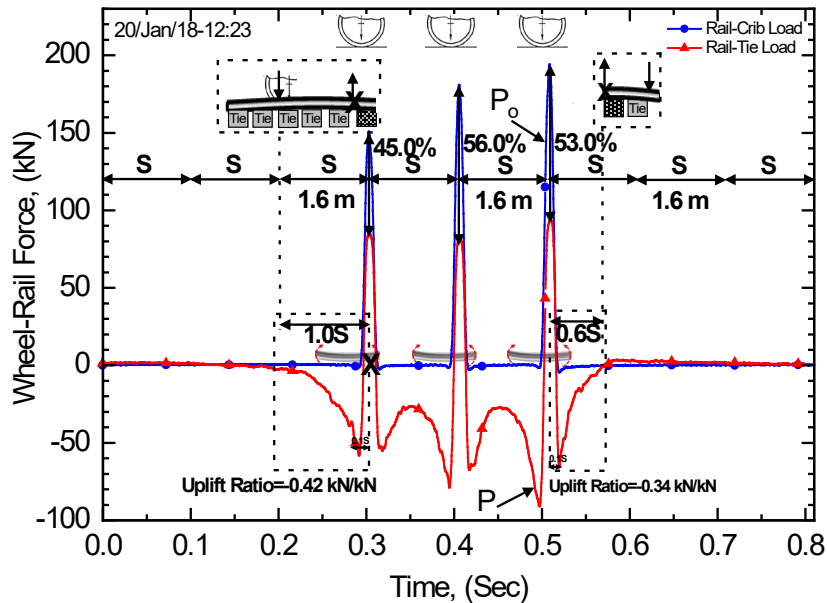


Fig. 3.17 Time history of measured wheel-rail Force for Train 4 obtained from rail-crib sensor B and rail-tie sensor C located in the fouled segment

These observations indicate that employing the tie load ratio as a proxy for cross-tie support efficiency does not capture the superstructure response in fouled railroad environment. However, monitoring the pre-loading and post-loading longitudinal range of influence may capture subtle changes in the response. For instance, post loading longitudinal range of influence of the front bogie rear wheel for Train 3 was 0.6S, while it was 1.0S for Train 4, i.e. number of ties engaged by distant load after bogie departure increased by 66.7% as shown in Figs. 3.16 and 3.17. Post loading longitudinal range of influence for distant wheel loads was in agreement with the measured rail transient displacement because it accounted for the factors that affected the superstructure behaviour. Table 3.4 lists the longitudinal range of influence, which demonstrates the effect of fouled ballast bed support conditions on the CWR performance for Trains 1 - 4.

Table 3.4 Effect of fouled ballast bed support conditions on longitudinal range of influence of distant wheels on the CWR

Train #	Environmental Conditions			Longitudinal Range of Influence (S*)	
	Temp.	MC at Critical Depths		Lead Bogie Approach	Lead Bogie Departure
		°C	(Duong et al.)	(Duong et al.)	Rail-Tie (P)
Train 1	4.7	32.6	28.9	0.6S	0.5S
Train 2	-12.6	27.2	16.0	1.0S	1.3S
Train 3	10.4	20.8	18.0	2.0S	0.6S
Train 4	12.0	21.2	18.6	1.0S	1.0S

* Bogie Axle Spacing; where, S=1.6 m for BNSF freight locomotives studied

Fig. 3.18 presents typical deflection data measured using the highspeed cameras. Results show that rail displacement due to passage of Train 1 was 1.5 times higher than that due to Train 4 and was 5 times that due to Train 2. The excessive rail deflection was caused by poor drainage condition below bottom of cross-tie. Gerald and Richard (1987) reported similar results based

on a laboratory study that evaluated the rail-ballast system performance due to ballast saturation.

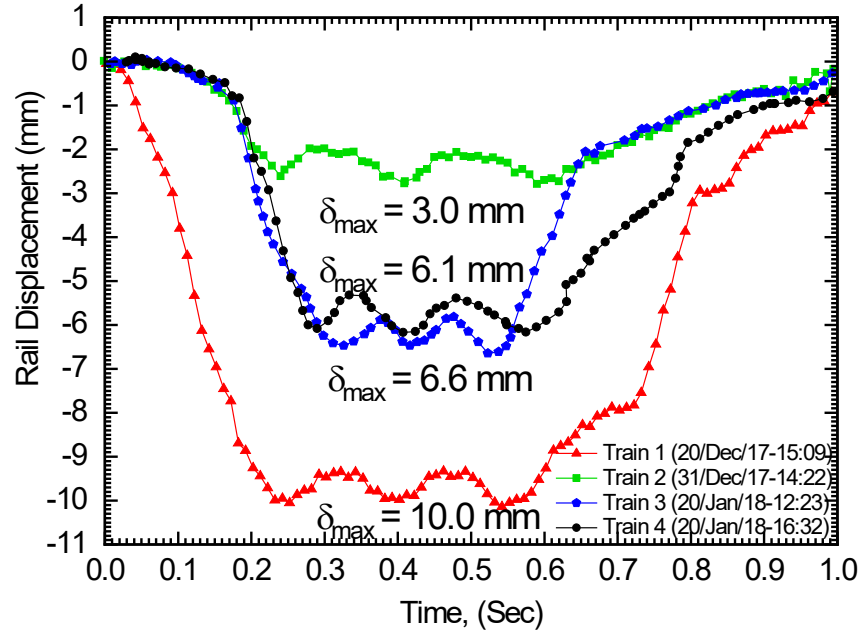


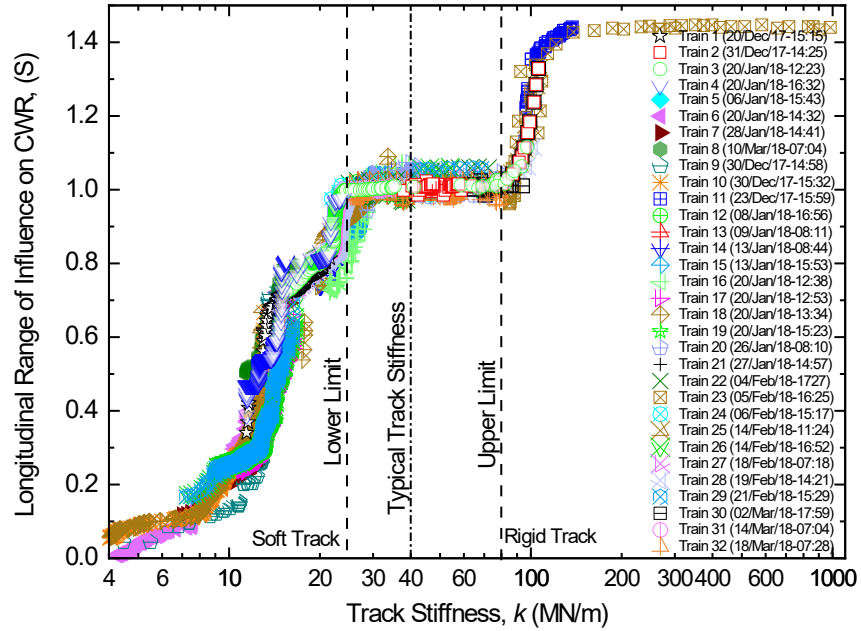
Fig. 3.18 Rail deflection in fouled segment due to cyclic loading of locomotive front bogie

Increase in ambient temperature from sub-zero to above zero caused frozen soil to thaw and MC to increase. The cross-tie load ratio for Train 4 was 6.0 % less than that for Train 3, but the superstructure response was slightly better; the maximum displacements of Train 3 and Train 4 were 6.6 mm and 6.1 mm, respectively. Thus, the tie load ratio could provide an insight into the support condition close to the instrumented cross-tie but would not reflect minor changes in the superstructure performance.

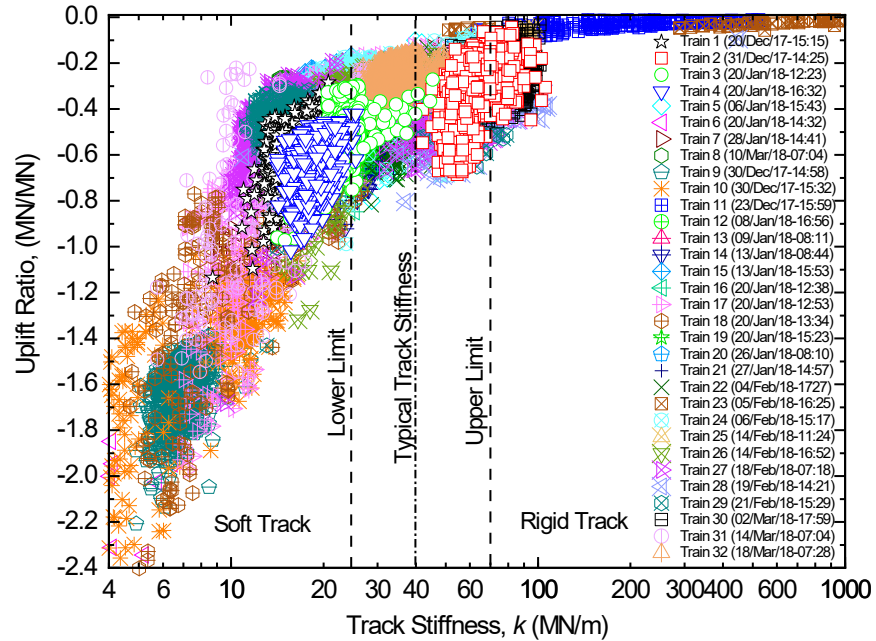
3.5.4 Effect of Fouled Static Track Stiffness on Longitudinal Range of Influence of Distant Wheel Loads

Fouled ballast bed support condition can be assessed by evaluating the range of influence of longitudinal forces acting on the CWR neutral axis. To ensure repeatability of obtained measurements and reliability interpreted results, a total of 32 train passes have been analysed, including response due rolling stock cars and their corresponding rail deflection data. For

increased as the fouled static track stiffness increased; however, uplift ratio varied with fouled static track stiffness above the lower limit.



(a)



(b)

Fig. 3.19 Variation in fouled static track stiffness (k) for the monitored trains passing over rail-crib sensor B and rail-tie sensor C located in the fouled segment for: (a) longitudinal range of influence of distant wheels, (b) rail-tie uplift ratio

3.5.5 Statistical Analysis and Empirical Solution

3.5.5.1 Hypothesis testing

To investigate the association between fouled static track stiffness (k) and longitudinal range of influence of distant wheels (S), the two-sided null *hypothesis 3.1* and alternative *hypotheses 3.2* were formulated. Similarly, to investigate the association between cross-tie uplift ratio and stiffness (k) of fouled track, the two-sided null *hypothesis 3.3* and alternative *hypothesis 3.4* were formulated.

H₀: There is no statistically significant association between longitudinal range of influence of distant wheels on CWR (S) and fouled static track stiffness (k)**Hypothesis 3.1**

H_a: There is statistically significant association between the longitudinal range of influence of distant wheels on the CWR (S) fouled static track stiffness (k).....**Hypothesis 3.2**

H₀: There is no statistically significant association between cross-tie uplift ratio and fouled static track stiffness (k).....**Hypothesis 3.3**

H_a: There is statistically significant association between cross-tie uplift ratio and fouled static track stiffness (k).....**Hypothesis 3.4**

The non-parametric Pearson chi-square test of independence is employed to measure the significance of association. The chi-square statistic is calculated from observed and expected counts under the null hypothesis of independence as given by (Mehta and Patel, 2011):

$$X^2 = \sum_{i=1}^r \sum_{j=1}^c \frac{(x_{ij} - \hat{x}_{ij})^2}{\hat{x}_{ij}} \dots\dots\dots \text{Equation 3.5}$$

Where,

x_{ij} = observed count

$$\hat{x}_{ij} = \frac{(m_i n_j)}{N}$$

i, j = expected count in cell of an $r \times c$ contingency table

m, n = row and column margins, respectively

N = total sample size

The observed asymptotic p-value of the Chi-Square statistic is $0.001 < 0.05$, implying that it is reasonable to assume that cross-tie uplift ratio is dependent on fouled static track stiffness (k). The test was conducted at the 0.05 significance level. Because the observed significance of 0.001 is less than 0.05; hence, the null *hypothesis 3.1* can be rejected, and alternative *hypothesis 3.2* can be accepted. Additionally, the observed asymptotic p-value of the Chi-Square statistic, at significance level of 0.05, is $0.023 < 0.05$, implying that it is reasonable to assume that the uplift ratio is dependent on the fouled static track stiffness (k). Because the observed significance, $0.023 < 0.05$; hence, the null *hypothesis 3.3* can be rejected, and alternative *hypothesis 3.4* can be accepted.

3.5.5.2 Empirical Solution

The plotted concatenated data for the longitudinal range of influence (S) and stiffness (k) of fouled track is curve fitted linearly, as shown in Fig. 3.20a. The fouled static track stiffness (k) can be estimated from the empirical solution:

$$k = \frac{S-a}{b} \dots \dots \dots \text{Equation 3.6}$$

Where (a) and (b) are empirical constants and (S) is the longitudinal range of influence obtained from wayside instruments. The curve fitting constants were determined from the data, i.e. $a = -0.75236$; $b = 1.11605$

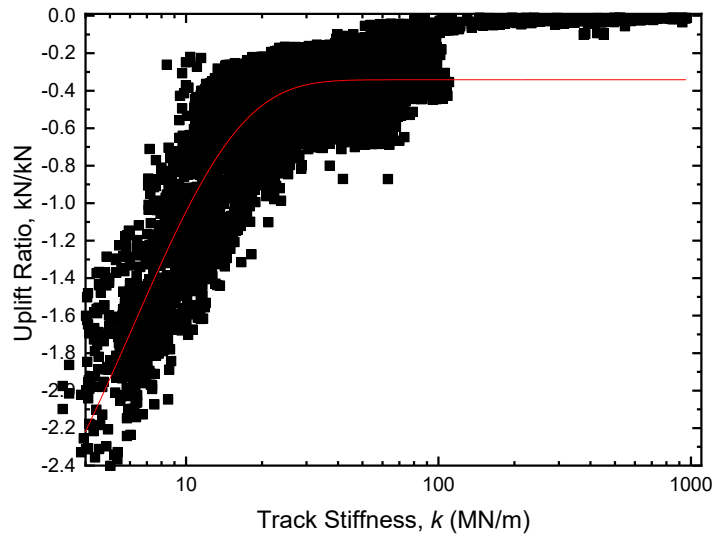
The statistical analysis was performed on total sample size of 23045-wheel loads obtained from 32 trains, and the r-square coefficient of determination (COD) = 0.8168. This means the model explains more than 81.68 % of the variability in (k). Additionally, the strength of linear

relationship between paired data has been tested by Pearson's r , which represents the percentage of points that fall within the regression line. The calculated, $r = 0.9037$, indicates that the curve fitting line passes through 90% of the data points. The exponential fit of the plotted wheel loads data from the 32 trains in terms of cross-tie uplift ratio and fouled static track stiffness (k) is shown in Fig. 3.20b. An empirical model is developed to estimate fouled static track stiffness (k), i.e.:

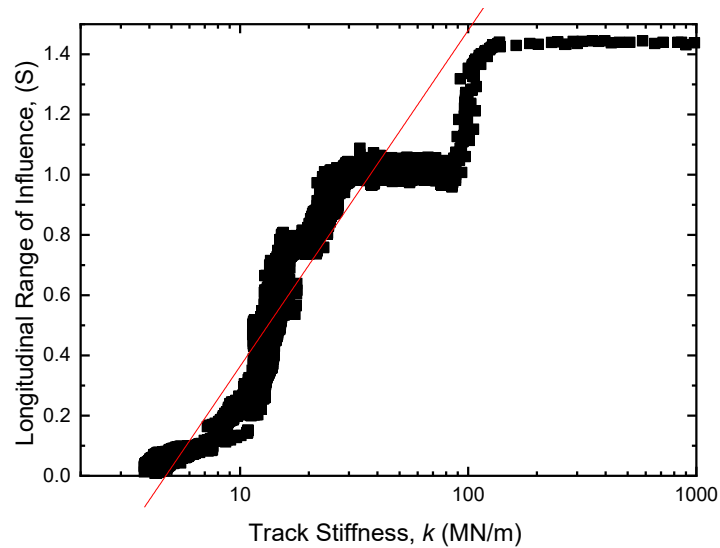
$$k = \frac{\ln\left(\frac{a-UR}{b}\right)}{\ln(c)} \dots \dots \dots \text{Equation 3.7}$$

Where (a), (b), and (c) are empirical constants and (UR) is the uplift ratio captured from wayside instruments. Based on curve fitting the collected data, $a = -0.34161$; $b = 3.6078$; $c = 0.84923$; and $UR =$ uplift ratio (kN/kN)

The goodness of fit of the empirical solution presented in *Equation 3.7* to estimate the fouled static track stiffness (k) from the uplift ratio explains more than 77.07 % of the variability in (k).



(a) Longitudinal Range of Influence



(b) Uplift Ratio

Fig. 3.20 Fouled ballast bed empirical model for: (a) longitudinal range of influence, (b) uplift ratio

3.5.6 Practical Applications

Employing the proposed empirical *Equations 3.6* and *3.7*, a positive fouled ballast bed control system could be established, similar to positive train control systems. The system can monitor unfavorable CWR response at fouled ballast beds (i.e. measurements below the lower limits) and alert users to inspect or maintain fouled ballast beds or tracks prone to fouling. The control system would rely on measurements from calibrated, strain gauges installed at mid-height of the rail along its neutral axis. The instrumentation would be installed on tracks prone to fouling or track segments where train derailment occurred in the past. The strain gauges should be installed in a full-bridge type I configuration to measure rail bending. Using the data gathered from the CWR strain gauges, a program can be trained to calculate the longitudinal range of influence and uplift ratio, which can be used as input parameters for *Equation 3.6* and *Equation 3.7* to estimate static stiffness (k) of fouled track. The proposed approach enables users to estimate fouled static track stiffness (k) from trackside measurements, eliminating the need for conventional load-deflection measurements.

3.6 Summary

Long-term monitoring program was conducted for fouled railroad segment of the Sioux City rail track segment. Candidate fouled ballast bed was instrumented and data was collected from uncontrolled sources (normal train traffic) to establish a relationship between train load and fouled ballast bed and superstructure response. The field data was obtained using a variety of techniques, including conventional rail strain gauge circuits and digital correlation of images obtained by highspeed cameras. The current study demonstrated that instrumentation placed above the cross-tie can provide meaningful data (i.e. longitudinal range of influence of loads on the rail and cross-tie uplift ratio). A method is proposed for continuously measuring spatially varying static fouled static track stiffness by monitoring the longitudinal range of influence for distant wheel load. The proposed method enables estimating fouled static track stiffness (k) from the longitudinal range of influence and uplift ratio. The following observations and conclusions are made:

- (i) The results presented showed that during summertime (i.e. wet railroad conditions) the fouled railroad would have a relatively lower static track stiffness. Meanwhile, during wintertime (i.e. porewater in the ballast is frozen) the fine contaminated railroad is characterized relatively higher static track stiffness.
- (ii) For the test section, the level of water increased gradually across the depth of the fouled ballast. A layer 76 mm starting at depth of 0.102 m and ending at depth of 0.178 m below the bottom of the cross-tie was found highly fouled and was identified as the source of the perched water.
- (iii) At the bottom of the cross-tie (0.025 m) and at a depth of 0.254 m, the water-storage capacity of fouled ballast bed decreased for typical and rigid static track stiffness, i.e. $k \geq 25$ MN/m.
- (iv) When train wheel was at a distance of $0.1S$, i.e. in the rail-crib area, the maximum uplift force developed in the rail-tie instrumented section as the first wheel of the front bogie approached and last wheel departed.

- (v) The linear range of influence of distant wheel loads on the superstructure (rail, cross-tie) and subgrade vertical deflections increased as fouled static track stiffness (k) increased.
- (vi) The bending moments from the enveloping axles generated the highest uplift force on the neutral axis of the CWR. Furthermore, the approaching and departing wheels generated uplift forces in the rail-tie section. Maximum uplift force was generated when the wheel was on the crib area (the hanging segment of the CWR between two cross-ties).
- (vii) Fouled static track stiffness (k) substantially altered the response of fouled track superstructure. Regardless of the railroad condition (clean/fouled), fouled ballast bed performance could be considered acceptable under traffic loading at below-zero ambient temperature (i.e. frozen soil conditions).
- (viii) Employing the tie load ratio as a proxy for cross-tie support efficiency does not capture the response of the superstructure in fouled railroad environment, especially for light wheel loads. Employing the uplift ratio to analyse the uplift forces due to the passage of front and rear wheels of the bogie, and the linear range of influence of distant wheel loads on the rail superstructure offer a better alternative.
- (ix) The fit of plotted concatenated data of wheel loads in terms of the longitudinal range of influence (S) and fouled static track stiffness (k) is almost linear and can predict static track stiffness.
- (x) The fit of plotted concatenated data of wheel loads in terms of the cross-tie uplift ratio and fouled static track stiffness (k) is almost exponentially asymptotic and can be used to predict fouled static track stiffness (k).
- (xi) The statistical analysis demonstrated the suitability of the presented empirical solutions for estimating stiffness (k) of fouled track in terms of (S) and the cross-tie uplift ratio with $R^2 = 81.68\%$ and 77.07% , respectively.
- (xii) Lastly, further field monitoring should involve controlled passes of trains with constant and variable travel speeds. This can help determine whether an optimal combination of train loading and speed can be established to maintain the integrity of fouled static track stiffness.

Chapter 4

4 In-situ Assessment of Cross-tie Vibrations Induced by Freight Trains³

4.1 General

Railway transportation is one of the most environmentally sustainable modes of cargo hauling. Driven in part by the reduction in congestion on highways and emission of air pollutants and greenhouse gases, the European Union commission aims to shift 50% of road freight trips exceeding 300 km to rail and water by 2050 (EC-European-Commission, 2011). However, noise and vibrations associated with train traffic are considered environmental pollutants (Thompson et al., 2019). Particularly in heavily populated zones, noise and vibration due to the traversing inter-city trains are a major cause of nuisance for residents. Trains generate surface waves (mainly Rayleigh waves) travelling with long wavelengths and low velocity that could impact a wide zone depending on cross-tie conditions. The mechanical vibrations are generated in the track when the passing train induces a varying force on the railroad. The force pattern is influenced by the railroad superstructure components, such as rail, spikes, cross-ties, between the wheel and the substructure. Consequently, the vibration waves that propagate into the railway superstructure then through the track foundation to the surroundings as shown in Fig. 4.1 are influenced by the conditions of the railroad components. Vibration is initiated at the wheel-rail interface due to quasi-static (dynamic ride/moving axels) loads and dynamic wheel/rail loads, transmitted to the sub-structure by the cross-ties (Cai et al., 2010; Jensen et al., 2015; Thompson et al., 2019; Ouakka et al., 2022). The vibrations induced by the axel excitations are caused by several mechanisms: wheel out of roundness, rail

³ A version of this chapter has been submitted for possible publication in the Journal of Soil Dynamics and Earthquake Engineering: Touqan, M., El Naggar, M.H., & Stark, T.D. (2022). In-situ Assessment of Track Borne Vibrations Induced by Freight Trains Journal of Soil Dynamics and Earthquake Engineering, (Under review)

corrugation/roughness, impact wheel loads due to rail joints/ wheel flats, and parametric excitation due to cross-tie periodicity (Lombaert et al., 2015; Thompson et al., 2019).

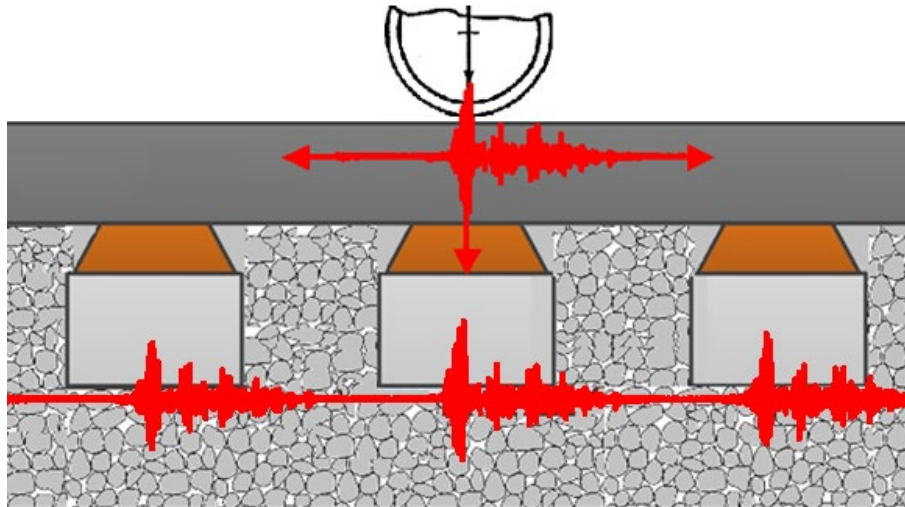


Fig. 4.1 Vibrations transmittal to substructure via superstructure

Railway induced vibrations are affected by the complex nature of the medium in which the vibrations travel. The mechanical properties of the ballast and underlying natural soil, and the potential variation of fouled substructure affect the vibration characteristics, and hence complicate the analysis to evaluate train induced vibrations. Ewing et al. (1957) pioneered studies of problematic vibrations from railway traffic by simplifying the analysis considering wave propagation through elastic media from point and line sources. Early experimental studies of railway vibrations considered interaction between the cross-ties and the ballast (e.g., Richart (1970), Dawn (1983), Volberg (1983), and Melke (1988). Volberg (1983) measured vibrations induced by railway traffic and reported that the vibrations increased in tracks laid on stiff subgrade more than in soft clay as propagating waves attenuate faster in clay subgrade. This underscored the importance of evaluating the static track stiffness as it influences the response of track components below the rails (rails pads, spikes, cross-ties, cross-tie pads) and substructure (ballast, sub-ballast, sub-grade) to quasi-static and axel excitations (Milne et al., 2019).

Esmaeili et al. (2014) investigated the effect of sand fouling on the static track stiffness and the vibration transmissibility. They probed the vibrational behaviour of railroads on tracks fouled by wind-carried sand particles and reported that the track fouling caused an increase in the static track stiffness. This resulted in reducing the track deflection by 68.0 % but increased the maximum acceleration by 43.0 %. This study, however, did not consider the effect of fine material (silt/clay) fouling on the static track stiffness and the transmissibility of track vibration. In addition, the effects of environmental conditions such as temperature and subgrade moisture content were not studied.

Vibration mitigation measures at the source of vibration have been investigated. Lombaert et al. (2015) listed four mitigation measures: wheel truing, rail reprofiling (Wilson et al., 1983; Nelson, 1996; Grassie, 2012), reducing vehicle loads by modifying bogie and axle distance (Wilson et al., 1983) and using resilient wheels (Kouroussis et al., 2010). Additional mitigation measures at the source of vibration include stiffening of track subgrade (Adam et al., 2007; Peplow and Kaynia, 2007) and modifying track superstructure. The latter is of particular importance because track superstructure geometric unevenness causes variability in the support stiffness at each cross-tie, which results in parametric excitation (Hunt, 2005; Johansson et al., 2008). Resilient superstructure components would confine the vibration energy in the superstructure, hence reducing the energy radiated into the soil (Lombaert et al., 2015). The vibration energy leaked to the free field is related to the phase velocities of the railway track borne waves and the soil Rayleigh waves (Lombaert et al., 2006; Lombaert et al., 2015). Therefore, it is necessary to evaluate the wave propagation in the track to devise a proper method for minimizing the vibrations at the source.

Hanson (1995) listed the important train operational and vehicle factors that influence vibration including high speed, stiff primary suspension and out of round wheels. In addition, subgrade conditions such as track foundation stiffness and damping, and depth of bed rock influence the magnitude of vibrations. For example, the wave propagation is more efficient in stiff clay soils, and shallow bedrock reflects the vibrations to the surface, which increases the vibration amplitudes away from the track. However, neither study quantified the vibrational response of

the superstructure due to cyclic train loading. Kaewunruen and Remennikov (2007) investigated vibration of railway concrete cross-ties. Although important outcomes utilizing the Timoshenko-beam on elastic foundation theory were presented, nonetheless the study was limited to numerical modelling. Kaewunruen and Remennikov (2007) presented results on the effect of voids on the dynamic properties of prestressed concrete cross-ties. However, their was limited to physical testing. Vibrations induced by trains were measured both on the railway track and on the free-field by Costa et al. (2012), however, their study did not investigate voided cross-ties in fouled railroad. A comprehensive in situ track vibration assessment of the dynamic interaction between cross-ties and fouled ballast has rarely been studied.

The current study aims to quantify cross-tie vibrations by utilizing accelerometers mounted on the concrete monoblock cross-ties. A special emphasis is placed on assessing the acceleration response of voided cross-ties compared with supported cross-ties. In addition, vertical acceleration response charts were plotted to examine the effect of train velocity and static track stiffness on the behaviour of both voided and supported cross-ties. The vibration of cross-ties in the fouled segment of the track is compared with the cross-tie vibration at the clean section to elucidate the effect of ballast fouling.

4.2 Measurement Site, Accelerometer Array, and Test Trains

The railroad test segment is located in the city of Parkville, Missouri, USA (39°11'22.6"N 94°41'21.1"W). The instrumented site was a 281m single track segment of the 175 km Sioux City BNSF railway network. The superstructure and substructure were constructed in accordance with the American Railway Engineering and Maintenance-of-Way Association. The characterization of the substructure materials is presented in Chapter 2. The mechanical properties of the fouled material, shown in Table 4.1, were evaluated following the general provisions of ASTM standard D 6913 (ASTM, 2004). Based on AASHTO M 145 system (AASHTO, 2008), the fouled ballast was classified as A-1-a (stone fragments, gravel, and sand), the fouled sub-ballast was classified as A-2-4(0). The sub-grade was classified as A-2-4(0). However, according to Soil Classification System (USCS), the fouled Ballast was

classified as Poorly Graded Gravel (GP), and the fouled sub-ballast was classified as Well Graded Gravel (GW) with sand. The sub-grade was classified as Silty Sand (SM). Fouling changes with time, especially when the source of fouling is not particle breakage or attrition. As the water table level rises and falls, it drags the fines from the subgrade with it. This was clearly indicated by comparing observations made during two site visits; percent fouling of the ballast ranged from 58% to 67% as shown in Table 4.2. Samples' analysis showed that as the percent fouling decreased, clay activity of fine materials also decreased.

A total of 32 (including rolling stock data) heavy haul freight trains were monitored and corresponding track vibrational response has been analyzed. However, measured responses in temporal and frequency domains for only six selected trains were presented as typical results. The measured data of the six trains were based on the front locomotives of the rolling stock. The trains travelled through the monitoring section at the following times: 20/Dec/2017-15:15, 31/Dec/2017-14:22, 06/Jan/2018-15:43, 20/Jan/2018-13:34, 20/Jan/2018-14:32, and 09/Jan/18-08:11, hereafter referred to as: Train A, Train B, Train C, Train D, Train E, and Train F respectively.

During site visits the track was inspected and two clean zone and a 12 m fouled zone in between. The track in the test section was instrumented with strain gauges to monitor the wheel load and track and cross-ties' deflections. In addition, high-speed cameras were used to monitor track deflection. The details of these instrumentation devices and high-speed cameras are presented in Chapter 3. Furthermore, an array of nine (9) aligned weather-resistant high accuracy accelerometers (frequency 1 Hz) was used to monitor the cross-ties' vibration. The measured acceleration time histories are utilized to evaluate the cross-ties response to wheel loads from traversing trains. The accelerometers were attached to different cross-ties within the fouled and clean track segment. The accelerometers were mounted on the concrete cross-ties as shown in Fig. 4.2 to measure cross-tie vibration. They were attached using steel plates and bolts drilled in the cross-tie, which did not interfere with train operations allowing long-term monitoring. The accelerometer network was linked with an eight (8) channel National Instruments (NI-cDAQ-9172) data acquisition system. The data acquisition system collected

cross-tie acceleration readings at a time interval of 2.4×10^{-4} second per measurement. The layout plan of all sensors is presented in Fig. 4.3.

Table 4.1 Characteristics of the fouled sub-ballast

Sub-Ballast Property	Value
Maximum Dry Density, ρ_d	1.93
Friction Angle, ϕ	40.00°
Plasticity Index, PI	10.00
Specific Gravity, G_s	2.65
Coefficient of Uniformity, C_u	25.10
Coefficient of Curvature, C_c	2.80
D_{10}	0.30 mm
D_{30}	3.10 mm
Mean Diameter, D_{50}	7.40 mm
D_{60}	9.51 mm

Table 4.2 Railroad fouling parameters

Ballast Sample Date	Percent Fouling (%)	W_N (%)	LL (%)	PL (%)	PI (%)	Activity	USCS Symbol
05/Dec/2017	67	17.8	39	30	9	0.13	CL
06/Apr/2018	58	9.4	25	20	6	0.09	CL-ML



Fig. 4.2 Cross-tie mounted accelerometer

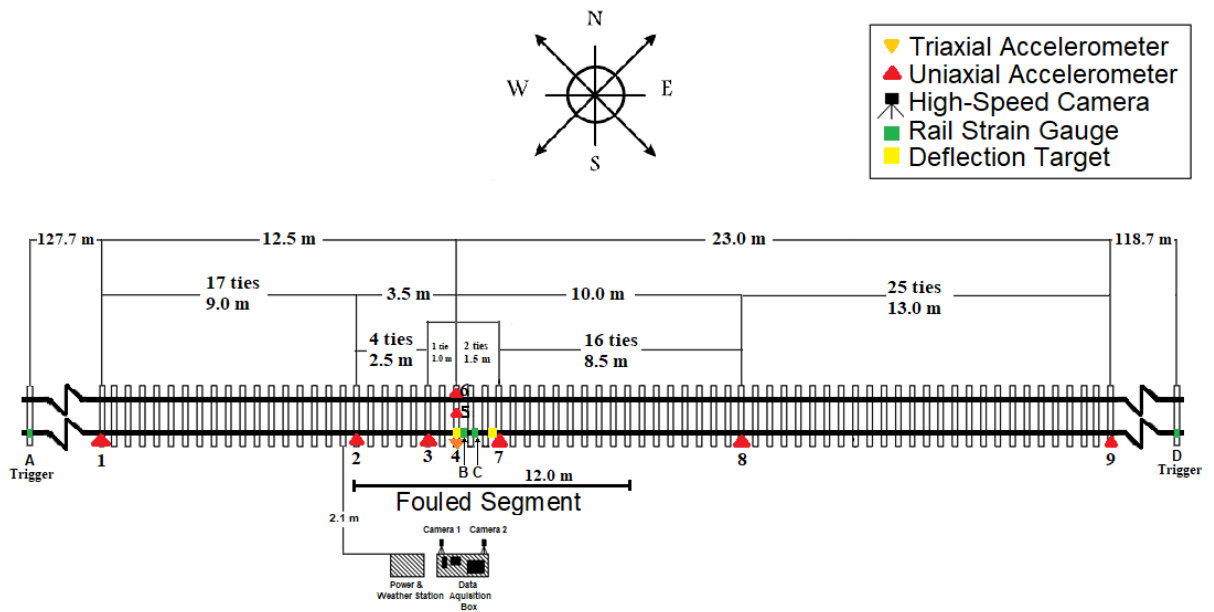


Fig. 4.3 Accelerometer measurement array layout plan

The static track stiffness (k) is a measure of the vertical stiffness of both its superstructure and the substructure. It is calculated using peak wheel loads and the maximum rail deflections for the locomotives and rolling stock, which can be estimated by:

$$k_{avg} = \frac{\sum_{n=1}^N k_{n=1}}{N} \dots\dots\dots \text{Equation 4.1}$$

Where,

$$\sum_{n=1}^N k = \left(\frac{P_{max_1}}{\delta_{max_1}} + \frac{P_{max_2}}{\delta_{max_2}} + \dots\dots + \frac{P_{max_N}}{\delta_{max_N}} \right)$$

P_{max} = Maximum Wheel Load Applied on the Crib Area

δ_{max} = Maximum Rail Deflection of the Crib Area

$n = 1^{st}, 2^{nd}, 3^{rd}, 4^{th} \dots\dots\dots N^{th}$ wheel

$N =$ Total Number of Wheels

Trains A and D were chosen as typical data because at the time of passage through the fouled instrumented track, static track stiffness (k_{avg}) was estimated to be ≈ 20.5 MN/m, and 8.2 MN/m, respectively. The estimated static track stiffness (k_{avg}) at the time of passage of Trains A and D, were the least during the monitoring period of the railway track (November 2017-April 2018). This was because the track experienced the highest track deflection due to the unfavorable environmental circumstances that resulted in poor track support condition. Meanwhile, during the crossing of Trains B and C, the average static track stiffness (k_{avg}) was found to be ≈ 82.0 MN/m and 72.4 MN/m, respectively. The fouled static track stiffness values during the crossing of Trains B and C were amongst the highest estimated for the monitored period. Moreover, Trains E and F crossed the railroad at typical static track stiffness, 51.1 MN/m and 54.1 MN/m, respectively. Table 4.3 shows static track stiffness information for the selected trains. The details of analyses performed to estimate the static track stiffness are presented in Chapter 3.

Table 4.3 Test trains operation conditions and rail-crib stiffness data

Train	Train Traverse		Fouled Static Track Stiffness	Train Velocity
ID	Date	Time	k_{avg}	V_T
	(dd/mmm/yy)	(hh:mm)	(MN/m)	(km/h)
A	20/Dec/17	15:15	20.5	77.0
B	31/Dec/17	14:22	82.0	57.0
C	06/Jan/18	15:43	72.4	56.0
D	20/Jan/18	13:34	28.2	27.0
E	20/Jan/18	14:32	51.1	95.4
F	09/Jan/18	08:11	54.1	110.0

4.3 Acceleration Signal Analysis

The time domain analysis of measured data of all test trains were based on the forward bogie of the front locomotives of the rolling stock to ensure minimum variance in wheel loading conditions, and to avoid interference from bogies in proximity (i.e. coupled wheel loads from consecutive cars). In the current study, a two-pronged approach was implemented to analyze the acceleration signal, i.e.: time, and frequency domains, for the quantification of cross-tie vibrations. Furthermore, this study also probed the influence of train velocity and static track stiffness on the temporal response of supported and voided cross-ties.

4.3.1 Time Domain Analysis

Fig. 4.4 shows the cross-tie acceleration in the fouled and clean segments due to train A traversing the instrumented segment. The first peak of the acceleration signal is considered to be the cross-tie response to the applied wheel load. Fig. 4.4a displays the superimposed acceleration signals for adjacent ties (accelerometer 3 and accelerometer 4), which demonstrate comparable acceleration pattern and most importantly, acceleration magnitudes for the fouled segment. This indicates the instrumentation reliability and precision. However, the acceleration time history recorded by accelerometer 4 shows a slightly higher response because this particular cross-tie in the fouled segment was severely voided as observed during site visits.

Each acceleration data collection epoch was initiated as the wheel load signal was received from the trigger strain gauge located at 140.2 m from the triaxial accelerometer 4. The distance between accelerometer 4 and the trigger strain gauge was used to estimate the train velocity. The travel time (i.e. time for the train to cross the distance from the trigger sensor to accelerometer 4) may be calculated using the x-axis coordinate of the first peak on the acceleration time history, i.e.:

$$Velocity = \frac{D}{T} \dots\dots\dots \text{Equation 4.2}$$

Where,

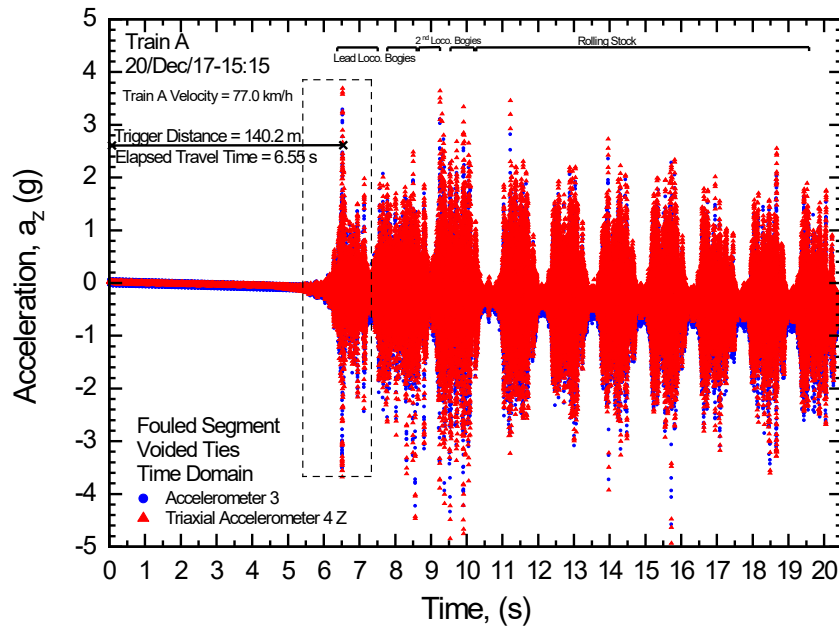
D = Distance between trigger strain gauge sensor and the accelerometer analyzed

T = Train travel time from trigger sensor location to accelerometer location.

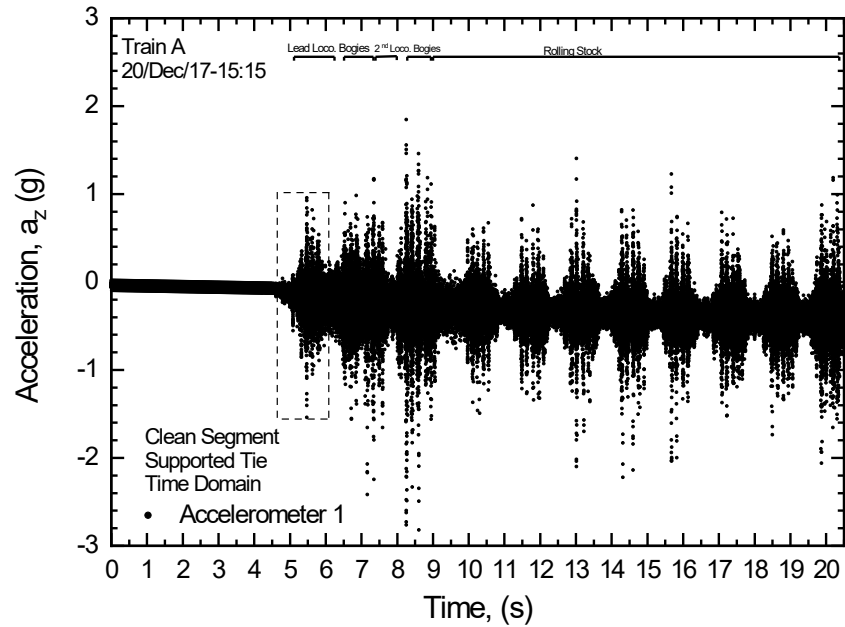
With reference to Fig. 4.4a, the velocity of Train A was estimated using *Equation 4.2* to be $V_{Train A} = 77.0$ km/h.

The pattern and amplitude of the acceleration signal depend on train and track support parameters. In general, the measured Z-axis acceleration amplitudes (both +ve and -ve) were higher for the fouled segment as can be observed by comparing the results in Figs. 4.4a and 4.4b. For the passage of the forward bogie of Train A travelling at $V_{Train A} = 77.0$ km/h and a fouled static track stiffness of $k_{avg} \approx 20.5$ MN/m, the maximum vertical acceleration of the

voided cross-tie was $a_z = \pm 3.8$ g, while the maximum acceleration of the supported cross-tie in the clean segment was $a_z = \pm 1.0$ g. The relatively low static track stiffness in the fouled segment, mainly due to ballast contamination with fines, in addition to the presence of the cavities beneath the cross-ties, amplified the response under wheel loading, especially along the Z-axis. This imposed high stresses on the ballast cross-tie interface. As the stresses increased at the ballast-tie interface, the load on the super structure increased and consequently cracks developed in the cross-tie and the cross-tie fastening system could fail prematurely. Moreover, continuous increase in stresses at the cross-tie ballast interface would eventually cause ballast crushing and increased fouling of the ballast material. The increase in fine materials would in turn exacerbate the drainage problem of fouled ballast, which would reduce the ability of the railroad structure to cope with cyclic wheel loads.



(a)



(b)

Fig. 4.4 Response of cross-ties due to Train A crossing: (a) fouled segment, (b) clean segment

Fig. 4.5 displays the vertical acceleration of the cross-ties during the passage of the forward bogie of Train D. The effect of transitioning from a high static track stiffness (clean segment) to a low static track stiffness (fouled segment) can be inferred from the results presented in Fig. 4.5. In addition to excessive superstructure deflection, significant vibrations were measured. For the front bogie of the lead locomotive of Train D crossing at $V_{Train D} = 27.0$ km/h and static track stiffness $k_{avg} \approx 28.2$ MN/m, the measured maximum vertical acceleration of the voided cross-tie was $a_z = \pm 4.1$ g. This means the response of the poorly supported cross-tie in the fouled segment was 400% of that for the supported cross-tie, which exhibited maximum acceleration $a_z = \pm 1.0$ g.

Zhang et al. (2017) suggested that dynamic amplification increases as the train velocity increases. However, comparing acceleration amplification for trains A and D, indicates minor

difference of amplification. For Train A crossing the fouled segment at $V_{Train A} = 77.0$ km/h, the voided cross-tie amplified the response 3.8 times compared to the well supported cross-tie. On the other hand, for Train D traveling at $V_{Train D} = 27.0$ km/h, the voided cross-tie amplified the response 4.1 times compared with the well supported cross-tie. It appears that the influence of static track stiffness has a greater effect on the acceleration amplitudes for lower train speeds. This is attributed to the difference in the static track stiffness at the time of crossing of both trains; the static track stiffness during the passage of Train D was 71.4 % higher than the static track stiffness during the passage of Train A. The higher static track stiffness is attributed to good support condition associated with favorable environmental conditions (sub-zero ambient temperature and low track moisture content).

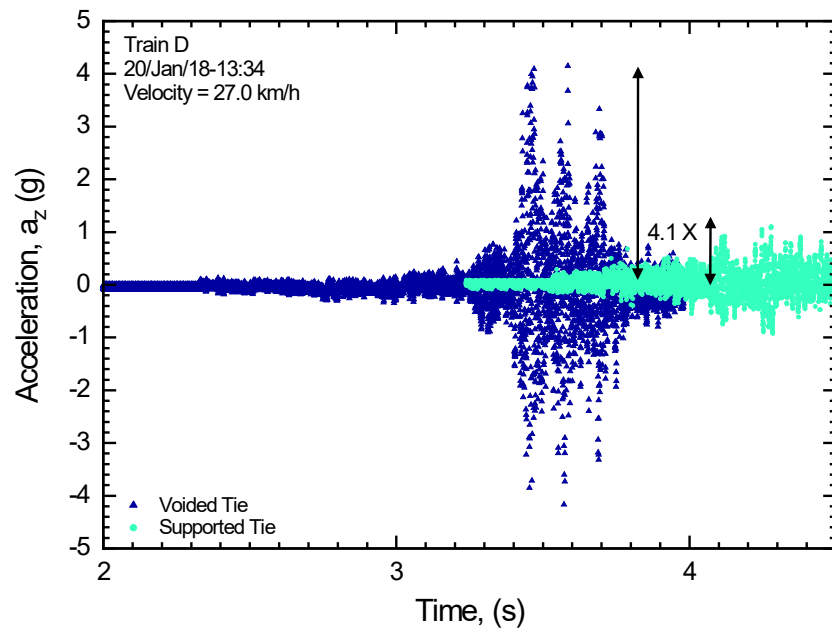


Fig. 4.5 Response of cross-ties due to Train D crossing

For the fouled segment, favorable environmental conditions result in reduced track deflection, but increased vibrational response. Figs. 4.6 and 4.7 show the effect of high static track stiffness, $k_{avg} \approx 82.0$ MN/m and $k_{avg} \approx 72.4$, on the excitation of supported and voided cross-

ties during the passage of the forward bogie of Train B and Train C, respectively. For Train B ($V_{Train B} = 57.0$ km/h and $k_{avg} \approx 82.0$ MN/m, the acceleration signature for each wheel as it crossed the cross-tie is distinctive, (i.e. fewer number of noise vibrational peaks produced for each wheel). Fig. 4.6 shows that the increase in static track stiffness amplified the response of the voided cross-tie to $a_z = \pm 9.6$ g, which was about 13.7 times the response of the supported cross-tie ($a_z = \pm 0.7$ g). On the other hand, when static track stiffness was $k_{avg} \approx 72.4$ MN/m during the passage of Train C and the acceleration response ($a_z = \pm 5.5$ g) was 7.9 times the acceleration response of the supported cross-tie ($a_z = \pm 0.7$ g) as shown in Fig. 4.7. Given that the velocities of trains B and C were nearly equal (average velocity of 56.5 km/h), the difference in acceleration amplification on fouled railroad is attributed to the difference in static track stiffness. This observation is in agreement with Hanson (1995) and Quagliata et al. (2018), which indicated that the increase in track rigidity (i.e. timber cross-ties embedded in a concrete slab track bed) would result in higher acceleration levels.

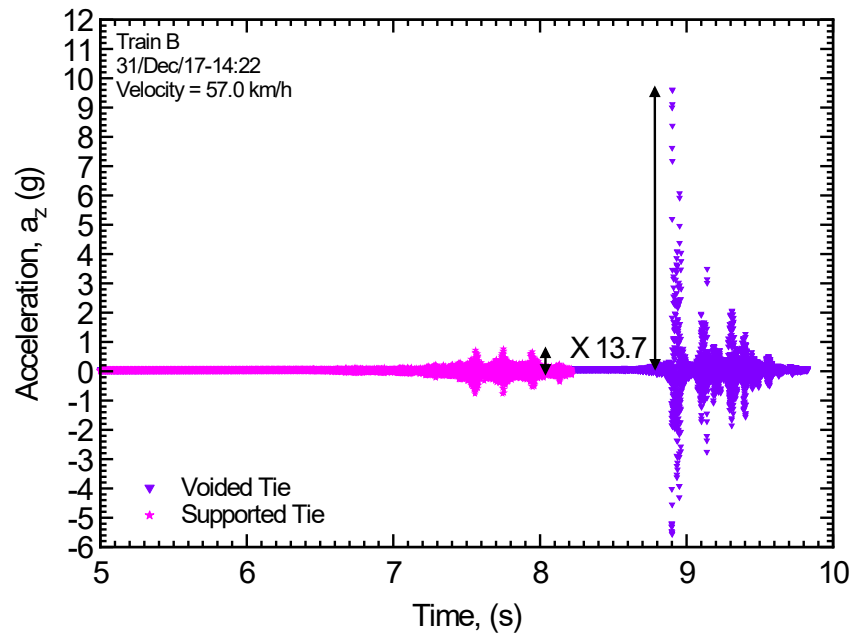


Fig. 4.6 Acceleration of cross-ties due to Train B crossing

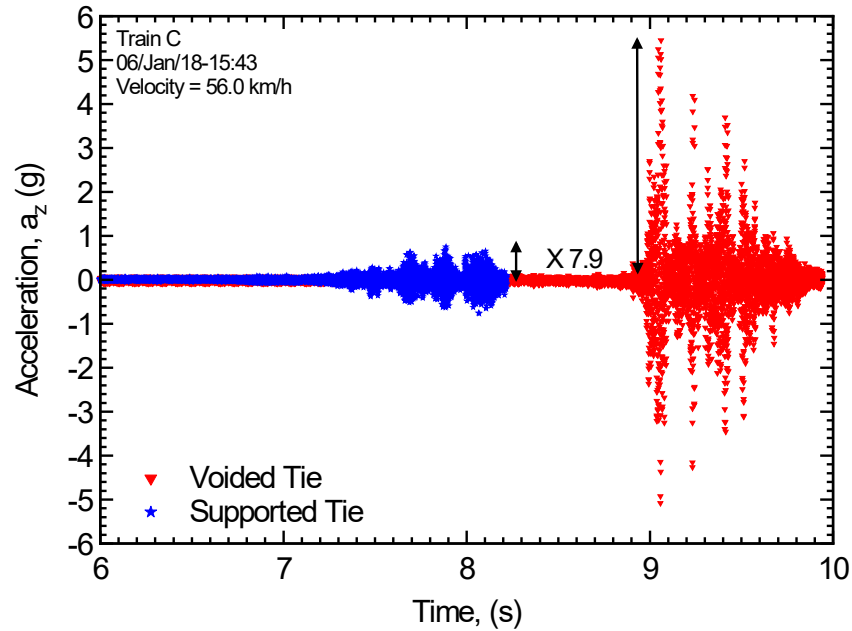


Fig. 4.7 Acceleration of cross-ties due to Train C crossing

It may be concluded that the train induced acceleration of voided cross-ties is proportional to static track stiffness. This is because the cavities underneath the cross-tie that are filled with fines are influenced more by the moisture content and ambient temperature. On the other hand, clean ballast drains water properly and attenuates the acceleration as it offers higher energy dissipation (i.e. damping). The details of analyses performed to estimate the effect of environmental conditions and drainage on the response of the superstructure were presented in Chapter 2.

Figs. 4.8 and 4.9 show the response of the track superstructure during the passage of the forward bogie of Train E and F, respectively. Both represent typical static track stiffness observed during the monitoring period of the test site. Train E was travelling at 95.4 km/h on a fouled railroad static track stiffness ($k_{avg} \approx 51.1$ MN/m). The results demonstrate that the acceleration of the voided cross-tie was twice that of the supported cross-tie. Also, as expected, the vibrations due to Trains E and F were higher than vibrations due to Train A that had lower

velocity ($V_{Train A} = 77.0$ km/h) and lower static track stiffness ($k_{avg} \approx 20.5$ MN/m). The maximum acceleration amplitudes at supported and voided cross-ties for train A were $a_{z supported} = \pm 1.0$ g, and $a_{z voided} = \pm 4.1$ g, while the maximum acceleration amplitudes for Train E and Train F were $a_{z supported} = \pm 2.5$ g and $a_{z voided} = \pm 7.6$ g. These results indicate the acceleration amplitudes increased by more than 200% as the train velocity and static track stiffness increased.

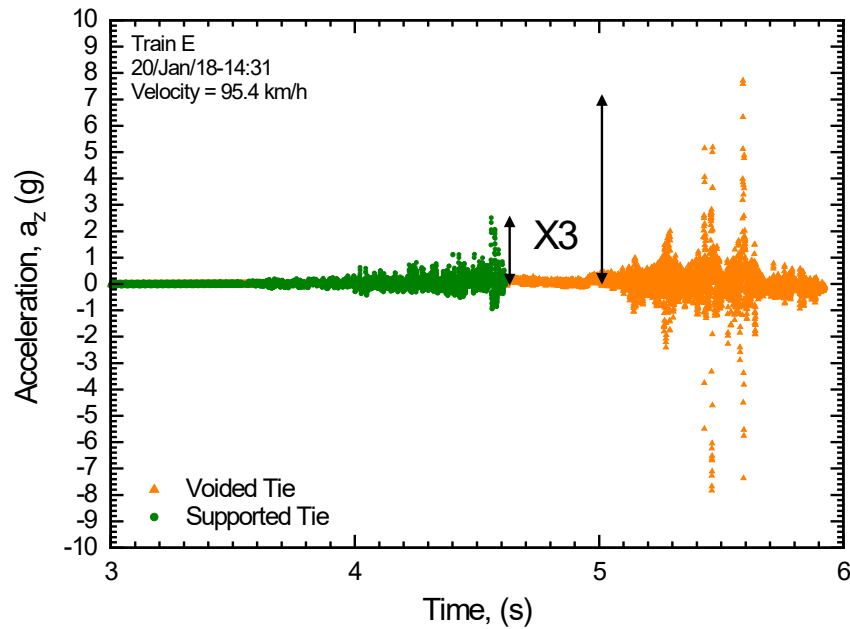


Fig. 4.8 Acceleration of cross-ties due to Train E crossing

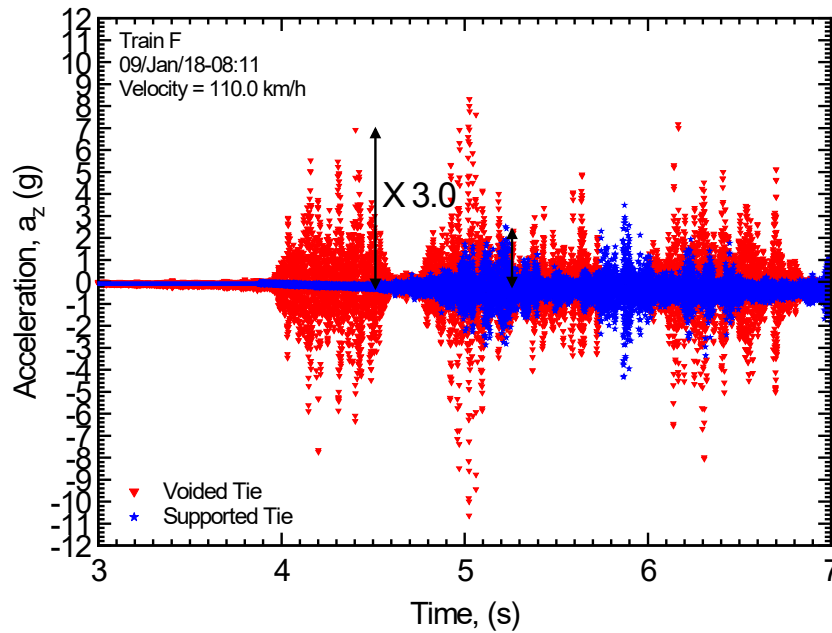


Fig. 4.9 Acceleration of cross-ties due to Train F crossing

In general, the accelerations of the supported and voided cross-tie varies can be compared in terms of their magnitude. To understand the effect of the voids beneath the poorly supported cross-ties, the ratio of the acceleration of the voided cross-tie to the acceleration of the supported cross-tie, is calculated. The impact of the lack of support on the vibrational response of the poorly supported cross-tie, can be quantified by:

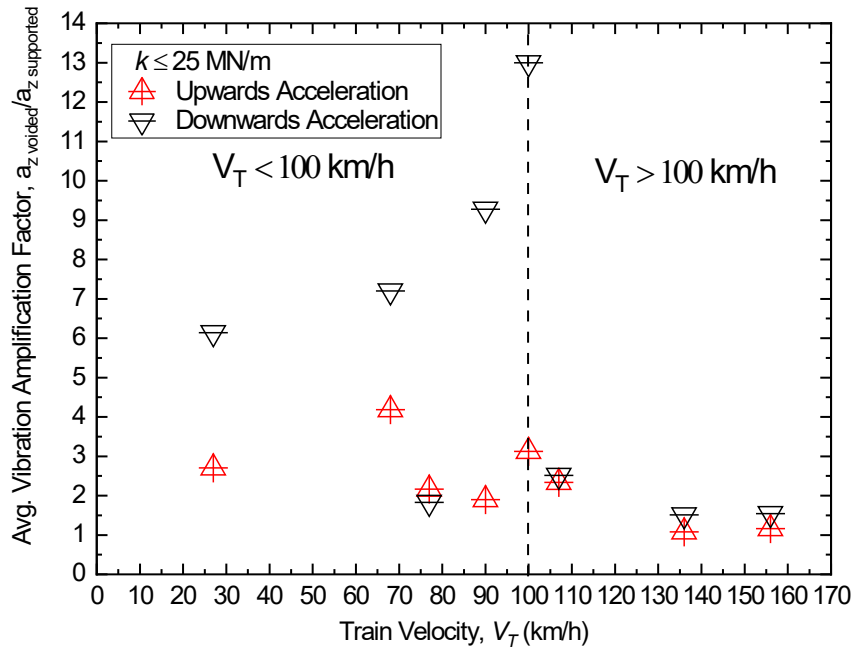
$$\text{Voided Cross-tie Vibration Amplification Factor} = \frac{a_{z \text{ voided}}}{a_{z \text{ supported}}} \dots\dots \text{Equation 4.3}$$

Fig. 4.10 summarizes the variation in voided cross-tie amplification factors for different trains' velocity, including locomotives and rolling stock data. As shown in Fig. 4.10a, for $V_T \leq 100$ km/h the amplification of vibrational response is correlated with train velocity. The results demonstrate that the downwards acceleration component (i.e. measured negative acceleration amplitudes in Z-axis) of the voided cross-tie amplified from 6 to 13 times when compared to downwards acceleration component of supported cross-ties. Nonetheless, upwards acceleration component also experienced amplification, however it did not show sensitivity to

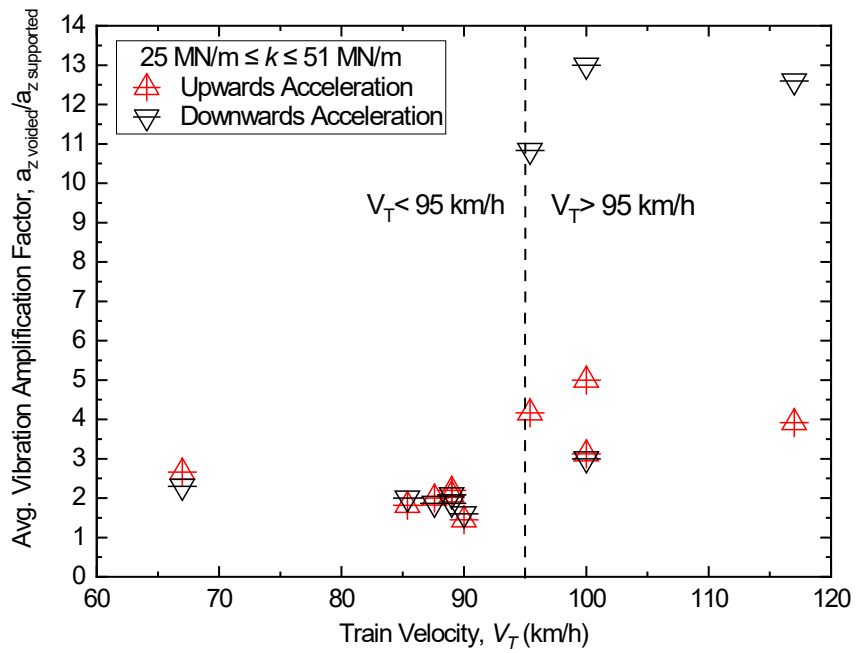
the increase in train velocity. Upwards acceleration component amplification response was around 3 times that of the supported cross-tie. Moreover, for $V_T > 100$ km/h, voided cross-tie vibration amplification factor was comparable for the upward and downward acceleration components, which was found to be around 1.0. At inflection point $V_T > 100$ km/h, the decrease in the amplification of vibrations for soft track can be explained in part by the mud pumping phenomenon. At high train speed, the viscous fine-rich sub-grade gets pumped towards the surface cushioning the cross-tie and dampening vertical deflection.

Fig. 4.10b presents the variation in voided cross-tie amplification factors with train velocity for typical static track stiffness. Results show that for $V_T \leq 95$ km/h and static track stiffness $25 \text{ MN/m} \leq k \leq 51 \text{ MN/m}$ the upward and downward amplification factors are similar (i.e. the increases in the downward and upward acceleration magnitudes are comparable). However, for the typical static track stiffness and $V_T > 95$ km/h it was found that downward acceleration component amplified up to 13 times for voided cross-ties when compared with supported cross-ties. Meanwhile, the upwards acceleration component amplified 4 times the response of the supported cross-ties. For rigid fouled track (i.e. $k \geq 51 \text{ MN/m}$), when $V_T > 95$ km/h, downwards acceleration amplification factors decrease from 13.0 to around 1.0, as shown in Fig. 4.10c. Meanwhile for train velocity $55 \text{ km/h} \leq V_T \leq 95 \text{ km/h}$, the amplification of the upwards acceleration component is twice (i.e. $\frac{a_{z \text{ voided upwards}}}{a_{z \text{ supported upwards}}} = 10.0$) that of the downwards (i.e. $\frac{a_{z \text{ voided downwards}}}{a_{z \text{ supported downwards}}} = 5.0$).

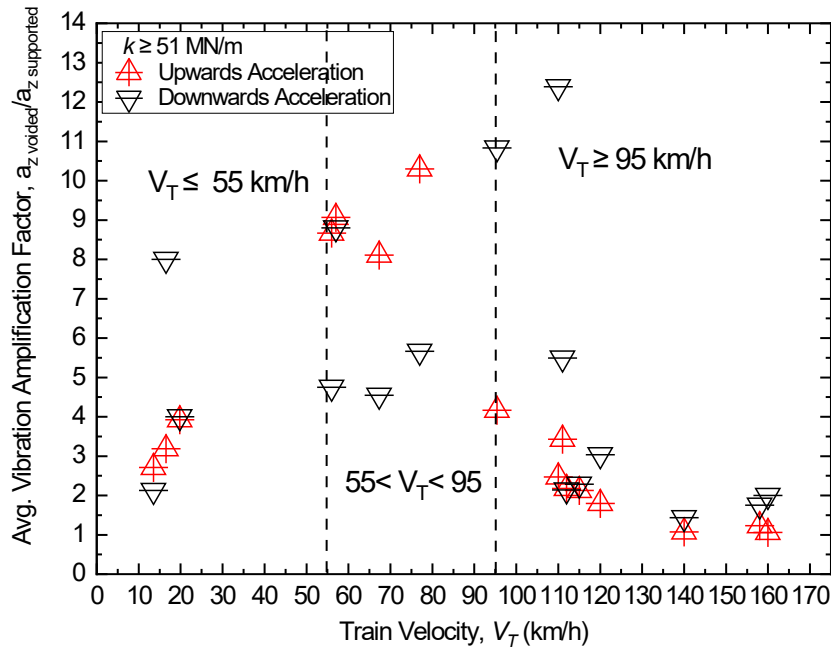
As the static track stiffness and train speed increase at inflection point $V_T > 95$, the unbalanced force created by the moving train produces vibrations that are reflected and transmitted to the cross-tie. This can be explained due to the absence of voids within the ballast. Air voids within the ballasts act as dampeners that absorbs and disperses vibrations.



(a)



(b)



(c)

Fig. 4.10 Variation of vibration amplification factor with train velocities for: (a) $k \leq 25$ MN/m, (b) $25 \text{ MN/m} \leq k \leq 51 \text{ MN/m}$, (c) $k \geq 51 \text{ MN/m}$

4.3.2 Frequency Domain

In the current study accelerometer data is analysed to obtain the displacement data from the acceleration signal. However, several studies noted that prior to obtaining the displacement data from the acceleration measurements, a high-pass filter must be applied to prevent low frequency drift (Bowness et al., 2007), and denoise the data to obtain the tie displacement data (Milne et al., 2018). Therefore, to characterize the displacement signals, the signals were filtered twice and integrated twice (i.e., once to obtain the tie's velocity, and the second time to obtain the tie's displacement (Bowness et al., 2007; Joh et al., 2014; Le Pen et al., 2016; Milne et al., 2017; Milne et al., 2018). The Butterworth filter is a method of infinite impulse response signal process employed to avert baseline error when processing dynamic data (Boore et al., 2002). The Butterworth High-Pass Filter (BHPF) is applied prior to the integration of

the signals (Zhang et al., 2017; Milne et al., 2018). The filter order of the applied BHPF did not exceed 13, i.e. $(n) \leq 13$. The BHPF was employed, i.e.:

$$H(u, v) = \frac{1}{1 + (\frac{F_c}{r})^{2n}} \dots \dots \dots \text{Equation 4.4}$$

Where,

$$u = 0, 1, \dots M-1$$

$$v = 0, 1, \dots N-1$$

(M, N) = Frequency domain coordinates

F_c = BHPF cut-off frequency, a key parameter within the range (0, 0.5)

$$r = \sqrt{(u^2 + v^2)}$$

N = an integer number representing the filter order

Measured acceleration due to test trains cyclic loading were processed using spectrum analysis for both supported and voided cross-ties for trains under study including locomotives and rolling stock data. The results presented in this section provides an in-depth understanding of the vibration profile measured, where the acceleration amplitude (g) is plotted as a function of frequency (Hz). The Fast Fourier Transform (FFT) presents the transfer function of the cross-tie support condition. To perform the FFT, a C-subroutine from the Fastest Fourier Transform in the West (FFTW) library was utilised. In the FFTW, the Cooley-Tukey FFT algorithm was executed to calculate the Discrete Fourier Transform (DFT), i.e.:

$$F_n = \sum_{i=0}^{N-1} x_i e^{-\frac{2\pi j}{N} ni} \dots \dots \dots \text{Equation 4.5}$$

Where,

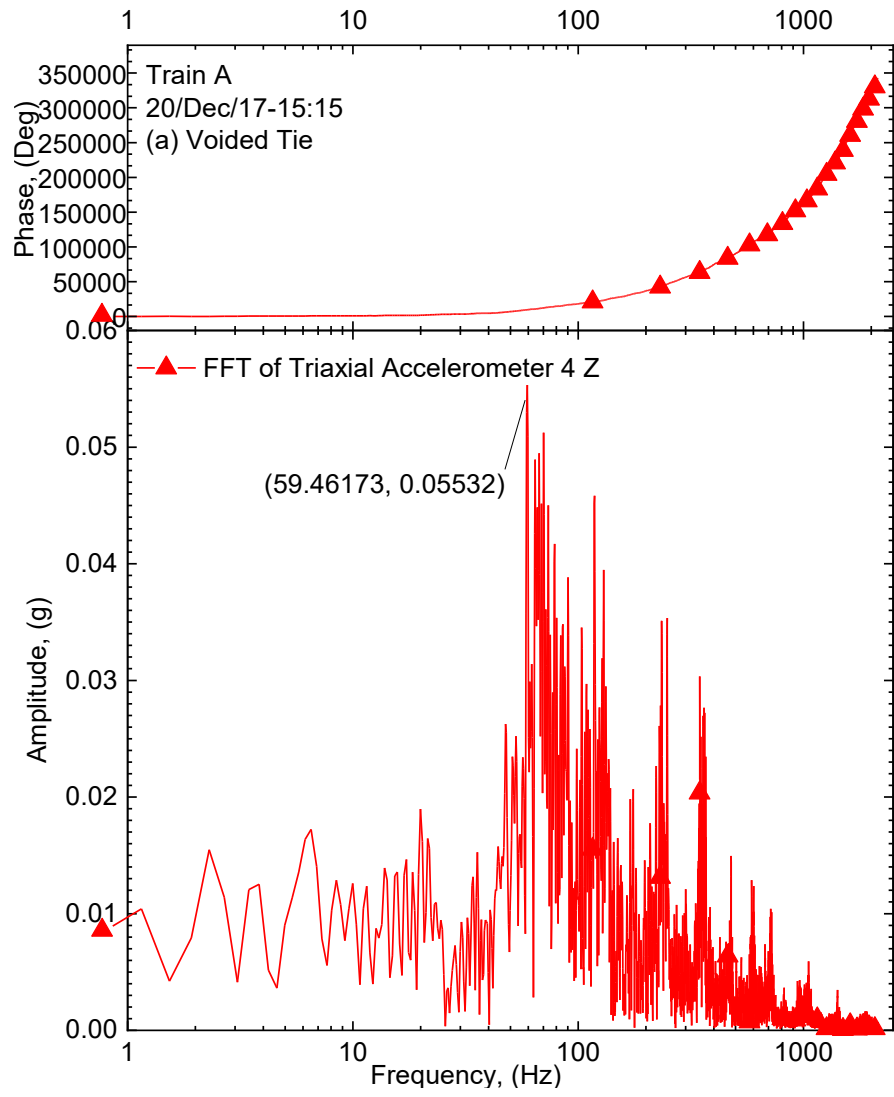
F_n = transformed sequence of N complex numbers

x_i = an array of N complex numbers

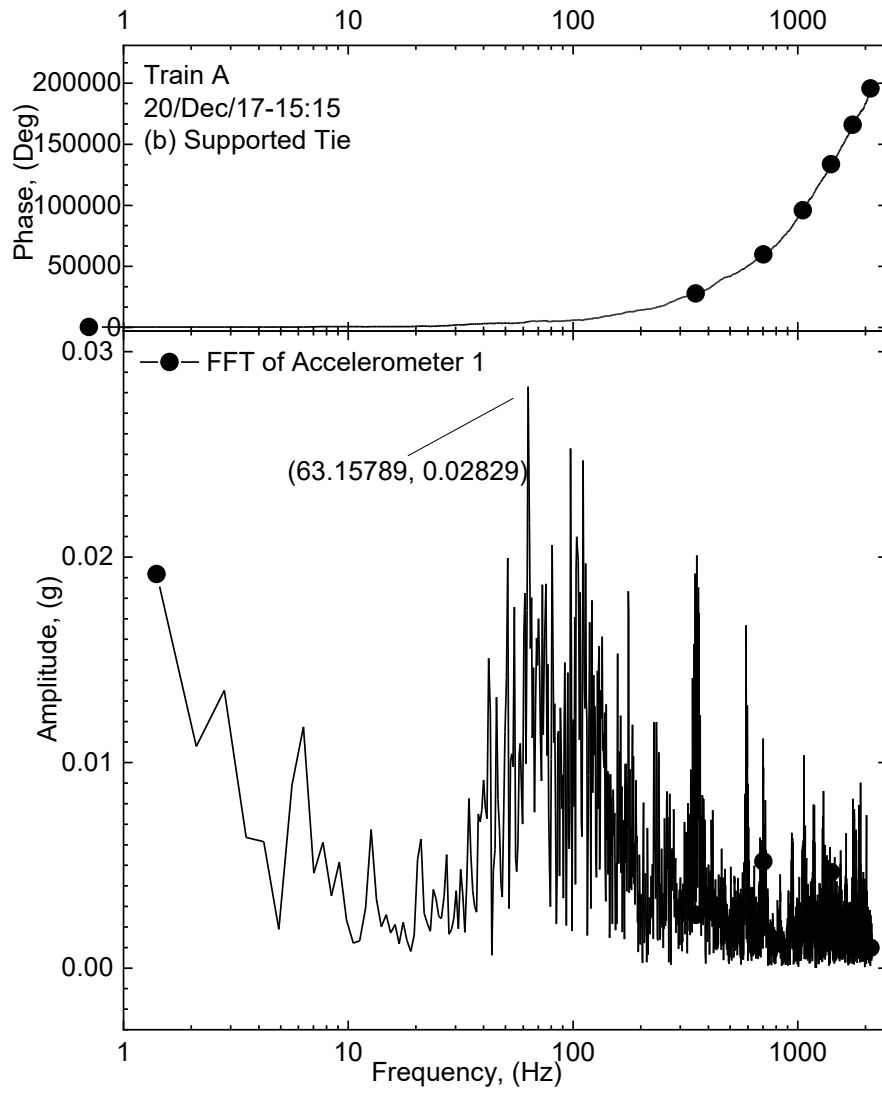
$0 \leq i \leq N; 0 \leq j \leq n; e^{-\frac{2\pi j}{N}}$ = the primitive N^{th} root of unity

Results are presented in the form of amplitude and phase spectra of the acceleration signal as a function of frequency. Fig. 4.11 provides an example of the typical results obtained from the acceleration spectra of two (2) ties during the train passage. Typical cross-tie acceleration spectra show a maximum in frequency range from 1 Hz to 2000 Hz, regardless of the support condition.

Fig. 4.11a shows the acceleration spectra of the instrumented voided cross-tie for Train A. The FFT analysis indicated there is clearly a dominant frequency at 59.4 Hz with an amplitude of 0.05g. While for the supported cross-tie, the strongest acceleration amplitude (0.02g) occurred at a frequency of 63.1 Hz, as shown in Fig. 4.11b. The shift in the peak dominant acceleration occurs towards the higher frequency spectra. This can be explained by the increased efficiency of the supported cross-tie in dissipating energy. When comparing both cross-tie responses, it can be noticed that the supported cross-tie is being excited at a lower amplitude and is dissipating acceleration energy. The higher the energy dissipation, the more dampened the response of the cross-tie, (i.e. more energy needs to be released to vibrate the cross-tie).



(a)

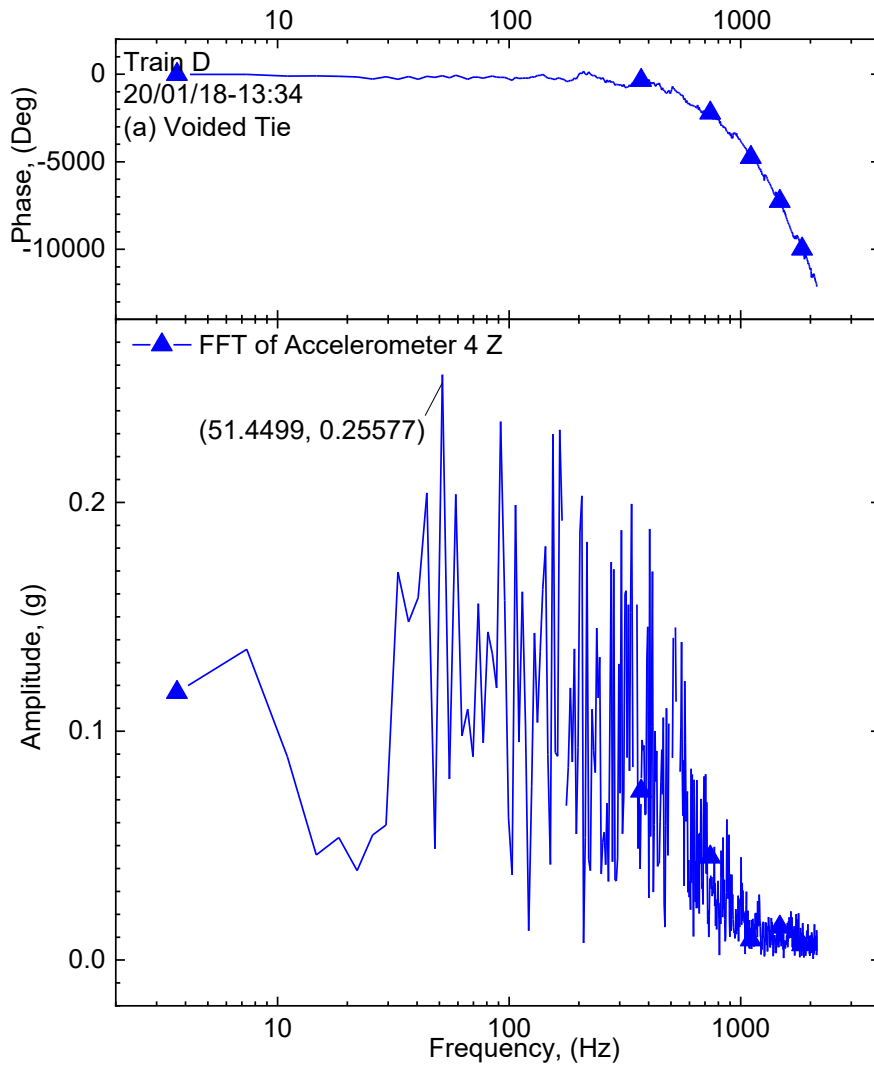


(b)

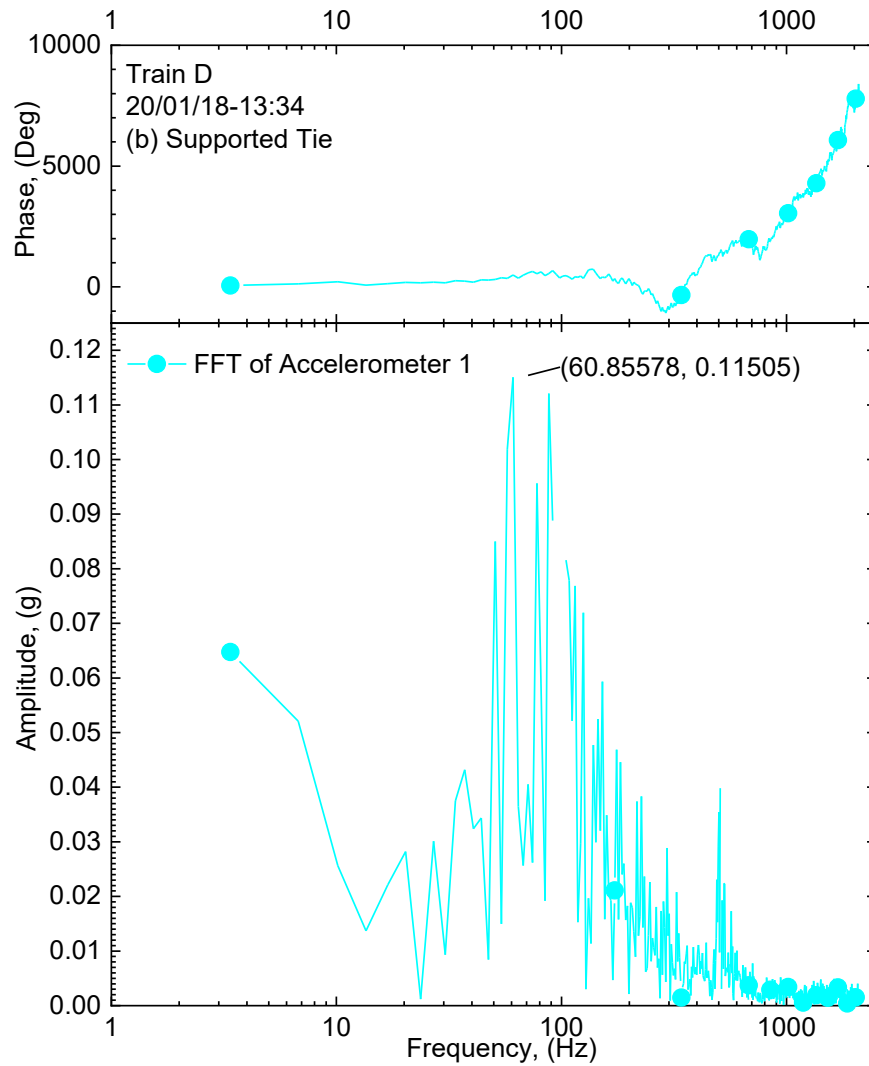
Fig. 4.11 FFT signal analysis of cross-tie acceleration for Train A crossing: (a) fouled segment, (b) clean segment

Fig. 4.12a presents the amplitude spectra and phase of the vertical acceleration of the voided cross-tie for Train D. The FFT analysis indicated there is a dominant frequency at 51.4 Hz with an amplitude of 0.25g. While for the supported cross-tie the high energy acceleration amplitude (0.11g) was observed at a frequency of 60.8 Hz, as shown in Fig. 4.12b. In comparison with acceleration of Train A, the dominant frequency of acceleration for the voided cross-tie has

shifted to a lower frequency. Similar behaviour was noticed for the supported cross-tie. The shift towards a lower frequency for both supported and voided ties is attributed to the significant reduction in the velocity of Train D when compared to Train A. Although the track is slightly stiffer in the case of Train D, the effect of change in stiffness was insignificant. Results show that as the velocity of the train decreases, the dominant frequency of acceleration shifts towards lower frequency range. This is explained by the fact that slower trains release less energy at lower acceleration amplitudes. The velocity of the train is directly proportional to the shift in the frequency range of both ties. However, supported ties have higher dominant frequency range than voided ties.



(a)



(b)

Fig. 4.12 FFT signal analysis of cross-tie acceleration for Train D crossing: (a) fouled segment, (b) clean segment

Figs. 4.13 and 4.14 present amplitude spectra and phase plots of the vertical acceleration of the instrumented cross-ties due to loading from Train B and Train C, respectively. The results presented in Figs. 4.13 and 4.14 reveal the effect of relatively high static track stiffness on the acceleration response of the voided and supported cross-tie as a function of frequency. For Train B, the FFT analysis indicated there is clearly a dominant frequency at 202.4 Hz with an

amplitude of 0.28g, as shown in Fig. 4.13a. While for the supported cross-tie, Fig. 4.13b shows that the high energy acceleration amplitude (0.08g) occurred at a frequency of 96.1 Hz. These results indicate that as the static track stiffness increases, there is a shift towards a higher range of dominant acceleration frequency for both voided and supported ties.

Fig. 4.14 displays the vibrational behaviour of the cross-ties as a function of frequency due to loading of Train C. The acceleration spectra of the voided cross-tie due to loading from Train C shown in Fig. 4.14a indicates there is a dominant frequency at 200.5 Hz with an amplitude of 0.38g. While for the supported cross-tie the strongest acceleration amplitude (0.06g) has been found to be at a frequency of 96.4 Hz, as shown in Fig. 4.14b. The results indicate that a reduction in static track stiffness, nevertheless, still considered to be high, would retain the dominant acceleration frequency of the supported cross-tie within the same range, and reduce the dominant acceleration frequency of the voided cross-tie to a lower value. A decrease in static track stiffness would have a major influence on the voided cross-tie and a minor influence on the supported cross-tie. This is because, the supported cross-tie is already characterized with high efficiency in energy dissipation. Meanwhile, the efficiency of the voided cross-tie would be critically impacted.

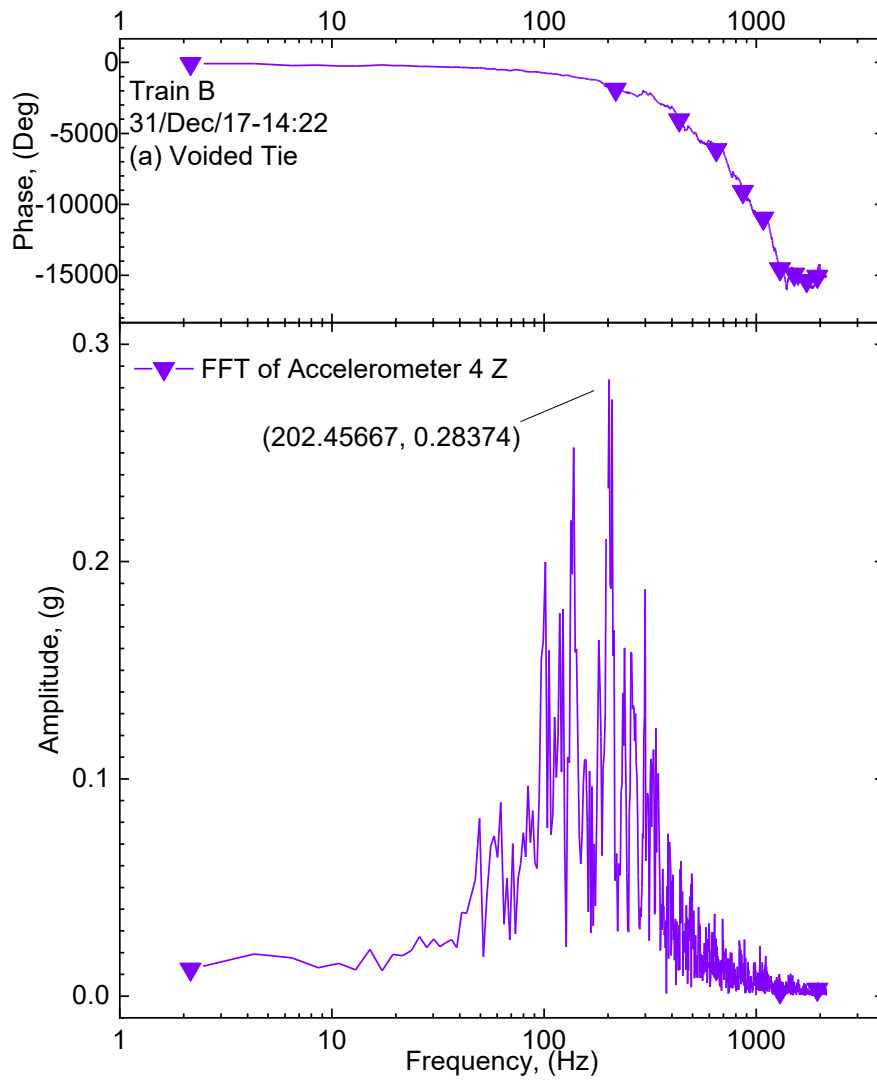
The FFT analysis of input data (i.e. acceleration time history) influences the phase results reported. This can be explained by the function of the FFT. In an FFT window, result bins are compared amongst each other in terms of the cosine and sine components (i.e. real and imaginary components). An unbalance between sine components (i.e. high component in one bin and low component in the other) produces negative phase data. Meanwhile, positive phase data signifies a consensus in terms of the compared bins (i.e. high component in one bin and high component in the other).

The FFT phase data can be observed for noise (i.e. arbitrary waveforms), which is indicative of errors in computed FFT results. In addition, FFT phase variations amongst the monitored trains can be examined to check for phase shifts between positive and negative phase angles which indicates resonance (i.e. a dominant high frequency acceleration component is due to bogie loading). This is because of impact wheel loading and sudden excitation of the cross-tie.

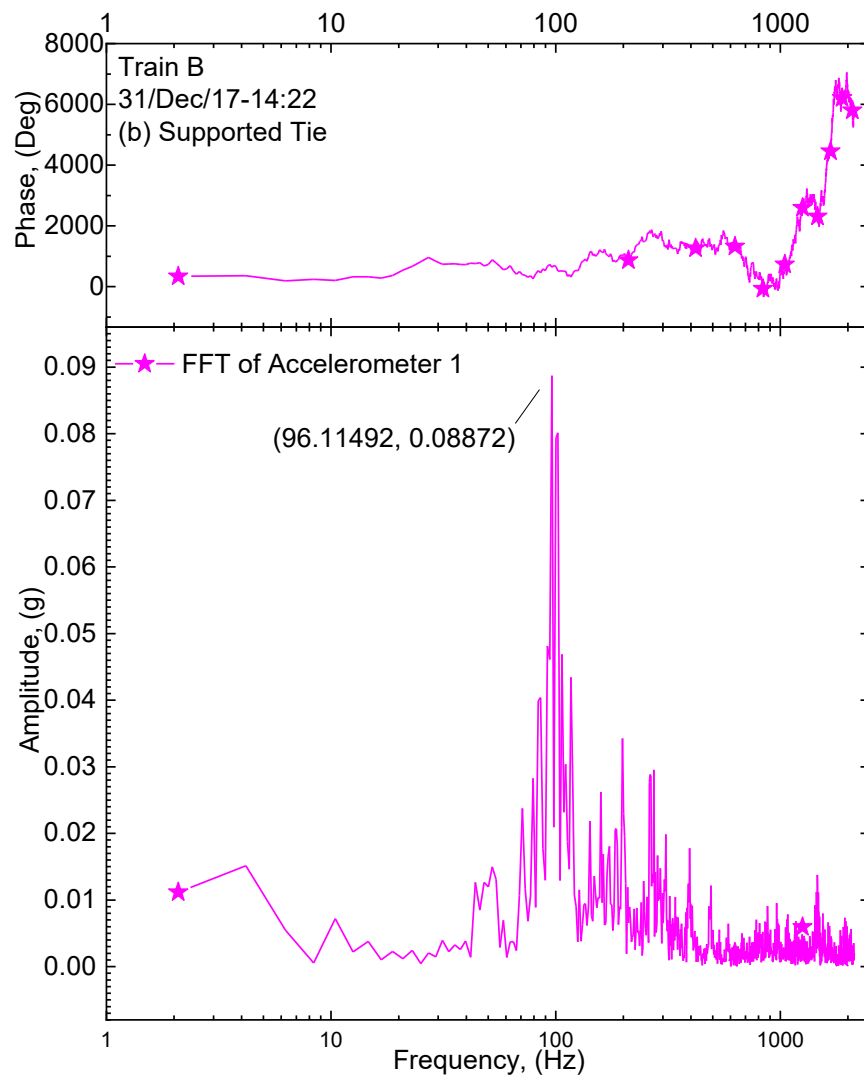
FFT phase results were in agreement with experimental test results presented by Aikawa (2018).

Figs. 4.15 present the vibrational behaviour of voided and supported cross-ties as a function of frequency due to the loading of Train E. The effect of train velocity is evident in the shift in the dominant frequency. The general trend observed in Fig. 4.15a shows the acceleration spectra of the instrumented voided cross-tie for Train E. The frequency content indicates there is a dominant frequency at 132.1 Hz with an amplitude of 0.26 g. While for the supported cross-tie the highest acceleration amplitude (0.12 g) is observed at a frequency of 62.7 Hz, as shown in Fig. 4.15b. These observations demonstrate that regardless of train velocity and static track stiffness, supported cross-ties have lower dominant acceleration amplitude and frequency than voided cross-ties. However, train velocity significantly influences the dominant acceleration of voided cross-ties, unlike supported cross-ties.

Fig. 4.16a shows the acceleration spectra of the instrumented voided cross-tie for Train F. FFT analysis indicated there is a dominant frequency at 150.1 Hz with an amplitude of 0.025g. While for the supported cross-tie the highest acceleration amplitude (0.020g) is observed at a frequency of 144.6 Hz, as shown in Fig. 4.16b. FFT results show that when train velocity increases and static track stiffness increases, as presented in Figs. 4.15 and 4.16, the peak dominant frequency increases and acceleration amplitude of dominant response decreases for voided and supported cross-ties. Nonetheless, supported cross-ties have lower dominant acceleration amplitude and frequency than voided cross-ties.

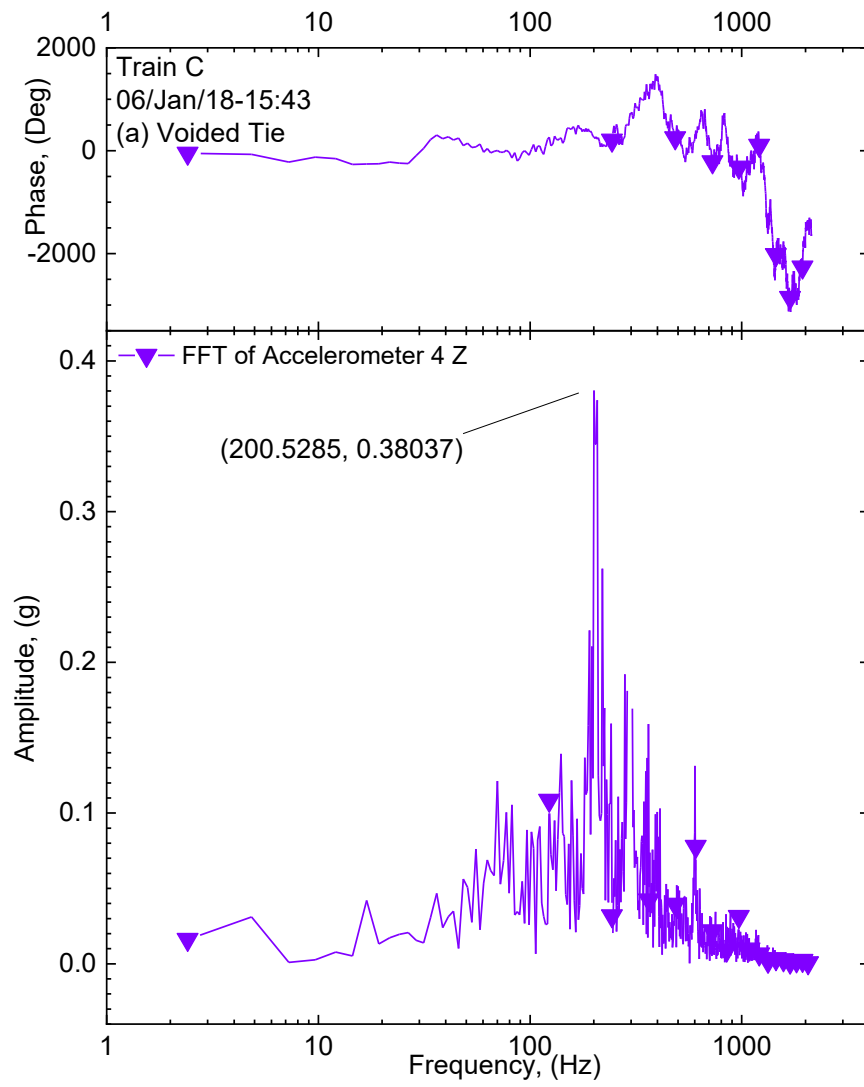


(a)

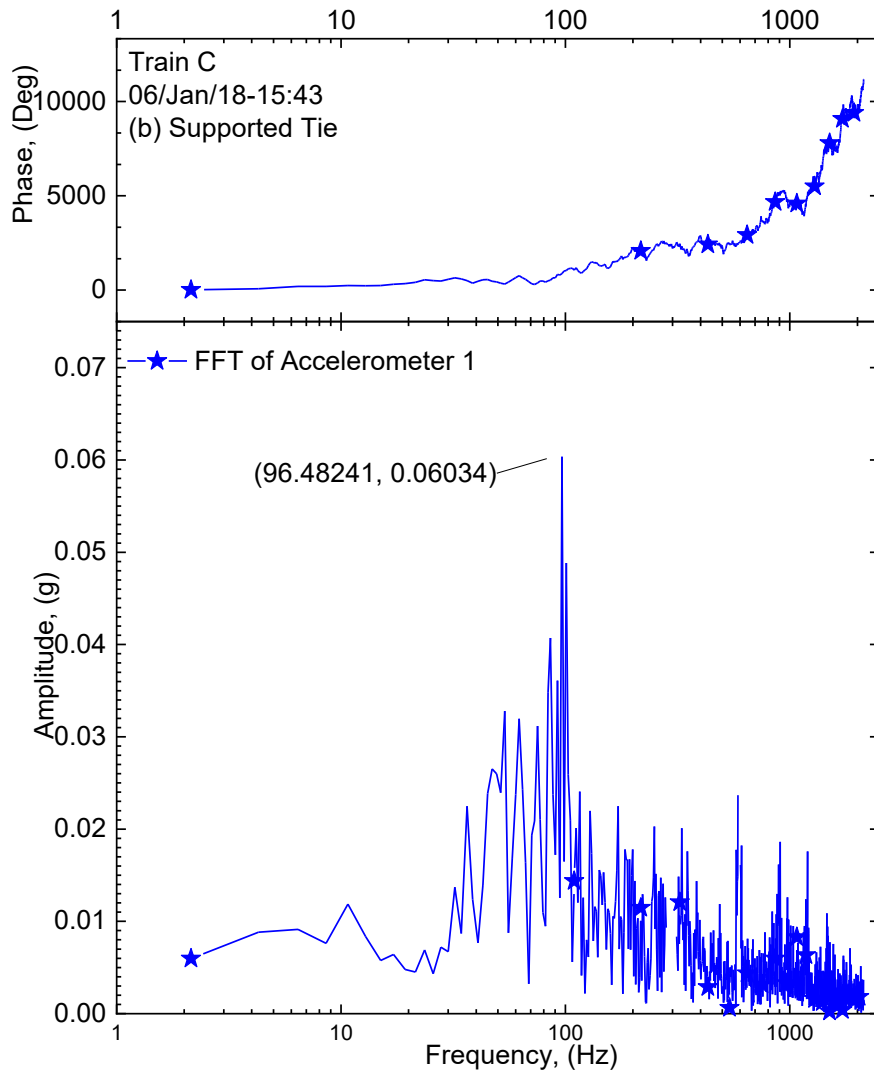


(b)

Fig. 4.13 FFT signal analysis of cross-tie acceleration for Train B crossing: (a) voided cross-tie (b), supported cross-tie

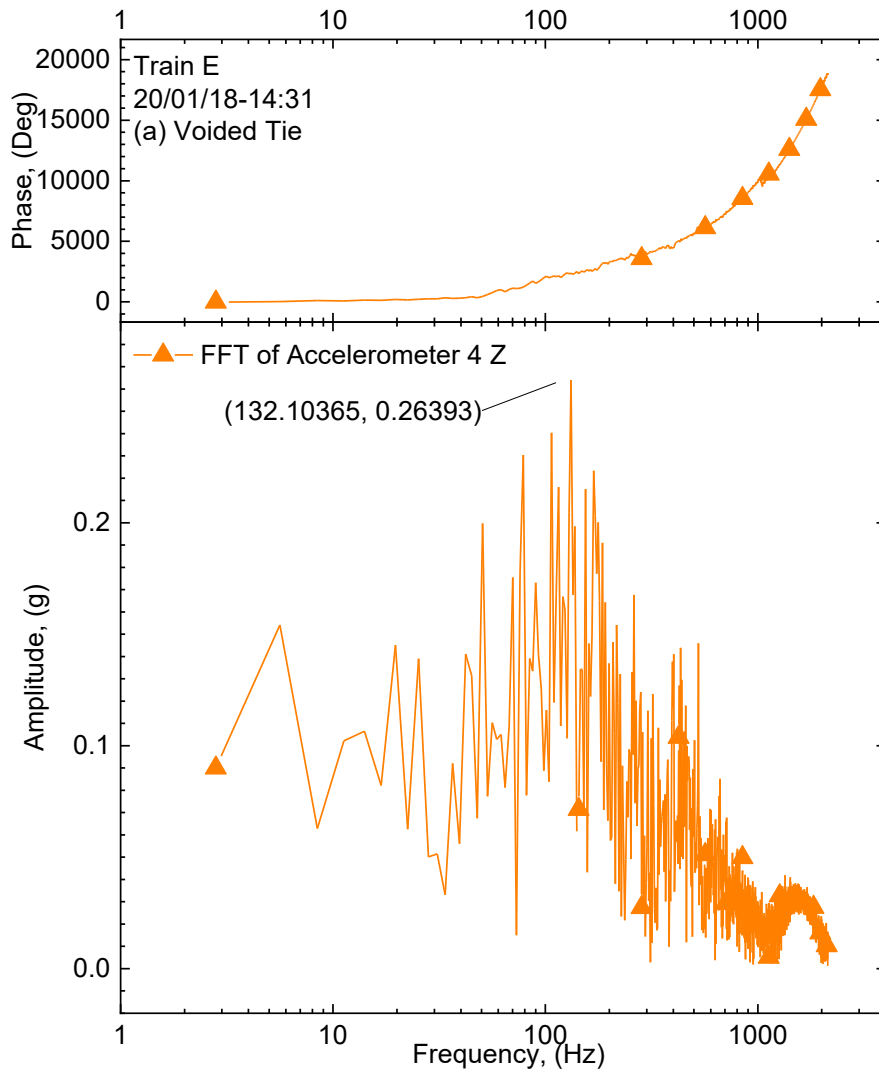


(a)

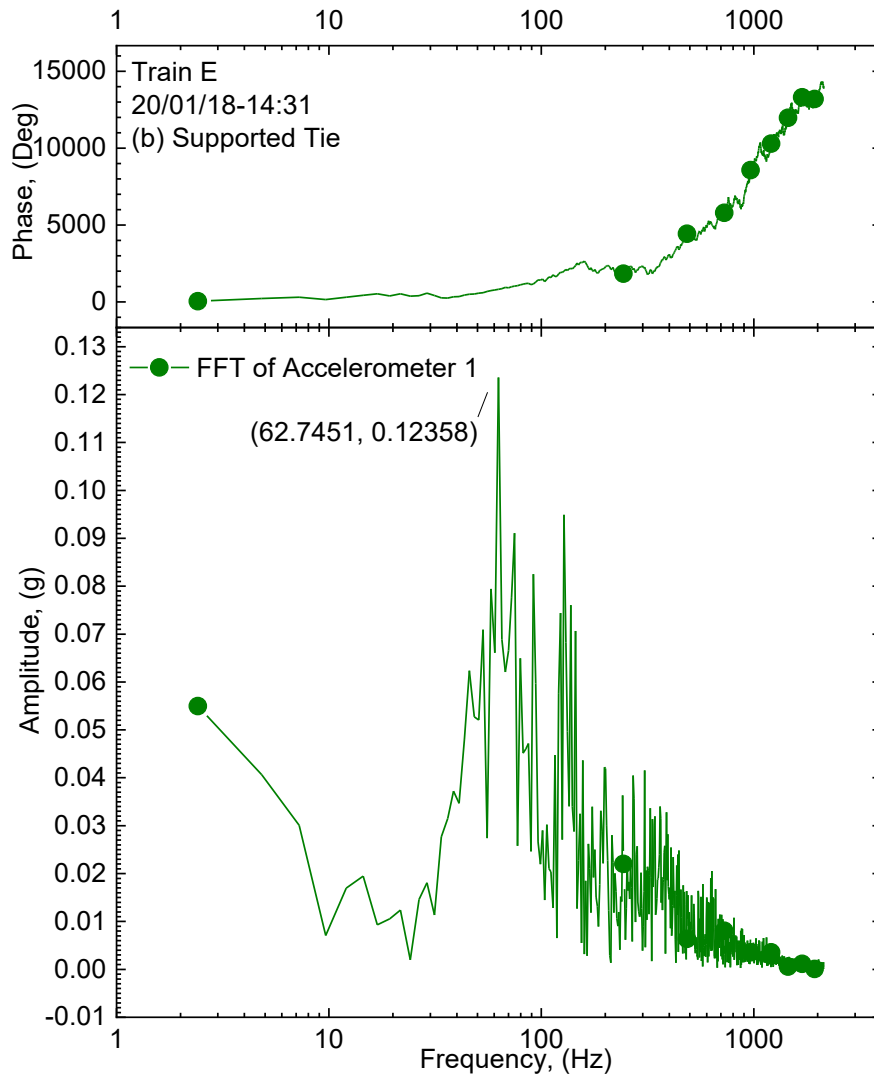


(b)

Fig. 4.14 FFT signal analysis of cross-tie acceleration for Train C crossing: (a) voided cross-tie, (b) supported cross-tie

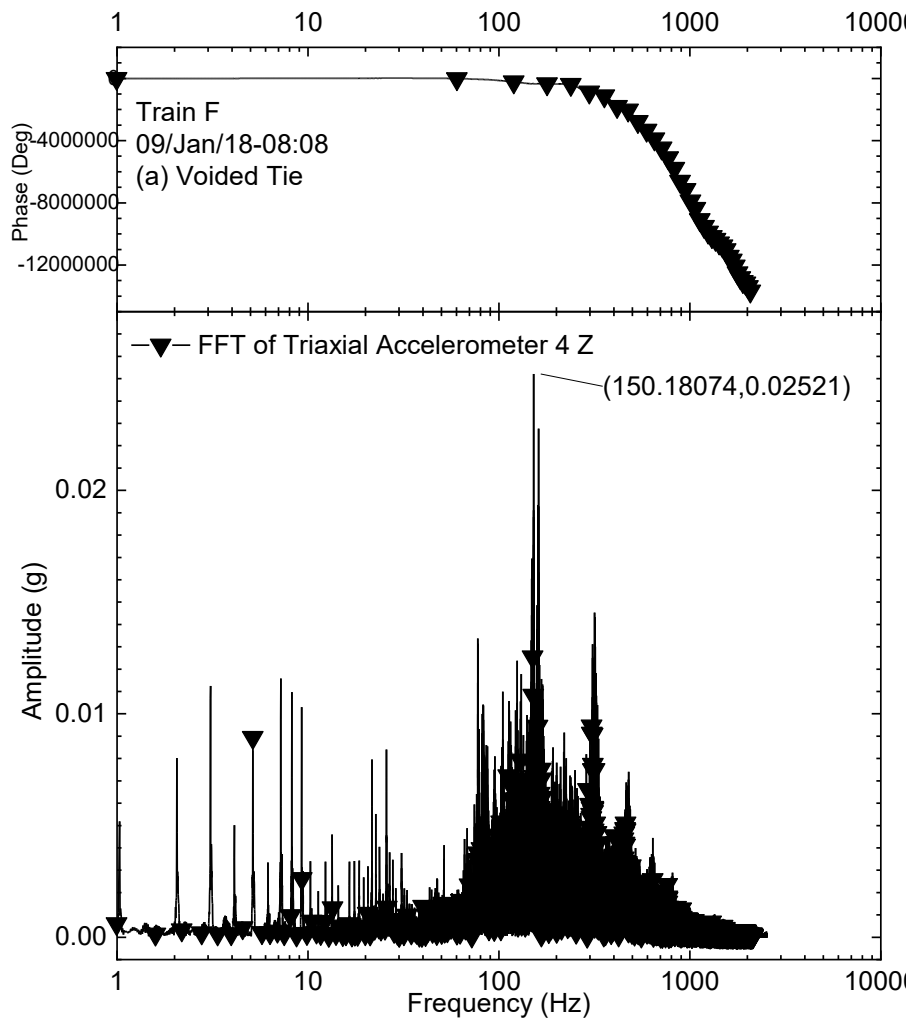


(a)

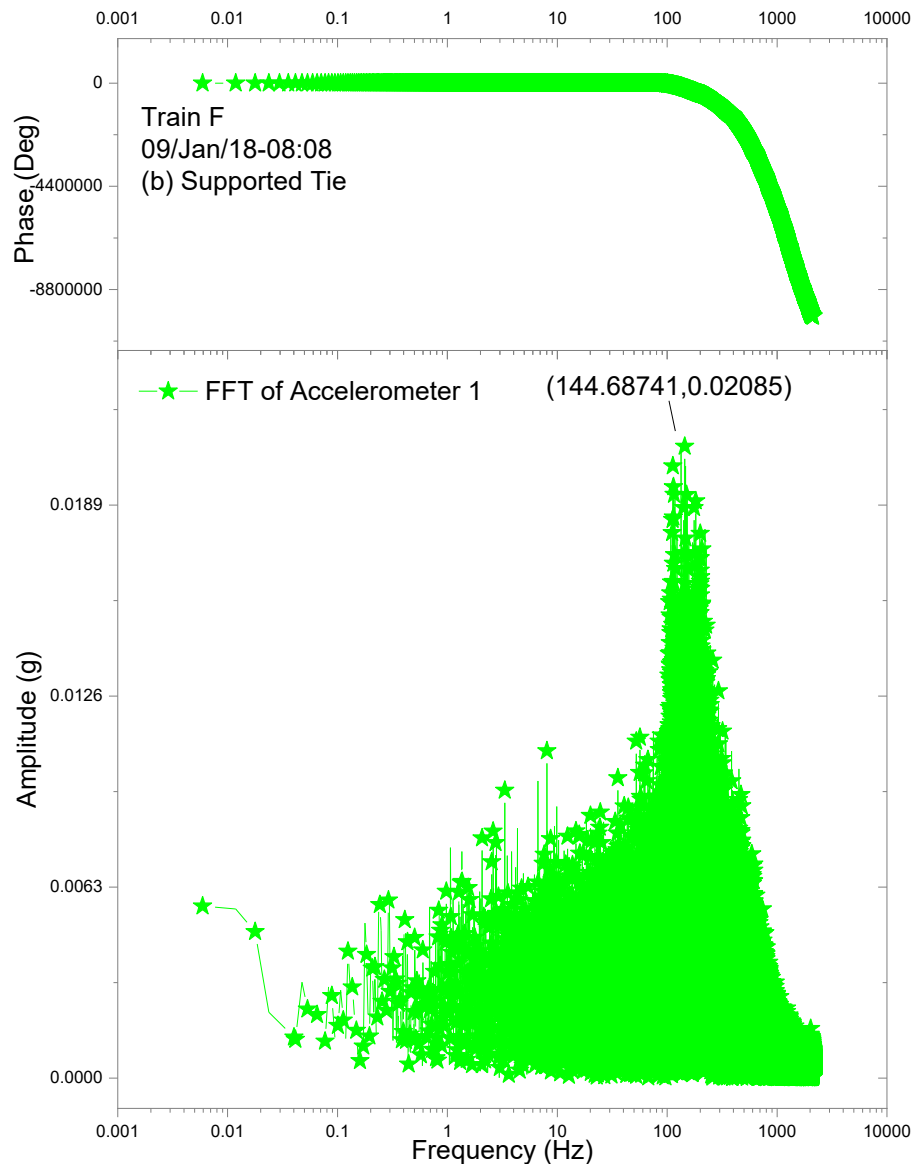


(b)

Fig. 4.15 FFT signal analysis of cross-tie acceleration for Train E cross: (a) voided cross-tie, (b) supported cross-tie



(a)



(b)

Fig. 4.16 FFT signal analysis of cross-tie acceleration for Train E cross: (a) voided cross-tie, (b) supported cross-tie

4.4 Factors Affecting Vertical Acceleration Response of Supported and Voided Cross-ties

4.4.1 Static Track Stiffness

The monitoring study presented in Chapter 3 reported static track stiffness results of 32 test trains using wayside instruments. The static track stiffness was estimated utilizing rail strain gauges to measure crib wheel loads and high-speed cameras to measure rail deflection. The results showed that during summertime (i.e. wet railroad conditions) the fouled railroad would have a relatively lower static track stiffness. Meanwhile, during wintertime (i.e. porewater in the ballast is frozen) the fine contaminated railroad is characterized relatively higher static track stiffness.

Fig. 4.17 shows the average acceleration response for the trains under study including locomotives and rolling stock data. In general, as the fouled static track stiffness (k) decreases below the typical static track stiffness range around 40 MN/m, the train induced vibrations are likely to increase at the fouled segment. For typical track conditions, within the same velocity range 70-90 km/h, the vertical acceleration was within the ± 3.0 g. The average acceleration magnitude for the supported cross-ties is ± 3.0 g compared to a much higher mean magnitudes recorded for voided cross-ties. This is explained in part by the good support conditions of the well supported cross-ties that is demonstrated in terms good cross-tie-ballast interface. Thus, making well-supported cross-ties more efficient dampers. Voided cross-ties are more sensitive to speed, given that track conditions are far from ideal; therefore, causing them to have higher vibrational response. The optimum static track stiffness provides adequate support for the cross-ties, whilst maintains the elastic the behaviour of the support system, where more energy is dissipated as may be noticed in Fig. 4.17. A stiff track, (i.e. $k \geq 51$) would have no voids present in between the ballast particles. The voids are filled with fine material and trapped pore water. Increased fine contamination and moisture content at sub-zero ambient temperature would cause the behaviour of the ballasted substructure behavior like the slab track (ballastless substructure). That is mainly due to the increase in the number of contact points and the contact force chain developed between the load bearing ballast particles and contaminating fines (Indraratna et al., 2014). The increase in the number of contact points and the contact force

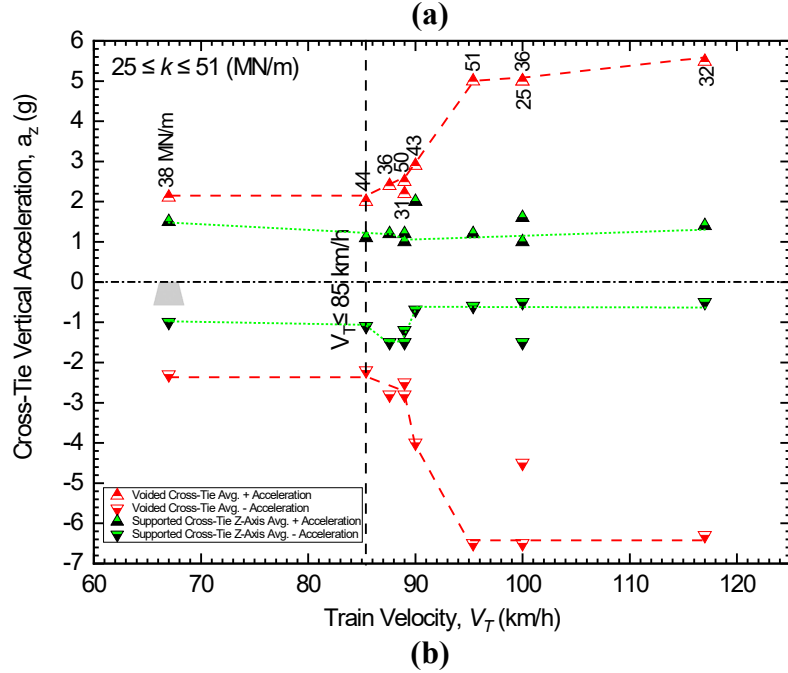
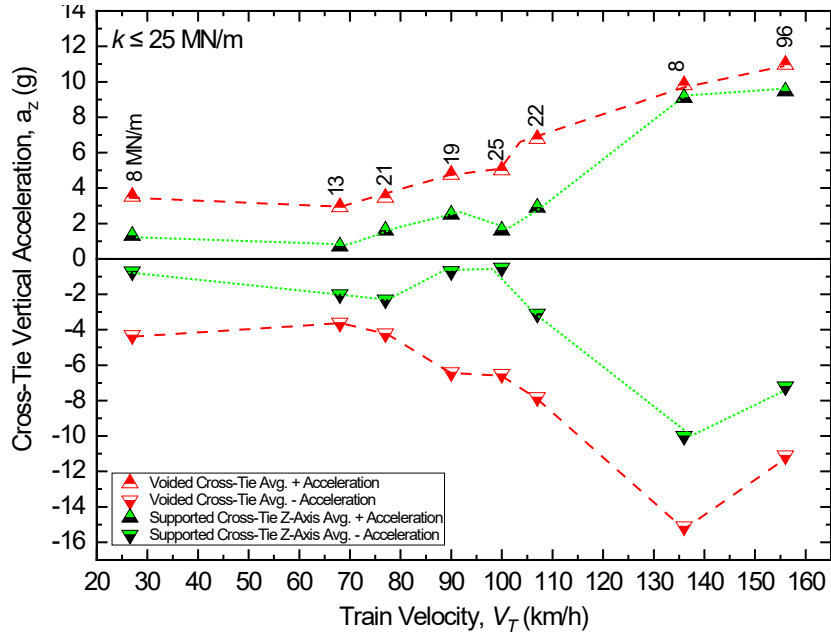
4.4.2 Train Velocity

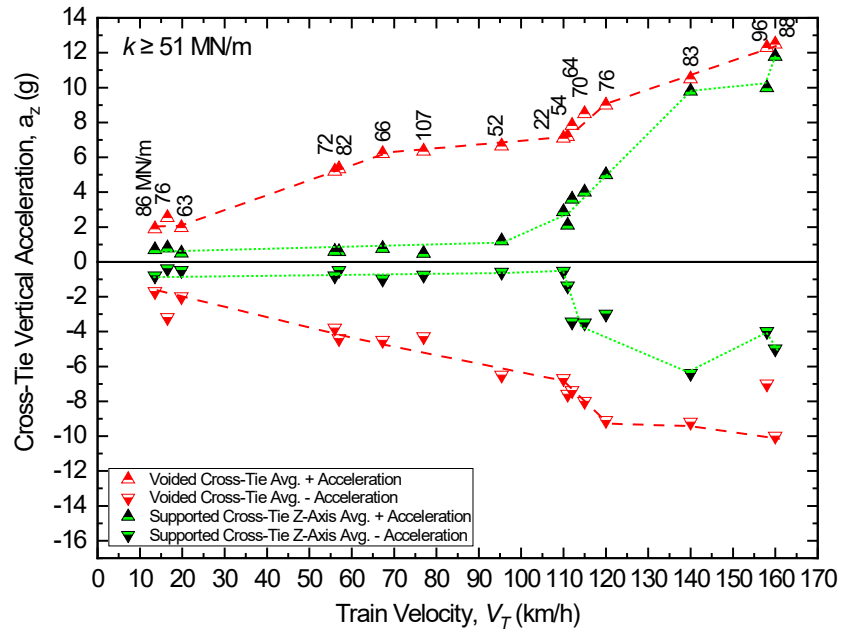
Figs. 4.18 present the measured locomotives and rolling stock acceleration data for supported and voided cross-ties at different train velocities. As the train velocity increases, the train induced vibrations increased at the instrumented segment; however, the magnitude of the excitation of the voided cross-tie was higher than the supported cross-tie. This may be explained by the lack of fines-contaminated voids present in between the ballast particles of the well supported cross-tie. Increased fines-contamination and moisture content at sub-zero ambient temperature would cause the response of the ballasted substructure to behave like a slab track (ballastless substructure). That is mainly due to the reduced damping performance of the ballasted track.

Fig. 4.18a presents the influence of train velocity on the vibrational response of the supported and voided cross-ties for soft track, (i.e. $k \leq 25$ MN/m). The results show that for train velocity $V_T \geq 100$ km/h the magnitude downward acceleration of the cross-ties is higher than the upward acceleration. This is explained in part by the effect of the pumped viscous fine-rich sub-grade cushioning the cross-tie and dampening vertical deflection. Data also suggested that for train velocities $V_T \leq 70$ km/h, there is no change in the upward vertical acceleration of the voided cross-tie, (i.e. no change in the vibrational response in the Z-direction).

Fig. 4.18b shows the effect of train velocity on the vibrational response of the supported and voided cross-ties for typical static track stiffness range (i.e. $25 \leq k \leq 51$ MN/m). The results show that for train velocity $V_T \geq 90$ km/h the magnitude downward acceleration of the cross-ties was higher than the upward acceleration. In addition, the data indicates that for train velocities $V_T \leq 85$ km/h, the response of the voided cross-tie in terms of vertical acceleration plateaued, (i.e. no change in the vibrational response in the Z-direction as velocity changed). Fig. 4.18c illustrates the influence of train velocity on the vibrational response of the supported and voided cross-ties for rigid track, i.e. $k \geq 51$ MN/m. The results indicated that for the voided cross-tie and train velocity $V_T \geq 20$ km/h, the vertical acceleration of the voided cross-tie increased drastically. Meanwhile, for the supported cross-tie, there was no change in the vibrational response in the Z-direction for train velocities under 100 km/h. The results showed

that regardless of train velocity the magnitude of downward and upward acceleration of the cross-ties was comparable. Additionally, for the voided cross-tie, the results indicated that for train velocity $V_T \geq 20$ km/h the vertical acceleration, increased drastically due to the absence of voids within the ballast. Air voids within the ballasts act as dampeners that absorbs and disperses vibrations. Meanwhile, for the supported cross-tie, there was no change in the vibrational response in the Z-direction for train velocities under 100 km/h.





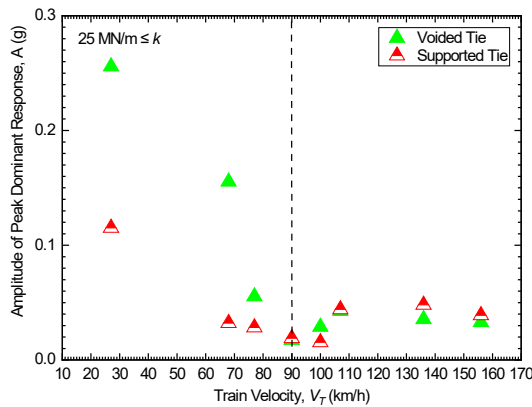
(c)

Fig. 4.18 Acceleration response of supported and voided cross-ties at different train velocities for: (a) $k \leq 25$ MN/m, (b) $25 \text{ MN/m} \leq k \leq 51 \text{ MN/m}$, (c) $k \geq 51 \text{ MN/m}$

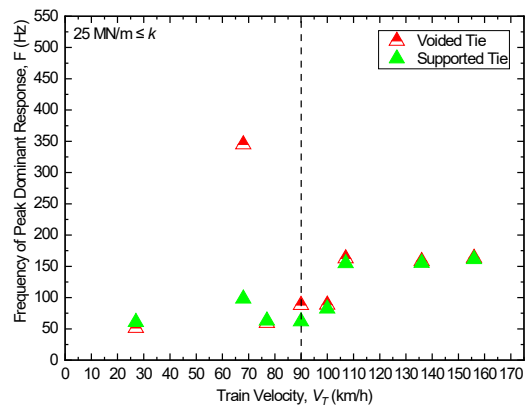
Fig. 4.19 presents the peak amplitude and its frequency for supported and voided cross-ties locomotives and rolling stock acceleration data. Fig. 4.19a demonstrates that as the static track stiffness decreased (i.e. $k \leq 25 \text{ MN/m}$) the peak Fourier amplitude for the supported cross-ties was higher (0.25 g) than the voided cross-ties for $V_T < 90 \text{ km/h}$. However, at higher velocities the amplitude of the sinusoid decreased to magnitudes equivalent to voided cross-ties (0.03 g). At lower velocities, the performance of the voided cross-ties may be considered better than supported cross-ties. This may be explained by the damping effect the sludge and water surrounding the voided cross-ties that may dampen the response of the cross-tie. Performance of the supported cross-tie was found to be improving at higher train velocities. This is explained by the densification process the train induces in the railroad sub-structure. As static track stiffness decreases, the frequency of the peak dominant response of voided cross-ties matches that of supported cross-ties except for $V_T \approx 70 \text{ km/h} - 90 \text{ km/h}$. Results demonstrate a critical

velocity range $V_T \approx 70$ km/h - 90 where frequency of peak dominant response is higher for voided cross-ties as shown in Fig. 4.19b. However, typical static track stiffness (i.e. $25 \text{ MN/m} \leq k \leq 51 \text{ MN/m}$) demonstrated optimum track performance $V_T < 90$ km/h, exemplified in low amplitude of peak response. However, frequency component of peak response is considered to be high compared to lower static track stiffness. This can be explained in the superior dynamic properties of clean ballast. Although, the vibration frequencies were higher, energy dissipation is optimal. Energy is dissipated more efficiently for supported cross-ties especially around critical velocity $V_T \approx 90$ km/h. At critical velocity voided cross-ties performed sub-optimally.

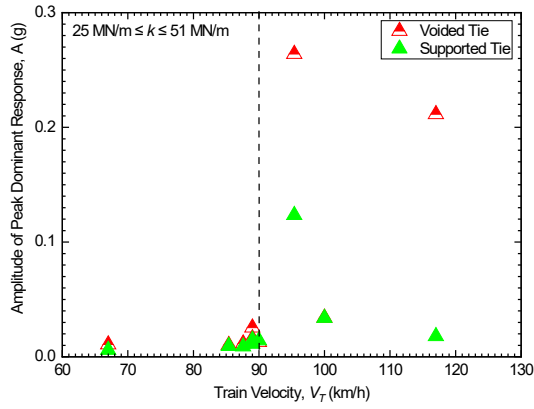
Sub-optimal energy dissipation of voided cross-ties cause the poorly supported cross-tie to vibrate at higher amplitude and higher frequency, as shown in Figs 4.19c and 4.19d, respectively. As the static track stiffness becomes very rigid, regardless of train velocity and support condition, the amplitude of the peak response is low ($A \approx 0.05$ g). Figs. 4.19e and 4.19f show that as the static track stiffness increases the cross-ties perform optimally regardless of the state of fouling and train velocity. This can be explained by the relatively low amplitude of the peak response (high energy dissipation), as shown in Fig. 4.19e, and high frequency response (high track vibrations) presented in Fig 4.19f.



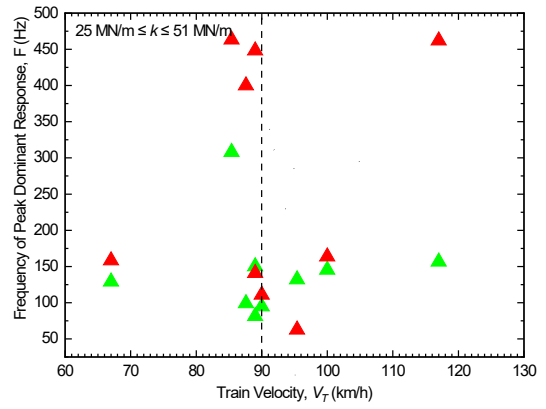
(a)



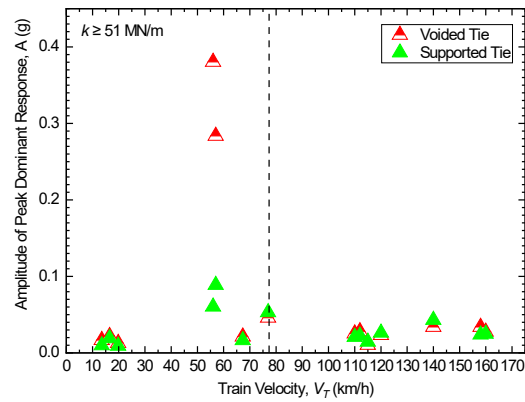
(b)



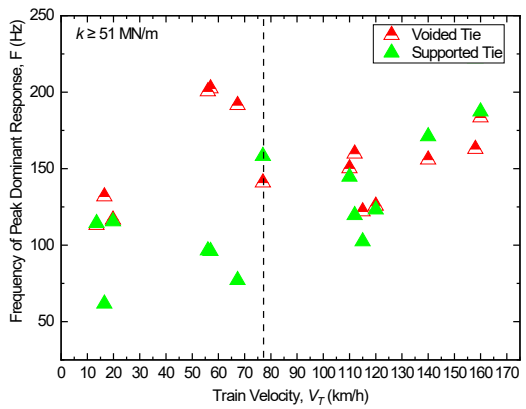
(c)



(d)



(e)



(f)

Fig. 4.19 Amplitude and frequency of peak dominant acceleration response of supported and voided cross-ties at different train velocities for: (a-b) $k \leq 25$ MN/m, (c-d) $25 \leq k \leq 51$ MN/m, (e-f) $k \geq 51$ MN/m

4.5 Summary

Cross-tie acceleration in the fouled segment due to train applied cyclic wheel load showed that the pattern and amplitude of the acceleration signal depends on train and track support associated parameters. In general, measured accelerations from different accelerometers in the fouled segment were close in terms of their amplitudes. The acceleration amplitudes measured in both directions (\pm) of Z-axis were higher for the fouled segment. The vibrational behaviour of concrete cross-ties in terms of magnitude and spectral distribution depends on the fouling state of the ballast and train velocity. For the fouled segment, although favorable environmental conditions resulted in an improved performance in terms of track deflection, the vibrational response increased. For stiff track, the vibration signature for each wheel was distinctive, i.e. fewer number of noise vibrational peaks produced for each wheel.

In general, as the train velocity increases, and the static track stiffness increases, the train induced vibrations are likely to increase at the fouled segment. However, results show that for train velocity $V_{Train} \leq 70.0$ km/h, the effect of train velocity for well supported ties is trivial in terms of the maximum measured acceleration magnitude in the in the vertical direction. For trains operating at a velocity $V_{Train} \leq 70.0$ km/h, the highest measured acceleration for supported ties $a_z = \pm 1.0$ g. Generally, results showed that regardless of train speed, static track stiffness, and wheel loading, the amplitude of the acceleration signal in the Z-axis is practically equivalent in magnitude for both directions (upwards and downwards).

FFT analysis indicated that as the static track stiffness decreases (i.e. $k \leq 25$ MN/m) the amplitude of the sinusoid for supported cross-ties is higher (0.25 g) than voided cross-ties for $V_T < 90$ km/h. However, at higher velocities the amplitude of the sinusoid decrease to magnitudes equivalent to voided cross-ties (0.03 g). Results demonstrate a critical velocity range $V_T \approx 70$ km/h – 90 km/h where frequency of peak dominant reponse is higher for voided cross-ties. Typical static track stiffness (i.e. 25 MN/m $\leq k \leq 51$ MN/m) demonstrated optimum track performance $V_T < 90$ km/h, exemplified in low amplitude of peak response. As the static track stiffness increases the cross-ties perform optimally regardless of the state of fouling and

train velocity. This can be explained by the relatively low amplitude of the peak response (high energy dissipation) and high frequency response (high cross-tie vibrations).

Unlike fully supported cross-tie, the vibrational response of the voided cross-tie varied with cross-tie support conditions. This is mainly because of the key role static track stiffness (k) plays in influencing the support conditions of the voided cross-tie. To avoid excessive train-induced vibrations (i.e. above the vibration level of the supported cross-ties) when crossing through fouled track segments, operators can use the empirical data presented in the current study as a general guideline to reduce vibrations from the source, i.e. the track:

(i) When crossing through soft to typical static track stiffness i.e. $k \leq 51$ MN/m, or during summer/spring seasons, the train velocity should be less than 70 km/h, so that the vertical acceleration of voided cross-ties remains below $\pm 3.0g$ (i.e. acceleration level of supported cross-ties for typical track stiffness range).

(ii) When traversing stiff track, i.e. $k \geq 51$ MN/m, or during fall/winter seasons, the train velocity should be less than 20 km/h so that the vertical acceleration of voided cross-ties remains below $\pm 3.0g$ (i.e. acceleration level of supported cross-ties for typical track stiffness range).

(iii) Further studies are required to enable deducing train velocity thresholds to minimize cross-tie vibrations and attenuation distance from the track.

Chapter 5

5 Numerical Modelling of cyclically-induced track suction and excess pore water pressure in ballasted tracks

5.1 General

Fouled railroads are beset with infiltrating fines contaminating the ballast, hindering drainage, and compromising its performance. Several failure incidents have been attributed to mud pumping and liquefaction, where fines from the saturated sub-grade, migrate upwards into the railroad substructure. Shallow or near surface water table is particularly problematic to ballasted railroads, especially when the native soil onto which the railroad is laid upon contains fine sized materials such as clays or silts. Mud pumping phenomenon is initiated in the railroad substructure (i.e., ballast, sub-ballast, and sub-grade). When saturated subgrade is subjected to short-term undrained cyclic loading, the pore-water pressure can accumulate causing fine particles to migrate upwards into the ballast layer. Moreover, the hydraulic gradient also plays a role in the transportation of fines. Under hydraulic flow internal erosion of subgrade takes place facilitated by pore pressure gradients in the railroad sub-structure.

Different theories are proposed in the literature for mud pumping mechanisms. For instance, Takatoshi (1997) attributed mud pumping to cyclic-induced suction. He categorised the phenomenon into four stages as shown in Fig. 5.1, and accordingly, proposed a suction-based mud pumping model. Cui et al. (2014) experimentally studied the fouled sub-ballast using embedded suction probe and found that the hydraulic conductivity of the interlayered track foundation is governed by the suction inside the fines, while the coarse elements being inert for the water transfer. Although the study provided valuable insights on the hydro-mechanical behavior of the fouled sub-ballast, it did not evaluate the suction in the fouled ballast. Wang et al. (2014) reviewed the state of the art and concluded that the main cause of mud pumping is confining and suction stresses; however, they did not elaborate on the quantification of confinement and suction stresses. Ebrahimi et al. (2015) performed laboratory tests on

contaminated ballast and reported that plastic strain for unsaturated fouled ballast with suction greater than 2000 kPa is same as that for clean ballast, regardless of fouling level and moisture content. They evaluated the soil water characteristic curves (SWCC) of the test materials, but only considered the suction induced by fines and water content, but not cyclic-induced suction. Yu et al. (2016) proposed a mathematical model based on the suction theory proposed by Takatoshi (1997). Their theoretical model introduced suction stress (σ_s) into 1D consolidation theory and established a relationship between critical hydraulic gradient (i_{cr}), constant applied load (P), time (t) and depth (z). However, their mathematical model cannot be extrapolated to train passby loading.

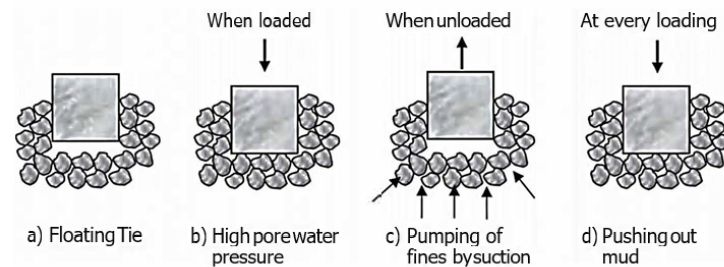


Fig. 5.1 Cyclic-induced suction-based mud pumping mechanism (Takatoshi, 1997)

Meanwhile, several studies suggested that cyclic-induced excess pore water pressure is the main cause for mud pumping. For example, Alobaidi and Hoare (1996); (1999) studied the pore water pressures generated near the top of the subgrade under static loading, using finite element modelling and static triaxial tests. They suggested that fines migration from subgrade is due to the development and dissipation of pore-water pressures at the interface between the subgrade and lower road layers. However, their study is not representative of cyclic-induced pore pressure because train passby loads change their amplitude with time, unlike static and quasi-static loads, and thus the results would not describe accurately the pore water pressures generated due to moving trains. Indraratna et al. (2009) investigated the effectiveness of prefabricated vertical drains in the dissipation of cyclic-induced excess pore water pressure when shear strain exceeds 1.5 – 2 %. However, their study was limited to laboratory testing. Duong et al. (2014) performed physical small scale model tests on a ballast layer overlying a

subgrade layer under different water content, loading and subgrade dry density conditions. The model was instrumented with moisture, pore water pressure, and axial displacement sensors. They found that the generation of pore water pressure in the subgrade is the major cause of migration of fine particles (i.e., mud pumping into the ballast) and creation of subgrade-sub-ballast interlayer. Duong et al. (2014) experimentally investigated the effect of effect of wetting–drying cycles on track foundation microstructure, and on hydraulic conductivity of fouled sub-ballast. However, they did not provide any insights on the role of cyclic loading in contaminating fines migration to the ballast.

Mekonnen (2019) analyzed the response of railroad track to train loading using finite element analysis. His results demonstrated that hydraulic conductivity, undrained elastic modulus and depth of embankment significantly affect the induced excess pore water pressure, while the effect of relative density is trivial. Although the study quantified the excess pore water generated, but the wheel loads were simulated as sinusoidal loads (i.e., constant amplitude and frequency), which do not reflect the in-situ cyclic loading conditions. Li et al. (2019) investigated the effects of highspeed trains travelling on slab track over saturated foundation. Their results demonstrated that maximum pore water pressure occurred at the track foundation surface and attenuated with depth. However, the study was limited to slab tracks and hence the results can not be extrapolated to ballasted tracks. Indraratna et al. (2020) discussed important results from large-scale undrained cyclic triaxial tests, and stated that soil plasticity, fines content, and the hydraulic gradient play a major role in pumping subgrade fines. However, their study only attributed the migration of fines to the presence of hydraulic gradient and increase in cyclic-induced excess pore water pressure. However, their study did not discuss the cyclic induced suction effect on the migration of fines to the surface of the ballast. In the same study, Indraratna et al. (2020) predicted rise in excess pore pressure 2.0 m below the subgrade and along the centre line of the track and discussed the role of prefabricated vertical drains (PVDs) in stabilizing the toe of the embankment. However, their study did not map the areas in which excess pore water pressure rise and did not comment on the role of suction in stabilising or destabilising the railroad embankment.

This literature review revealed that the suction component of excess pore water pressure (i.e., negative *PWP*) is seldom investigated because its stabilizing role is typically considered through effective stresses. The current study aims to address the gap in the current state of knowledge with regards to the quantification of the excess pore water pressure induced by cyclic loading and evaluating the suction component and its effect on the migration of fines in the ballast and sub-ballast. This study employed two-dimensional finite element (FE) models established using the PLAXIS 2D Dynamic (Brinkgreve et al., 2017) to quantify excess pore water pressure and map areas of maximum values due to measured train loading time histories. The load time history used in the analysis corresponded to the front locomotives of the rolling stock only to minimise the effect of load variation. The effect of shallow ground water level (GWL) on generated positive and negative excess pore water pressures was investigated. The details of the site sub-structure, super-structure, and train loading are presented in the preceding chapters.

5.2 Finite Element Model

The primary focus of the current study is on the behaviour of the substructure; therefore, two-dimensional dynamic analyses were conducted to allow consideration of ballast and foundation sub-structure while keeping the computational efforts accurate and efficient. Several calibrated 15-noded element types were developed based on the Parkville, MO instrumented site.

5.2.1 Geometry and Meshing

A typical railway track with rail and cross-ties resting on ballast and sub-ballast layers with different thicknesses was modelled. A 3.0 m x 6.0 m soil strata was modelled as silty clay loam subgrade, a 0.17 m sub-ballast layer was defined on top of the subgrade, and was overlain by a 0.48 m ballast layer (Jiang and Nimbalkar, 2019). Fig. 5.2 shows the dimensions of the railway. The cross-tie was modeled as a concrete model volume element (cluster), with assigned depth, width, and concrete properties. The concrete cluster was defined as a linearly elastic concrete model, with a non-porous behaviour, typical of modeled concrete structural elements. The concrete model is a superior elastoplastic model for concrete and shotcrete structures. Time-dependent stiffness and strength of concrete, strain hardening-softening behaviour in

compression and tension, in addition to creep and shrinkage, which can be modeled accurately. The failure criterion of the concrete model is governed by the Mohr-Coulomb yield surface, which is combined with a Rankine yield surface when tensile stresses are experienced by the structural element. The rail was modeled as a 5-node beam element with four pairs of stress points. A beam element was assigned with rail parameters (i.e. flexural rigidity/bending stiffness ' EI ' and axial stiffness ' EA '). Node to node connections were created to model rail clips attached to the cross-tie. Interface joint elements were assigned to the volume cluster (i.e. cross-tie) to properly model the soil-structure interaction. Interface joints simulated the shearing material at the contact between the cross-tie and the surrounding ballast.

Dynamic boundary conditions were defined by default to represent the far-field behaviour of the subgrade. Actually, track subgrade was characterised by an infinite domain which was reduced creating the geometry model. Therefore, viscous boundaries were defined along the boundary of the 3.0 m x 6.0 m track subgrade in the model to simulate the far-field behaviour. Viscous boundaries absorb increments of stresses caused by dynamic loading prevents spurious wave reflections inside the modeled subgrade polygon. Hydraulic boundary conditions in the model are assigned based on the general phreatic level defined at the ground surface. A robust triangulation principle (i.e. PLAXIS mesh generator created 32,245-15-nodal triangular elements) which was used to discretize the different layers and optimised triangles ensured finer distribution of nodes and hence accurate calculations. Fig. 5.3 shows the finite element mesh comprising the generated triangular elements. A finer mesh configuration caused unfeasible calculation times. Therefore, the degree of mesh refinement used in the current study matched a relevant study by Jiang and Nimbalkar (2019).

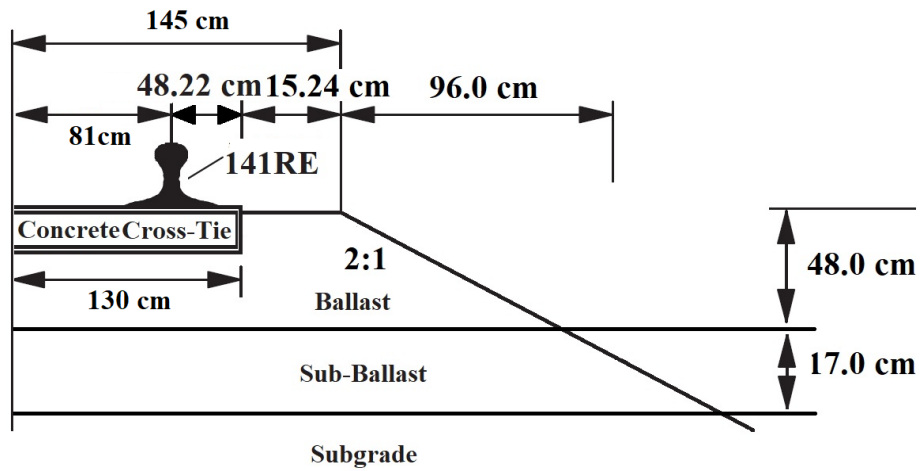


Fig. 5.2 Cross-section of constructed plane-strain model

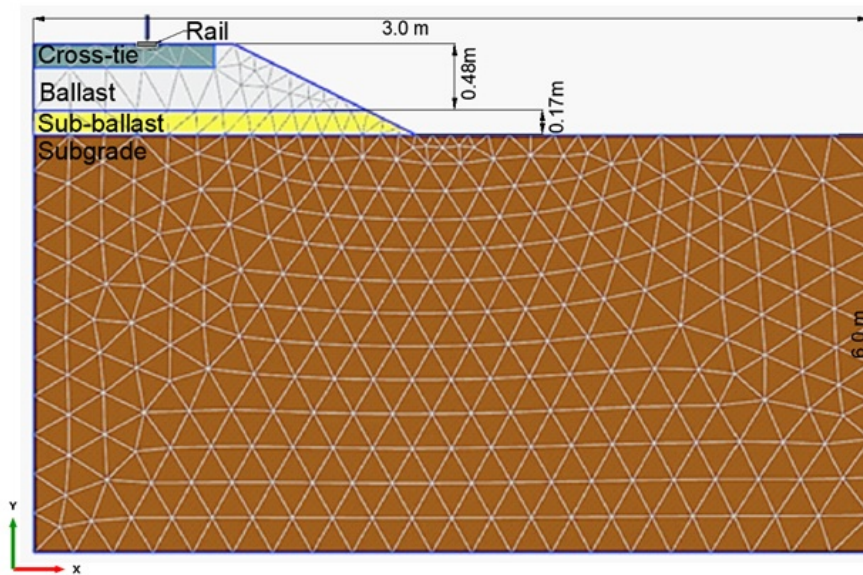


Fig. 5.3 Typical medium element distribution mesh

5.2.2 Defining elements and materials

The different soil layers (sub-grade, ballast and sub-ballast) behaviour was simulated as linear elastic-perfectly plastic material with Mohr-Coulomb failure criterion (Tvrdek, 2015;

Indraratna et al., 2020). Meanwhile, the behaviour of the superstructure components (i.e. rail and cross-tie) was simulated as linear elastic material. The Mohr–Coulomb failure envelope curve is governed by *Equation 5.1*, i.e.:

$$|\tau| = c + \sigma_n \tan \phi \dots \dots \dots \text{Equation 5.1}$$

Where,

τ = shear strength

σ_n = normal stress

ϕ = angle of internal friction

Material parameters and constitutive models employed in the numerical simulation are listed in Table 5.1 (Indraratna et al., 2012). Ballast, sub-ballast and subgrade were modeled using the Mohr-Coulomb soil model, which is suitable to describe the behavior of a ballast under wheel loading (Noorzai et al., 2012). The railroad superstructure components (i.e. rail and cross-tie) were modeled as linear elastic materials with properties presented in Table 5.2 (Jiang and Nimbalkar, 2019). Further laboratory testing is required to capture the dynamic properties of the modelled materials and use them in the model to mimic superstructure and substructure response. The Van Genuchten (1980) function was utilised to model the transient groundwater flow in the unsaturated track foundation (Tvrdek, 2015). It was utilised to estimate the soil water retention curve (SWRC) from which unsaturated hydraulic conductivity can be calculated, i.e.,

$$K_r = \Theta^{0.5} \left[\frac{\int_0^\Theta \frac{1}{h(x)} dx}{\int_0^1 \frac{1}{h(x)} dx} \right] \dots \dots \dots \text{Equation 5.2}$$

Where,

h = pressure head a function of normalized water content (Θ) (Van Genuchten, 1980)

$$\Theta \text{ (normalized water content)} = \frac{\theta - \theta_r}{\theta_s - \theta_r}$$

θ = volumetric water content

θ_r = residual water content

θ_s = saturated water content

In all modeled cases, the phreatic level was set at the ground surface (i.e. at elevation 0.0 m), since it represents the worst-case scenario. The steady state pore water pressures are generated according to the water conditions of each layer. Excess pore water pressures are calculated as a result of undrained track foundation behaviour. Therefore, drainage type is set to “undrained” to simulate the behaviour of high-water retention capacity of fouled ballast.

Table 5.1 Sub-structure input parameters

Parameters	Units	Substructure			
		Ballast	Sub-ballast	Subgrade	
Symbol	Model	Mohr-Coulomb	Mohr-Coulomb	Mohr-Coulomb	
E	Elasticity modulus	kPa	21,340	80,000	70,000
γ_{Dry}	Dry unit weight	kN/m ³	15.6	16.7	18.0
γ_{sat}	Saturated Unit Weight	kN/m ³	17.0	18.0	20.0
C'	Effective cohesion	kPa	0.0	0.0	1.0
ϕ'	Effective friction angle	°	58.47	35.0	25.0
ψ'	Dilatancy angle	°	12.95	0.0	0.0
p_{ref}	Reference confining pressure	kPa	50.0	-	-
	GW Model		Standard	Standard	Van Genuchten
	Type		Coarse	Coarse	Silty Clay Loam

Table 5.2 Super-structure input parameters

Parameters	Units	Superstructure		
		Rail	Concrete Cross-tie	
Symbol	Model	Linear Elastic	Linear Elastic	
E	Elasticity modulus	kPa	21,000,000	10,000,000

5.2.3 Model Calibration

Initially, a set of input parameters were selected based on the laboratory tests conducted by the author as part of this thesis (Indraratna et al., 2012; Touqan et al., 2020) and Chapter 2 in addition to field trials (Chapter 3) and from the literature (Indraratna, Nimbalkar et al. 2012). Using the initial input parameters, the superstructure deformation response was calculated, and the rail deflection vs time was plotted. An iterative process of fine-tuning input parameters (i.e. elastic modulus of sub-structure) so that the calculated maximum transient deflection was close to the measured transient response.

The numerical model was validated by assessing the output results with measured experimental deflection results obtained from wayside instruments. The deflection data from the high-speed cameras was processed using a MATLAB code where for each train consecutive frames were captured of the targets attached on the rail and compared with a benchmark height. The calibration of the high-speed cameras was performed during the installation, where the cameras captured the height of the deflection targets after the installation. The unloaded rail height was used as the benchmark height.

Fig. 5.4 compares the simulated transient time history deflection output free at a selected point node on the superstructure with the measured deflection employing the high-speed camera track readings. It is important to note that the phase shift shown in Fig. 5.4 is due to the trains having different speeds. The results presented in Fig. 5.4 demonstrate a good agreement between the calculated and measured responses, which validated the accuracy and reliability of the model.

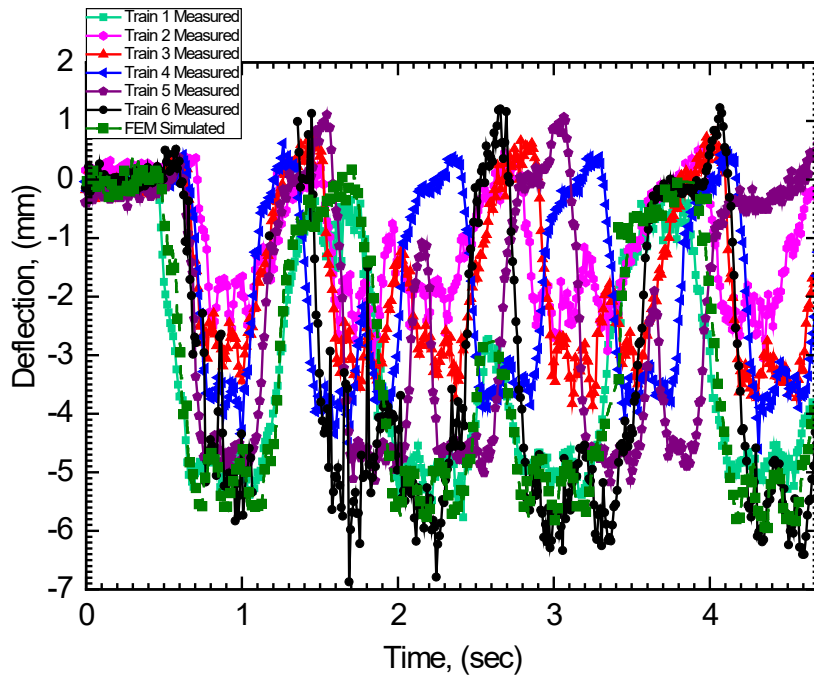


Fig. 5.4 Typical deflection output compared with measured track deflection

5.2.4 Input cyclic train passby loading

Train loading was applied as a dynamic point load time history on the rail. Typical load time history of the front locomotives shown in Fig. 5.5 was used as a dynamic multiplier. The loading data of six trains with varying velocities as presented in Table 5.3 were selected from a pool of 32 trains. It was imperative to opt for train data with corresponding static track stiffness (i.e. typical static track stiffness $25 \text{ MN/m} \leq k \leq 51 \text{ MN/m}$ for Trains 1-6) in order to minimize the effect track sub-structure stiffness may have on suction and generated porewater pressure. The governing equilibrium equation for time-dependent movement of a volume under the dynamic load is used, i.e.:

$$M\ddot{u} + C\dot{u} + Ku = F \dots \dots \dots \text{Equation 5.3}$$

where, M is the mass matrix, u is the displacement vector, C is the damping matrix, K is the stiffness matrix and F is the load vector. Displacement (u), velocity (\dot{u}), and acceleration (\ddot{u}), vary with time. To ensure realistic simulation of the fouled undrained track foundation (i.e.,

evaluating the generation and the dissipation of excess pore pressures), the dynamic response analysis incorporated the consolidation calculations.

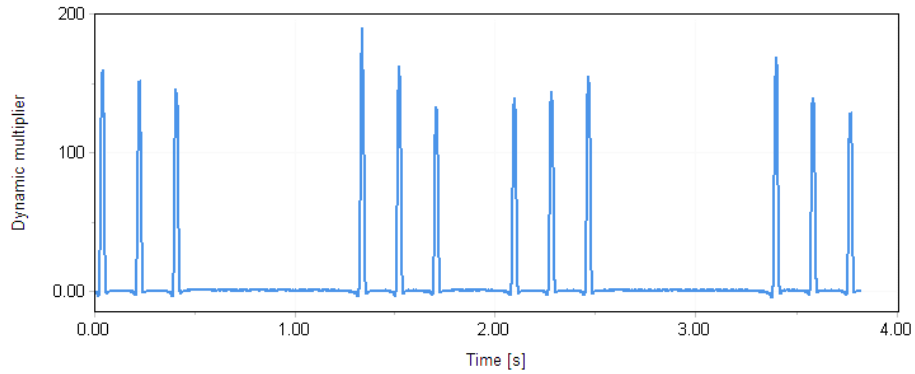


Fig. 5.5 Typical train loading time history used as applied point load

Table 5.3 Selected trains operational velocity at the time of crossing

Train ID	Date (dd/mmm/yy)	Time (hh:mm)	Train Velocity (km/h)
1	30/Dec/17	14:58	67.0
2	14/Feb/18	11:24	77.0
3	26/Jan/18	08:10	85.0
4	04/Feb/18	17:27	90.0
5	14/Mar/18	07:04	100.0
6	20/Jan/18	15:23	102.0

5.2.5 Analysis Stages

Simulation of the railroad was completed in 5 stages (Brinkgreve et al., 2017). To introduce the initial stresses in the field, an initial stage is performed to achieve the geostatic equilibrium, where initial vertical stresses that are in equilibrium with the self-weight of the track foundation stresses are generated by the K_0 procedure with active groundwater table (Singh and Seth, 2017). The K_0 procedure is a calculation method that considers the loading history of the soil at the time of definition of the initial stresses (Brinkgreve et al., 2017). K_0 procedure is ideal for Mohr–Coulomb soil model and for the conditions where the railroad surface is horizontal and the sub-structure layers are parallel to the surface. In this procedure, the coefficient of lateral earth pressure at rest, K_0 , is given by:

$$K_0 = 1 - \sin (\phi) \dots \dots \dots \text{Equation 5.4}$$

Where,

K_0 = coefficient of lateral earth pressure at rest

ϕ = soil friction angle

Stages 1-4 are consolidation phases, where the response calculation is time dependant. Very small-time steps (smaller than critical time steps) can result in stress oscillations. Therefore, PLAXIS uses a fully automated time stepping procedure that considers critical time step. Several staged construction procedures are found in literature. However, in the current study the procedure set for construction of a road embankment was followed (Brinkgreve et al., 2017). Phase 1 was created as a construction phase where the sub-ballast layer was activated, and a 1-day time interval was set. Phase 2 was defined as a consolidation phase where no changes in the geometry of the model were introduced. Phase 3 was specified as a construction phase of the ballast, similar to phase 1. Phase 4 was prescribed as a consolidation phase of the ballast layer. Phase 5 was set as dynamic loading with consolidation phase, where the applied dynamic point load was activated, and load-time history was applied as a dynamic multiplier.

5.2.6 Model limitations

In this study, the continuum model has been utilized. Air pressure is considered constant (i.e. excess air pressure and air compressibility are not considered). In the undrained analyses conducted herein, the water is undrained, but the pore air is always drained. Thus, the excess pore pressure was generated for the unsaturated track foundation and the suction effect was considered. Excess pore pressure is governed by the unsaturated bulk modulus of pore fluid, which considers water compressibility and soil-water retention curve. This fluid bulk modulus is usually much smaller than the bulk modulus of water. Soil-water retention curves for the track foundation are established using fouled track foundation grain size distribution (GSD). GSD of fouled track foundation under study can be found in Chapter 2 and Chapter 3.

5.3 Typical FEM Dynamic Simulation Results

The total stresses in the substructure were calculated using the developed numerical model. The total stresses (σ_{Total}) are comprised of effective stresses (σ'), and active pore pressures (P_{active}), shown in *Equation 5.5*. Active pore pressure is the product of PWP and effective saturation ($S_{effective}$) (i.e. degree of saturation). The effective saturation is utilized as the Bishop coefficient in the definition of Bishop effective stress which is also used to calculate the weight of soil. Bishop's definition of effective stress and includes suction (i.e. negative pore stress) and the degree of saturation in the calculation.

$$\sigma_{Total} = \sigma' + P_{active} \dots\dots\dots \textbf{Equation 5.5}$$

Where,

$$P_{active} = S_{effective} \times PWP$$

$$PWP = P_{steady} + P_{excess}$$

In unsaturated ballast conditions, *PWP* differs from active pore pressure. Excess pore water pressures develop due to stress changes associated with loading-unloading-reloading of the undrained ballast. Moreover, stress changes are influenced by the deformation in the

substructure, which can be triggered by change in loading, hydraulic, and consolidation conditions. Therefore, it was imperative to achieve accurate PWP_{excess} calculations to calibrate the numerical model using measured deflection data. Fig. 5.6 maps the total vertical displacements (U_y) in the y-direction. Results show that the maximum vertical displacement occurred around the cross-tie and on top of the ballast ($U_y = -5.6$ mm). While the ground surface experienced upward movement of soil ($U_y = 1.6$ mm), (i.e. heave a typical behaviour of silty granular subgrade under surcharge loading). Fig. 5.7 maps the total horizontal displacements (U_x) in the x-direction. Results show that the maximum horizontal displacement occurred the toe of the railroad embankment $U_x = -15.0$ mm.

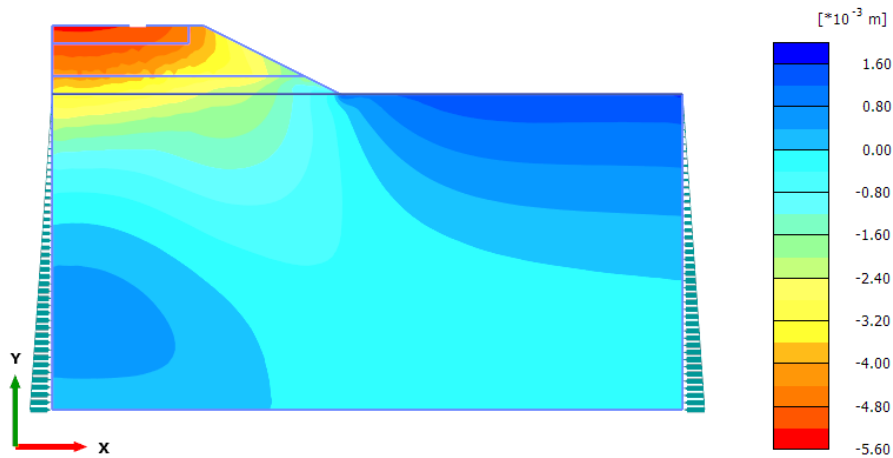


Fig. 5.6 Typical total vertical displacements U_y contour diagram

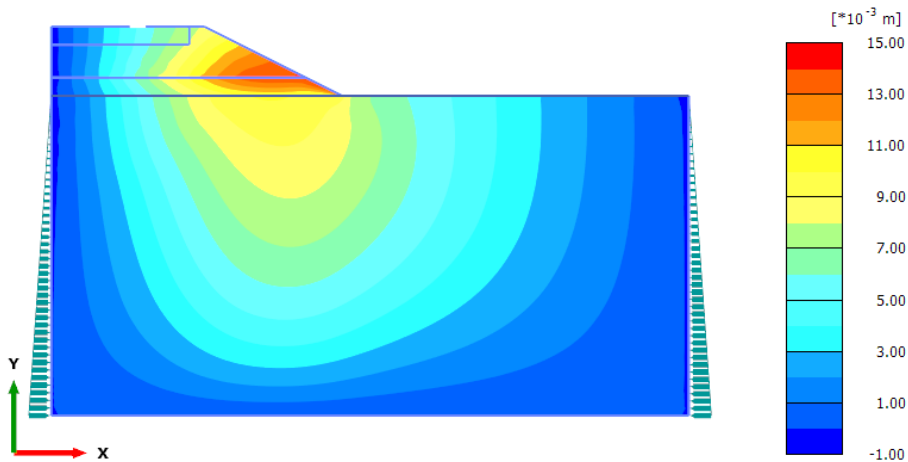


Fig. 5.7 Typical total horizontal displacements U_x contour diagram

Fig. 5.8 displays the developed excess pore water pressure bulbs at the end of the dynamic loading phase for Train 6. For this case, the ground water level (GWL) was at 0.0 m below ground surface (m BGS) (i.e. GWL at the ground surface). Positive excess pore water developed due to the cyclic loading event in the vicinity of the cross-tie in the sub-ballast and subgrade. However, maximum excess pore water pressure generated due to the cyclic event was estimated to be 180 kPa in the sub-grade at depths more than $0.5B$ (B =width of the cross-tie). It is evident that undrained conditions prevailed in the sub-grade and sub-ballast. In the meantime, capillary fringes were noticed to form in the sub-ballast layer. It is also noted that the pore water pressure values reported herein are generally higher than the FEM results reported by Li et al. (2019) and Mekonnen (2019). This is explained in part by the variance in load magnitudes used by both studies in comparison with the current study. In the current study actual wheel load time histories were obtained from wayside instrument of track crossed Class I heavy haul freight trains.

Fig. 5.9 shows the developed effective saturation at the end of the dynamic loading phase for Train 6. In the sub-grade, below the water table and in the vicinity of the cross-tie, the effective saturation drops to approximately 70%. However, in the sub-grade and sub-ballast, pore pressure remains positive in the vicinity of the cross-tie. Meanwhile, the pore pressure is zero in the dry ballast layers above the water table; nonetheless the sub-ballast layers remain saturated due to the capillary rise but with negative pore pressure (i.e. matric suction), as shown in Figs. 5.8 and 5.9. It is worth mentioning that the in PLAXIS the atmospheric pressure is air pressure is constant and air pressure taken as zero.

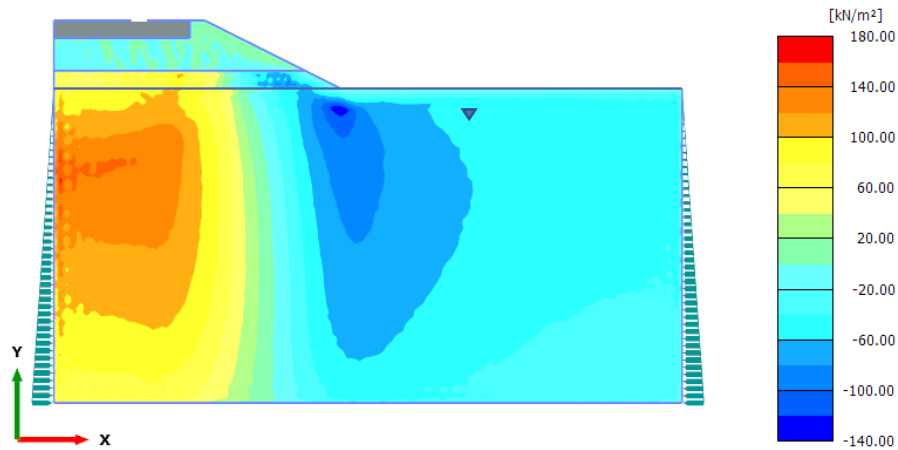


Fig. 5.8 Typical excess pore water pressure PWP_{Excess} contour diagram

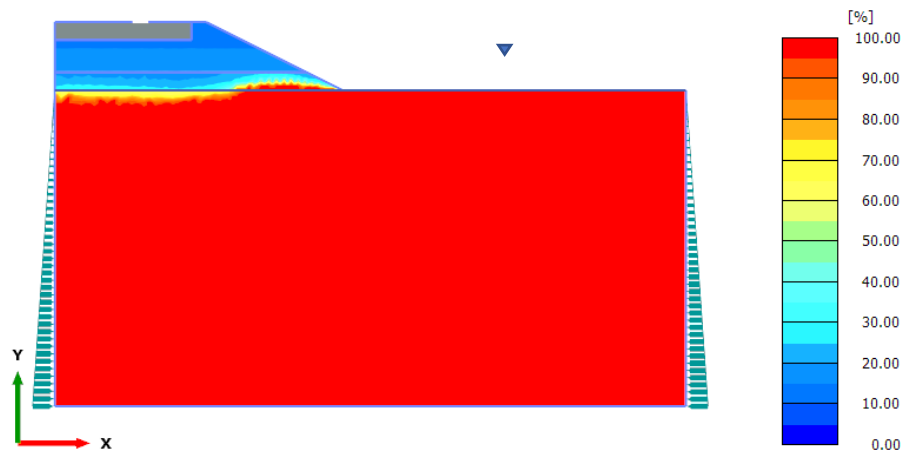


Fig. 5.9 Typical effective saturation contour diagram $GWL = 0B$

5.4 Discussion and Analysis

In the unsaturated part of the track foundation (i.e., ballast) water is present with air as water menisci due to the capillary effect (i.e., surface tension). Excess pore pressure is governed by three factors: the water compressibility, air compressibility and surface tension (i.e. matric suction effect). The rise of excess pore water pressure due to the cyclic loading event was facilitated by the negative pore pressure developed throughout the ballast and sub-ballast layers

(i.e., farther away from the cross-tie). The saturated zone in the subgrade extended to the sub-ballast and ballast as the pressure surface from the water is equal to the atmospheric pressure. This explains the high negative pore pressure developed at the toe of the embankment estimated to be -80 kPa. Thus, the sub-structure is subdivided into three zones: capillary fringe zone (i.e., saturated zone), intermediate and surface water zones (unsaturated zones). For the undrained track foundation condition, the pore pressures profile plays a crucial role in the saturation of the sub-structure. For fully saturated track foundation (i.e., voids are filled by water only and no air) high excess pore water pressures are generated due to the low compressibility of pore fluids. On the other hand, for unsaturated track foundation, (i.e. voids are filled by water and air), low excess pore water pressures are generated due to the higher compressibility of pore fluid in contrast with saturated track foundation.

Figs. 5.10 - 5.12 show the change in the profile of excess pore water pressure with depth under the cross-tie. In general, the excess PWP under the cross-tie is directly correlated with the train velocity. The increase in the excess PWP as the train velocity increases is attributed to the prevalence of undrained conditions and insufficient time between loading-unloading-reloading phases to dissipate excess PWP. As can be observed from Figs. 5.10-12, the track substructure is fully saturated up to the middle layer of the ballast. However, negative PWP is only noticed in the vicinity of the rail seat and cross-tie toe. The results presented in Figs. 5.10-12 are in agreement with Terzaghi's principle. The pore water pressure in the partially saturated track foundation in the vicinity of the rail seat, above the water table, is estimated to be negative. In the vadose zone, effective stresses are approximately equivalent to total stresses. The fact that the effective stresses are greater than total stresses indicates that the pore water pressure in the loading zone of the partially saturated track foundation is actually negative.

Fig. 5.10 shows the variation in the profile of excess pore water pressure with depth under the centre cross-tie. As the stress points under the cross-tie, which are used to estimate PWP, are located further away from the loading zone, the effect of suction decreases drastically. Fig. 5.11 demonstrates that the maximum negative PWP ≈ -5 kPa in the vicinity of the loading zone. Meanwhile, the maximum positive excess PWP ≈ 140 kPa at a depth of $0.5B$ ($B =$ width

of the cross-tie). As the train velocity increased from 67 km/h to 102 km/h, the excess PWP increased 1.2 times.

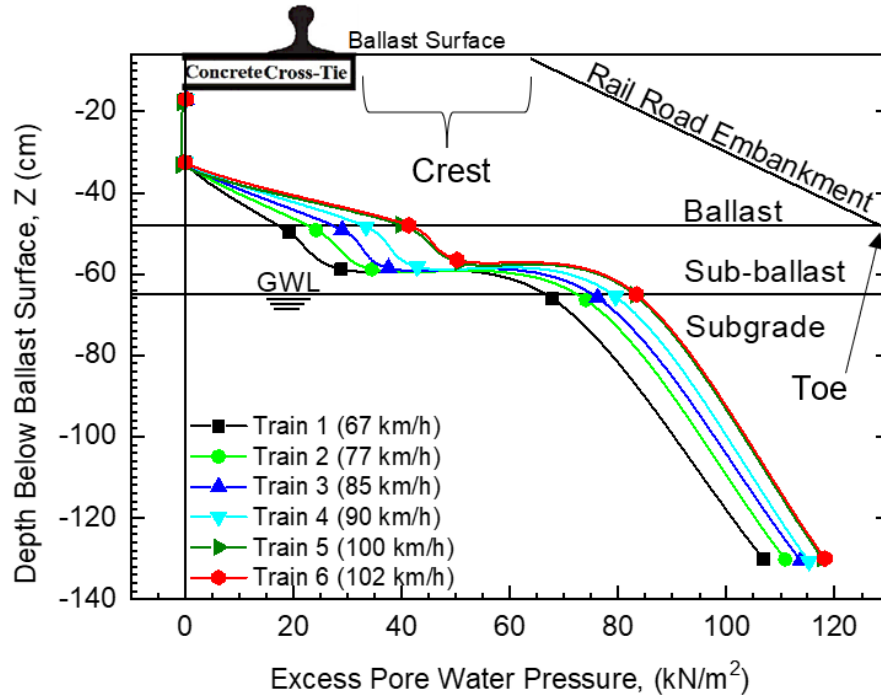


Fig. 5.10 Profile of excess pore water pressure under cross-tie centre

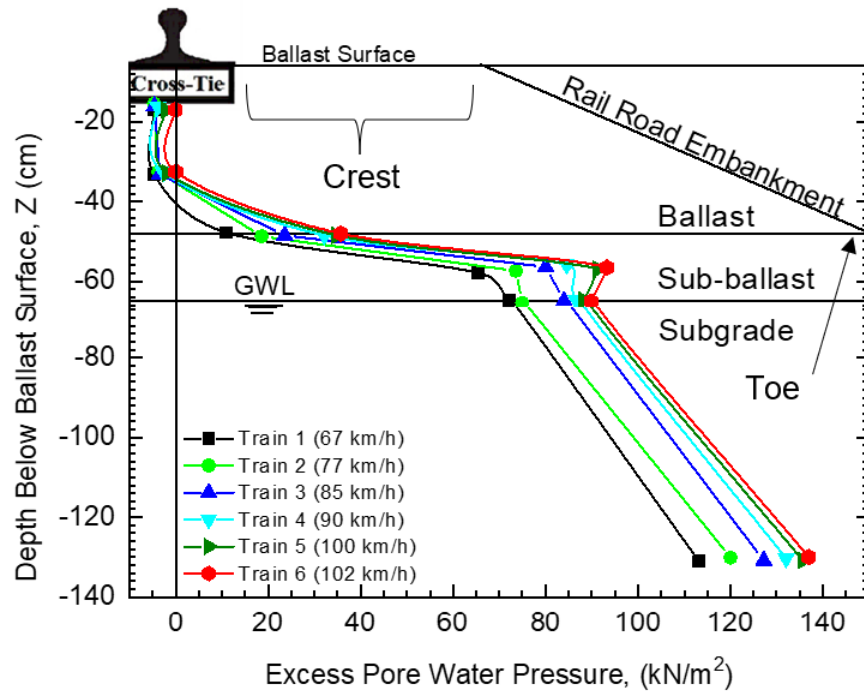


Fig. 5.11 Profile of excess pore water pressure under rail seat

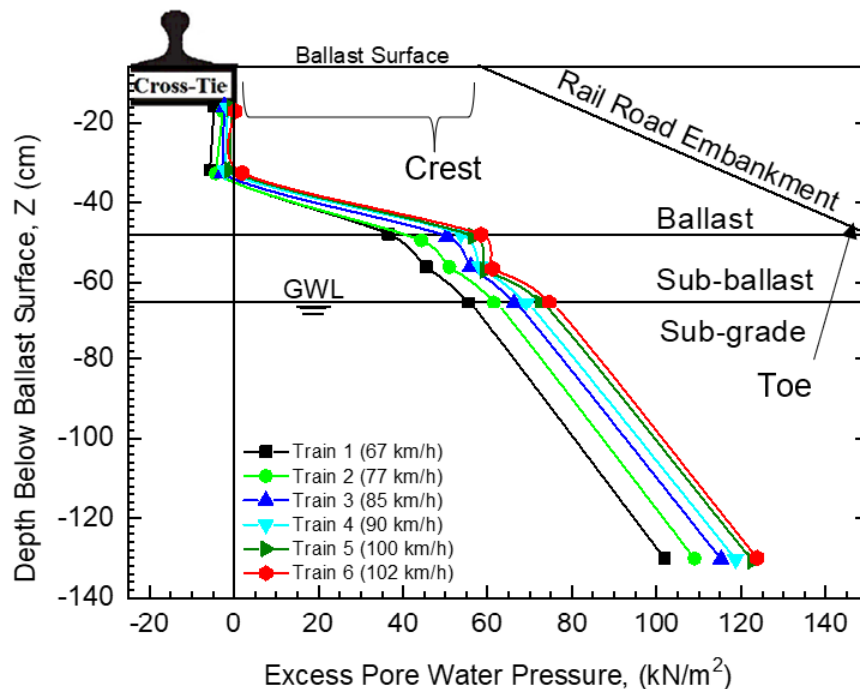


Fig. 5.12 Profile of excess pore water pressure under cross-tie toe

Figs. 5.13 - 5.14 show the variation of the excess pore water pressure profile with depth away from the cross-tie. In general, excess PWP away from the cross-tie is directly correlated with the train velocity. As can be observed from Figs. 5.13-14 the track substructure is fully saturated up to the middle layer of the sub-ballast. However, negative PWP is noted in the vadose zone (i.e. zone above the water table where effective stresses are higher than total stresses). Fig. 5.13 shows the variation in the profile of excess pore water pressure with depth under the ballast surface. The results presented in Fig. 5.14 show that the maximum negative PWP occurred at the interface between ballast and sub-ballast, and subgrade and sub-ballast and was approximately - 20 kPa. Meanwhile, the maximum positive excess, PWP \approx 95 kPa occurred at a depth of $0.5B$ (B = width of the cross-tie). As the train velocity increased from 67 km/h to 102 km/h, the excess PWP increased 1.3 times. When cyclic train passby load was applied by the super-structure to the compressible soil, the load was immediately taken up by the pore water in the form of excess PWP. With time, excess pressure would dissipate, and the pore pressure will go back to the static levels. Consequently, the track sub-structure would

deform resulting in permanent settlement. This behaviour explains the excessive horizontal deformation experienced by the railroad embankment toe.

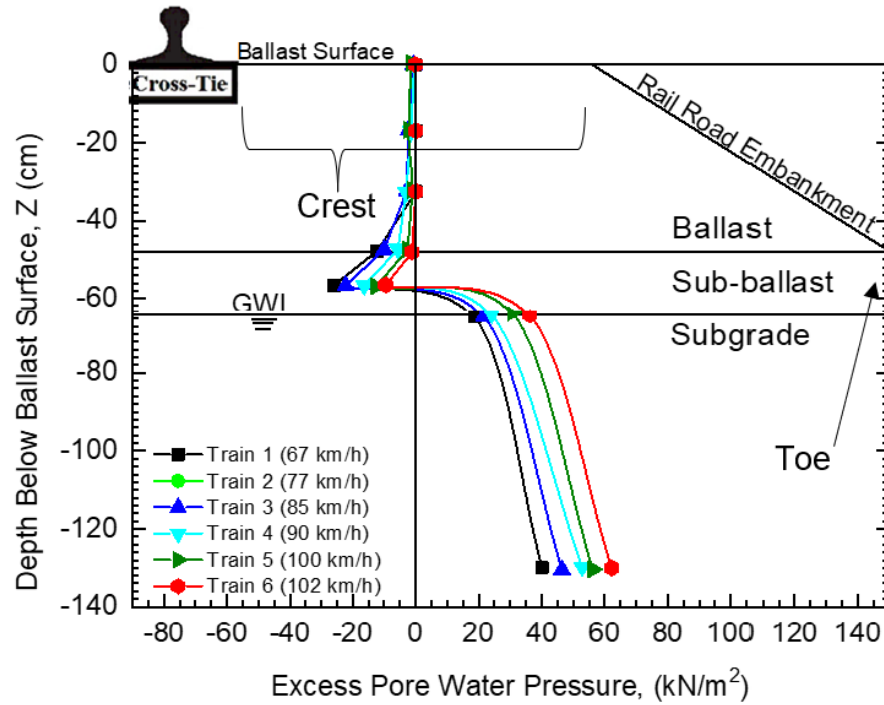


Fig. 5.13 Profile of excess pore water pressure under crest

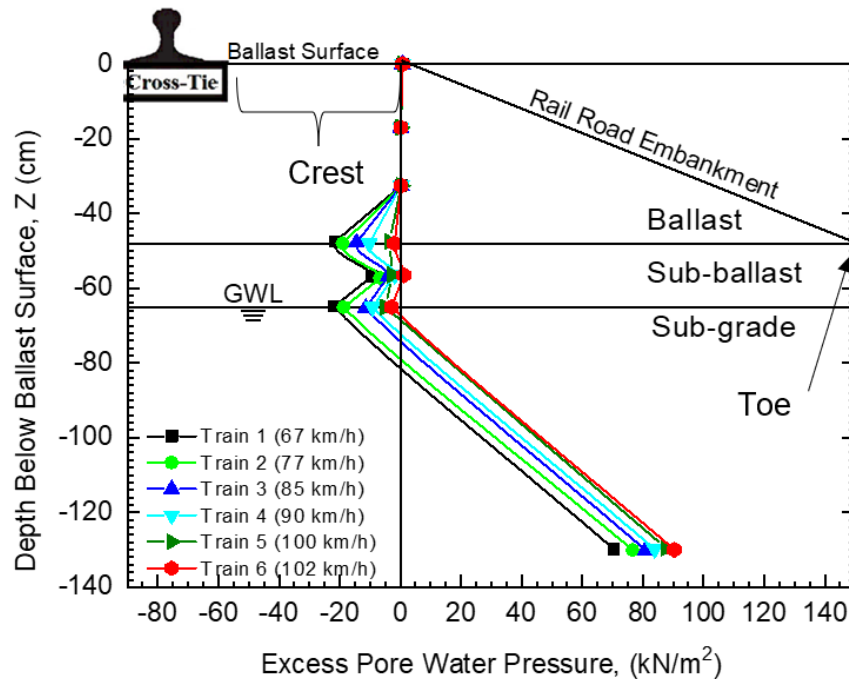


Fig. 5.14 Profile of excess pore water pressure slope edge

5.5 Summary

The suction component of pore water pressure (i.e. negative PWP) is seldom investigated due to its stabilizing role incorporated as effective stresses. For modelling purposes, PLAXIS takes atmospheric pressure as zero. Nevertheless, in fouled ballasts, negative PWP draws water from the capillary fringe from saturated sub-structure layers and causes further fouling. Therefore, dynamic plane-strain FE models were developed, calibrated, and validated then used to investigate the effect of train velocity on generated positive and negative excess pore water pressures using a variety of loading time histories for different train velocities. The results demonstrate that positive excess pore water developed due to the cyclic loading event in the vicinity of the cross-tie in the sub-ballast and subgrade. Undrained conditions prevailed in the sub-grade and sub-ballast (i.e. excess PWP developed). Capillary fringes were noticed to form predominantly in the sub-ballast layer. The following observations and conclusions are made:

- (i) Maximum excess pore water pressure generated due to the cyclic event was as high as 180 kPa in the sub-grade at depths more than 0.5B.
- (ii) The effective saturation in the subgrade below the water table and in the vicinity of the cross-tie drops to approximately 70%.
- (iii) High negative pore pressure develops at the toe of the embankment with values as high as -80 kPa.
- (iv) A maximum negative PWP of -5 kPa developed in the vicinity of the loading zone (near the cross-tie) and a maximum positive excess PWP of 140 kPa developed at a depth of 0.5B.
- (v) In the vicinity of the cross-tie, the excess PWP increased by 1.2 times as the train velocity increased from 67 km/h to 102 km/h.
- (vi) a maximum positive excess PWP of 95 kPa developed away from the loading zone (far from the cross-tie) at a depth of 0.5B.

(vii) Away from the cross-tie, the excess PWP increased by 1.3 times as the train velocity increased from 67 km/h to 102 km/h.

(viii) Further numerical modeling should consider seasonal fluctuation of groundwater table obtained from wayside developed monitoring wells.

(viii) Further numerical modeling should consider the use of geogrids to inhibit fine migration

Chapter 6

6 Conclusions, Major Findings and Recommendations for Future work

6.1 Conclusions

Triaxial static and cyclic tests were conducted on different sub-ballast soil samples to investigate the dynamic geo-mechanical behaviour and characteristics of fouled railroad sub-ballast under static and cyclic loading. The effects of train speed on the behavior of fouled railroad were evaluated in terms of the response of the railroad substructure as a result of the applied cyclical loading. This was achieved by varying the loading frequency during the cyclic triaxial tests. The cyclic loading was applied at frequencies of 2.5 Hz, 5.0 Hz and 10 Hz to simulate train cars travelling at 32 km/h, 64 km/h, and 128 km/h, respectively (Indraratna et al., 2010). The cyclic responses obtained from the experimental study were presented in terms of time history, strain, and number of cycles. This study evaluated the role of the sub-ballast in the railroad degradation process by studying the effect of simulated train speed on fouled sub-ballast samples. Based on the results of the study, some constraints are suggested for speed of trains travelling on fouled railroad segments. It is recommended that the maximum speed of trains in fouled zones be limited to 32 km/h.

Long-term monitoring program was conducted for fouled railroad segment of the Sioux City rail track segment. Candidate fouled ballast bed was instrumented and data was collected from uncontrolled sources (normal train traffic) to establish a relationship between the train load and the fouled ballast bed and superstructure responses. The field data was obtained using a variety of techniques, including conventional rail strain gauge circuits and digital correlation of images obtained by highspeed cameras. The current study demonstrated that the instrumentation placed above the cross-tie can provide meaningful data (i.e. longitudinal range of influence of loads on the rail and cross-tie uplift ratio). A method is proposed for continuously measuring spatially varying dynamic fouled static track stiffness by monitoring the longitudinal range of

influence for distant wheel load. The proposed method enables estimating fouled static track stiffness (k) from the longitudinal range of influence and uplift ratio.

The pattern and amplitude of the acceleration signal of cross-ties in the fouled segment due to the train applied cyclic wheel load varied with the train load and track support conditions. In general, the measured acceleration amplitudes obtained from different accelerometers in the fouled segment were close to each other, which confirms the reliability of acceleration measurements. The acceleration amplitudes measured in both directions of Z-axis (i.e., \pm) were higher for the fouled segment. The vibrational behaviour of concrete cross-ties in terms of magnitude and spectral distribution depends on the fouling state of the ballast and train velocity. For the fouled segment, although favorable environmental conditions resulted in an improved performance in terms of track deflection, the vibrational response increased. For stiff track, the vibration signature for each wheel was distinctive, i.e., fewer number of noise vibrational peaks produced for each wheel.

In general, as the train velocity increased and the static track stiffness increased, the train-induced vibrations increased at the fouled segment. However, the results reveal that for train velocity $V_{Train} \leq 70.0$ km/h, the effect of train velocity for well supported ties is minimal on the maximum magnitude of vertical acceleration. For trains operating at a velocity $V_{Train} \leq 70.0$ km/h, the highest measured acceleration for supported ties $a_z = \pm 1.0$ g. Generally, the results demonstrated that for all cases of train speed, static track stiffness and wheel loading, the amplitude of the acceleration was practically the same in both directions of the Z-axis (upwards and downwards).

The fast Fourier transfer (FFT) analysis indicated that as the static track stiffness decreases (i.e. $k \leq 25$ MN/m) the amplitude of the sinusoid for supported cross-ties is higher than that for voided cross-ties for $V_T < 90$ km/h. However, at higher velocities, the amplitude of the sinusoid decreases and becomes practically equal to that of voided cross-ties. The results demonstrated that there is a critical train velocity range, $V_T \approx 70$ km/h – 90 km/h, where frequency of the peak dominant response is higher for voided cross-ties. For typical static track stiffness (i.e. 25 MN/m $\leq k \leq 51$ MN/m), optimum track performance manifested in low

amplitude of peak response was observed for $V_T < 90$ km/h. As the static track stiffness increases, the cross-ties perform optimally regardless of the state of fouling and train velocity. This can be explained by the relatively low amplitude of the peak response (high energy dissipation) and high frequency response (high ground vibrations).

Unlike fully supported cross-ties, the vibrational response of the voided cross-ties varied with cross-tie support conditions. This is attributed to the key role of static track stiffness (k) in influencing the support conditions of the voided cross-tie. To avoid excessive train-induced vibrations (i.e. above the vibration level of the supported cross-ties) when crossing through fouled track segments, operators can use the empirical data presented in the current study as a general guideline to reduce vibrations from the source, i.e., the track.

The suction component of pore water pressure (i.e. negative PWP) is seldom investigated due to its stabilizing role, which is typically incorporated in any analysis as effective stresses. Nevertheless, in fouled ballasts, negative PWP draws water in the form of capillary fringe from saturated sub-structure layers and causes further fouling. Therefore, dynamic 2D analysis was conducted employing calibrated plane-strain FE models to investigate the effect of train velocity on generated positive and negative excess pore water pressures using a variety of loading time histories for different train velocities. The results demonstrate that positive excess pore water pressure developed in the vicinity of the cross-tie in the sub-ballast and subgrade due to the cyclic loading. Undrained conditions prevailed in the sub-grade and sub-ballast. Capillary fringes were noticed to form predominantly in the sub-ballast layer.

6.2 Major Findings and Observations

- Soil plasticity and confining pressure are not the only important factors that shape the damping curves; the loading rate and particle size play equally important role in determining the damping behaviour of the sub-ballast.
- Permanent axial strains and poor excess pore water pressure dissipation were accompanied by structural deformations of the soil specimen as the number of load cycles increased.

- Although the sub-ballast specimen exhibited prolonged failure behaviour under different loading rates, the shear stress amplitude decreased as the number of load cycles increased.
- Sub-ballast specimen loaded at a frequency of 2.5 Hz, simulating a train traveling at a speed of 32 km/h, exhibited 3 distinct shear modulus degradation stages due to its prolonged failure behaviour, unlike the samples loaded at 5Hz and 10Hz, which were characterized by faster failure response.
- Below the threshold strain level ($\gamma_{0.7}$)= 0.08 %, 0.1 %, and 0.2 %, the damping ratio (ξ) ranged from 1% to 2 % for soil specimens loaded at 2.5 Hz, 5 Hz, and 10 Hz, respectively.
- Damping ratio (ξ) increased exponentially for specimens loaded at 2.5Hz, 5Hz, and 10Hz.
- For the field test section, the level of water increased gradually across the depth of the fouled ballast. A layer 76 mm in thickness (from depth 0.102 m to 0.178 m below the bottom of the cross-tie) was found highly fouled and was identified as the source of perched water.
- Below the cross-tie, at depths of 0.025 m and 0.254 m, the water-storage capacity of fouled ballast bed decreased for typical and rigid static track stiffness, i.e. $k \geq 25$ MN/m.
- When train wheel was at a distance of 0.1S, i.e. in the rail-crib area, the maximum uplift force developed in the rail-tie as the first wheel of the front bogie approached and last wheel departed.
- The linear range of influence of distant wheel loads on the superstructure (rail, cross-tie) and subgrade vertical deflections increased as fouled static track stiffness (k) increased.
- The bending moments from the enveloping axles generated high uplift forces in the CWR. Furthermore, the approaching and departing wheels generated uplift forces in the rail-tie section. Maximum uplift force was generated when the wheel was on the crib area (the hanging segment of the CWR between two cross-ties).
- Fouled static track stiffness (k) substantially altered the response of the fouled track superstructure. The fouled ballast bed performance could be considered acceptable under traffic loading at below-zero ambient temperature (i.e. frozen soil conditions).
- Employing the tie load ratio as a proxy for cross-tie support efficiency does not capture the response of the superstructure in fouled railroad environment, especially for light wheel loads. Employing the uplift ratio to analyse the uplift forces due to the passage of front and

rear wheels of the bogie, and the linear range of influence of distant wheel loads on the rail superstructure offer a better alternative.

- The longitudinal range of influence (S) of wheel load is linearly correlated with fouled static track stiffness (k) and thus can be used to predict the static track stiffness.
- The cross-tie uplift ratio is exponentially correlated with fouled static track stiffness (k) and thus can be used to predict the fouled static track stiffness (k).
- The statistical analysis demonstrated the suitability of the presented empirical solutions for estimating stiffness (k) of fouled track in terms of (S) and cross-tie uplift ratio with $R^2 = 81.68\%$ and 77.07% , respectively.
- For static track stiffness, $k \leq 51$ MN/m, the train velocity should be less than 70 km/h so that the vertical acceleration of voided cross-ties remains below $\pm 3.0g$ (i.e. acceleration level of supported cross-ties for typical track stiffness range).
- For stiff track, $k \geq 51$ MN/m, the train velocity should be less than 20 km/h so that the vertical acceleration of voided cross-ties remains below $\pm 3.0g$ (i.e. acceleration level of supported cross-ties for typical track stiffness range).
- Maximum excess pore water pressure generated due to the cyclic event was as high as 180 kPa in the sub-grade at depths more than $0.5B$.
- The effective saturation in the sub-grade below the water table and in the vicinity of the cross-tie drops to approximately 70%.
- High negative pore pressure develops at the toe of the embankment and could be as high as -80 kPa.
- In the vicinity of the cross-tie, the maximum negative PWP could reach -5 kPa and the maximum positive excess PWP could reach 140 kPa at a depth of $0.5B$.
- Away from the cross-tie, the maximum positive excess PWP reaches 95 kPa at a depth of $0.5B$.
- The excess PWP increases 1.2 times in the vicinity of the cross-tie as the train velocity increases from 67 km/h to 102 km/h.
- The excess PWP increased 1.3 times away from the cross-tie as the train velocity increases from 67 km/h to 102 km/h.

6.2 Recommendations for Future Work

- Further field monitoring should involve controlled passes of train with constant and variable travel speeds. This can help determine whether an optimal combination of train loading and speed can be established to maintain the integrity of fouled static track stiffness.
- The gap underneath the cross-tie can be simulated using a scaled physical model or a full-scale prototype (i.e. the current study). However, for the scaled model would give crucial insights especially if placed in a plex glass box and transparent fine materials were used as the fouling agent. The ballast needs to be mixed with fines and cyclic loading needs to be applied to the cross-tie to achieve in-situ conditions.
- Tactile sensors could be placed underneath the rails and at the tie-ballast interface for force measurement and pressure mapping.
- Accelerometers could be embedded in the railroad substructure at deferent depths to quantify ground vibration amplification.
- In situ monitoring could include monitoring wells to observe the ground water conditions using level loggers.
- Accelerometers could be placed at deferent points in the free field (i.e. away from the track) to measure vibration decay.
- Further studies are required to enable deducing train velocity thresholds to minimize ground borne vibrations and attenuation distance from the track.
- Further numerical modeling should involve variance in loading magnitudes calibrated with wayside instrumentation, and seasonal fluctuation of groundwater table obtained from wayside developed monitoring wells.

References

- AAR (2020). Freight Railroads & Positive Train Control (PTC), The Association of American Railroads.
- AASHTO (2008). Classification of soil-aggregate mixtures for highway construction purposes 145-91.
- Adam, D., A. Vogel and A. Zimmermann (2007). Ground improvement techniques beneath existing rail tracks. *Proceedings of the Institution of Civil Engineers-Ground Improvement* 11(4): 229-235.
- AEA-Technology-Rail (2006). Findings from the investigation of SFE measurement techniques. London, UK AEA Technology Rail.
- Ahlbeck, D. R., M. R. Johnson, H. D. Harrison and J. M. Tuten (1980). Measurements of Wheel/Rail Loads on Class 5 Track, United States. Federal Railroad Administration.
- Ahmad, S. (2016). Piezoelectric Device for Measuring Shear Wave Velocity of Soils and Evaluation of Low and High Strain Shear Modulus. PhD.
- Aikawa, A. (2018). Vertical Natural Vibration Modes of Ballasted Railway Track. *New Trends in Structural Engineering*, IntechOpen.
- Alobaidi, I. and D. Hoare (1999). Mechanisms of pumping at the subgrade-subbase interface of highway pavements. *Geosynthetics International* 6(4): 241-259.
- Alobaidi, I. and D. J. Hoare (1996). The development of pore water pressure at the subgrade-subbase interface of a highway pavement and its effect on pumping of fines. *Geotextiles and geomembranes* 14(2): 111-135.
- Anderson, W. F. and A. J. Key (2000). Model testing of two-layer railway track ballast. *Journal of Geotechnical and Geoenvironmental Engineering* 126(4): 317-323.
- AREMA (2013). American railway engineering and maintenance-of-way association. Manual for railway engineering. Maryland, United States.
- Askarinejad, H., M. Dhanasekar, P. Boyd and R. Taylor (2015). Field measurement of wheel—rail impact force at insulated rail joint. *Experimental Techniques* 39(5): 61-69.
- Askarinejad, H., M. Dhanasekar and C. Cole (2013). Assessing the effects of track input on the response of insulated rail joints using field experiments. *Proceedings of the Institution of Mechanical Engineers, Part F: Journal of Rail and Rapid Transit* 227(2): 176-187.

ASTM (2004). Standard Test Method for Load Controlled Cyclic Triaxial Strength of Soil D5311: 1167-1176.

ASTM (2004). Standard test methods for particle-size distribution (gradation) of soils using sieve analysis ASTM D6913/6913M. C. D. o. S. Rock, ASTM International.

ASTM (2011). Method for Consolidated Drained Triaxial Compression Test for Soils D7181-11 1: 1-11.

ASTM (2013). Standard test methods for the determination of the modulus and damping properties of soils using the cyclic triaxial apparatus ASTM D3999-11.

Ayres, D. (1986). Geotextiles or geomembranes in track? British railways' experience. *Geotextiles and Geomembranes* 3(2-3): 129-142.

Azizi, M., M. Shahravi and J.-A. Zakeri (2021). Effect of unsupported sleepers on dynamic behavior of running vehicles and ride comfort index. *Proceedings of the Institution of Mechanical Engineers, Part C: Journal of Mechanical Engineering Science*: 0954406221989371.

Bailey, B., D. Hutchinson, D. Gordon, G. Siemens and M. Ruel (2011). Field and laboratory procedures for investigating the fouling process within railway track ballast. *Proceeding of the 2011 Pan-Am CGS Geotechnical Conference*, 8p.

Bian, X., J. Jiang, W. Jin, D. Sun, W. Li and X. Li (2016). Cyclic and postcyclic triaxial testing of ballast and subballast. *Journal of Materials in Civil Engineering* 28(7): 04016032.

Boore, D. M., C. D. Stephens and W. B. Joyner (2002). Comments on baseline correction of digital strong-motion data: Examples from the 1999 Hector Mine, California, earthquake. *Bulletin of the Seismological Society of America* 92(4): 1543-1560.

Bowness, D., A. Lock, W. Powrie, J. Priest and D. Richards (2007). Monitoring the dynamic displacements of railway track. *Proceedings of the Institution of Mechanical Engineers, Part F: Journal of Rail and Rapid Transit* 221(1): 13-22.

Brinkgreve, R., E. Engin and W. Swolfs (2017). *Plaxis 2D manual*. Rotterdam, Netherlands, Balkema.

Bruzek, R., T. D. Stark, S. T. Wilk, H. B. Thompson and T. R. Sussmann Jr (2016). Fouled Ballast Definitions and Parameters. *ASME/IEEE Joint Rail Conference, American Society of Mechanical Engineers*.

Bruzek, R., T. D. Stark, S. T. Wilk, H. B. Thompson and T. R. Sussmann (2016). Fouled Ballast Definitions and Parameters. *2016 Joint Rail Conference, American Society of Mechanical Engineers*.

- Burns, B., G. Ghataora and P. Sharley (2006). Development and testing of geosand composite layers using a pumping index test. Proceedings of Railway foundations conference: Railfound.
- Cai, Y., Z. Cao, H. Sun and C. Xu (2010). Effects of the dynamic wheel–rail interaction on the ground vibration generated by a moving train. *International Journal of Solids and Structures* 47(17): 2246-2259.
- Chang, C. S., C. W. Adegoke and E. T. Selig (1980). GEOTRACK model for railroad track performance. *Journal of Geotechnical and Geoenvironmental Engineering* 106(11).
- Chrismer, S. and D. Davis (2000). Cost comparisons of remedial methods to correct track substructure instability. *Transportation research record* 1713(1): 10-14.
- Correia, A. G., J. Santos, J. M. C. Barros and S. Niyama (2001). An approach to predict shear modulus of soils in the range of 10^{-6} to 10^{-2} strain levels. 4th International Conference on Recent Advances in Geotechnical Engineering and Soil Dynamics and Symposium in Honor of Professor W.D. Liam Finn, San Diego California
- Costa, P. A., R. Calçada and A. S. Cardoso (2012). Track–ground vibrations induced by railway traffic: In-situ measurements and validation of a 2.5 D FEM-BEM model. *Soil Dynamics and Earthquake Engineering* 32(1): 111-128.
- Cui, Y.-J., F. Lamas-Lopez, V. N. Trinh, N. Calon, S. C. D’aguilar, J.-C. Dupla, A. M. Tang, J. Canou and A. Robinet (2014). Investigation of interlayer soil behaviour by field monitoring. *Transportation Geotechnics* 1(3): 91-105.
- Dawn, T. (1983). Ground vibrations from heavy freight trains. *Journal of sound and vibration* 87(2): 351-356.
- Dobry, R. and M. Vucetic (1987). Dynamic properties and seismic response of soft clay deposits, Department of Civil Engineering, Rensselaer Polytechnic Institute.
- Duong, T. V., Y.-J. Cui, A. M. Tang, J.-C. Dupla and N. Calon (2014). Effect of fine particles on the hydraulic behavior of interlayer soil in railway substructure. *Canadian geotechnical journal* 51(7): 735-746.
- Duong, T. V., Y.-J. Cui, A. M. Tang, J.-C. Dupla, J. Canou, N. Calon and A. Robinet (2014). Investigating the mud pumping and interlayer creation phenomena in railway sub-structure. *Engineering Geology* 171: 45-58.
- Duong, T. V., Y.-J. Cui, A. M. Tang, J.-C. Dupla, J. Canou, N. Calon and A. J. E. g. Robinet (2014). Investigating the mud pumping and interlayer creation phenomena in railway sub-structure. 171: 45-58.

- Duong, T. V., Y.-J. Cui, A. M. Tang, J. C. Dupla, J. Canou, N. Calon, A. Robinet, B. Chabot and E. De Laure (2014). Physical model for studying the migration of fine particles in the railway substructure. *Geotechnical Testing Journal* 37(5): 895-906.
- Ebrahimi, A. (2011). Behavior of fouled ballast. *Journal of Railway Track Structures* 107(8).
- Ebrahimi, A. (2011). Deformational behavior of fouled railway ballast PhD.
- Ebrahimi, A., J. M. Tinjum and T. B. Edil (2012). Protocol for testing fouled railway ballast in large-scale cyclic triaxial equipment. *ASTM Geotechnical Testing Journal* 35(5): 1-9.
- Ebrahimi, A., J. M. Tinjum and T. B. Edil (2014). Deformational behavior of fouled railway ballast. *Canadian Geotechnical Journal* 52(3): 344-355.
- Ebrahimi, A., J. M. Tinjum and T. B. Edil (2015). Deformational behavior of fouled railway ballast. *Canadian Geotechnical Journal* 52(3): 344-355.
- EC-European-Commission (2011). Roadmap to a Single European Transport Area-Towards a competitive and resource efficient transport system. White Paper, Communication 144.
- Edwards, J. R., M. S. Dersch and R. G. Kernes (2017). Improved Concrete Crosstie and Fastening Systems for US High Speed Passenger Rail and Joint Corridors: Volume 1, Project Summary Report.
- Esmaeili, M., P. Aela and A. Hosseini (2017). Experimental assessment of cyclic behavior of sand-fouled ballast mixed with tire derived aggregates. *Soil Dynamics and Earthquake Engineering* 98: 1-11.
- Esmaeili, M., P. Aela and A. Hosseini (2019). Effect of moisture on performance of mixture of sand-fouled ballast and tire-derived aggregates under cyclic loading. *Journal of Materials in Civil Engineering* 31(2): 04018377.
- Esmaeili, M., J. A. Zakeri and S. A. Mosayebi (2014). Effect of sand-fouled ballast on train-induced vibration. *International Journal of Pavement Engineering* 15(7): 635-644.
- Esveld, C. (1989). *Track Geometry and Vehicle Reactions*. Rail Engineering International Edition 4: 13.
- Esveld, C. (2001). *Modern Railway Track*. The Netherlands. MRT-Productions.
- Ethier, Y., M. N. Hussien, D. Elbeggo and M. Karray (2016). Shear wave velocity of soft sensitive clay using novel piezoelectric technique P-RAT. *GeoVancouver*. Vancouver BC
- Ewing, W. M., W. S. Jardetzky, F. Press and A. Beiser (1957). Elastic waves in layered media. *PhT* 10(12): 27.

- Fallah Nafari, S., M. Gül, M. T. Hendry and J. R. Cheng (2018). Estimation of vertical bending stress in rails using train-mounted vertical track deflection measurement systems. *Proceedings of the Institution of Mechanical Engineers, Part F: Journal of Rail and Rapid Transit* 232(5): 1528-1538.
- FederalRailroadAdminstration (2020). Track Safety Standard. D. o. Transportation. United States Federal Railroad Administration.
- Feng, S. (2012). Monitoring and analysis of longitudinal forces from CWRs in ballastless tracks on long spanning bridges for high-speed railways. Nanchang, China, East China Jiaotong University.
- Feng, S., X. Lei and P. Zhang (2011). Remote monitoring and analysis of additional contractility from CWRs on bridges. *Journal of East China Jiaotong University* 28(2): 1-5.
- FRA (2021). FRA Office of Research, Development and Technology - Current Projects 2021. U. S. D. o. Transportation. Washington, DC, Federal Railroad Administration.
- Frohling, R. D. (2009). Deterioration of railway track due to dynamic vehicle loading and spatially varying track stiffness, University of Pretoria.
- Gerald, P. and J. Richard (1987). Performance of large-scale model single tie-ballast systems. *Transportation Research Record* 1134: 7-14.
- Ghataora, G., B. Burns, M. Burrow and H. Evdorides (2006). Development of an index test for assessing anti-pumping materials in railway track foundations. *Proceedings of the First International Conference on Railway Foundations, Railfound06*, University of Birmingham, UK.
- GlobalRailwayReview (2021) Sustainability.
- Grassie, S. L. (2012). Rail irregularities, corrugation and acoustic roughness: characteristics, significance and effects of reprofiling. *Proceedings of the Institution of Mechanical Engineers, Part F: Journal of Rail and Rapid Transit* 226(5): 542-557.
- Grossniklaus, R. (2016). Advances in tamping technology. AusRAIL PLUS 2016, Rail-Moving the Economy Forward, 21-23 November 2016, Adelaide, South Australia, Australia.
- Hamarat, M., S. Kaewunruen, M. Papaelias and M. Silvast (2019). New insights from multibody dynamic analyses of a turnout system under impact loads. *Applied Sciences* 9(19): 4080.
- Han, X. and E. Selig (1997). Effects of fouling on ballast settlement. *Proc., 6th International Heavy Haul Railway Conference*.

- Hanson, C. (1995). Transit noise and vibration impact assessment, US Department of Transportation, Federal Transit Administration.
- Haque, A., E. Kabir and A. Bouazza (2007). Cyclic filtration apparatus for testing subballast under rail track. *Journal of Geotechnical and Geoenvironmental Engineering* 133(3): 338-341.
- Huang, H., E. Tutumluer and W. Dombrow (2009). Laboratory characterization of fouled railroad ballast behavior. *Transportation research record* 2117(1): 93-101.
- Hudson, A., G. Watson, L. Le Pen and W. Powrie (2016). Remediation of mud pumping on a ballasted railway track. *Procedia engineering* 143: 1043-1050.
- Hunt, H. (2005). Modelling of rail roughness for the evaluation of vibration-isolation measures.
- Indraratna, Lackenby and Christie (2005). Effect of confining pressure on the degradation of ballast under cyclic loading.
- Indraratna, S. S. Nimbalkar and N. Tennakoon (2010). The behaviour of ballasted track foundations: track drainage and geosynthetic reinforcement. *GeoFlorida 2010: Advances in analysis, modeling & design*: 2378-2387.
- Indraratna, Tennakoon, Nayoma, Nimbalkar, Sanjay, Rujikiatkamjorn and Cholachat. (2012). Behaviour of Clay Fouled Ballast under Drained Triaxial Testing. *Géotechnique* 63(5): 410-419.
- Indraratna, B., A. Attya and C. Rujikiatkamjorn (2009). Experimental investigation on effectiveness of a vertical drain under cyclic loads. *Journal of Geotechnical and Geoenvironmental Engineering* 135(6): 835-839.
- Indraratna, B., N. T. Ngo and C. Rujikiatkamjorn (2011). Behavior of geogrid-reinforced ballast under various levels of fouling. *Geotextiles and geomembranes* 29(3): 313-322.
- Indraratna, B., N. T. Ngo, C. Rujikiatkamjorn and J. Vinod (2014). Behavior of fresh and fouled railway ballast subjected to direct shear testing: discrete element simulation. *International Journal of Geomechanics* 14(1): 34-44.
- Indraratna, B. and T. Ngo (2018). *Ballast railroad design: smart-uow approach*, CRC Press.
- Indraratna, B., S. Nimbalkar and C. Rujikiatkamjorn (2012). Track stabilisation with geosynthetics and geodrains, and performance verification through field monitoring and numerical modelling.
- Indraratna, B., W. Salim and C. Rujikiatkamjorn (2011). *Advanced rail geotechnology-ballasted track*, CRC press.

- Indraratna, B., M. Singh and T. T. Nguyen (2020). The mechanism and effects of subgrade fluidisation under ballasted railway tracks. *Railway Engineering Science* 28(2): 113-128.
- Indraratna, B., N. Tennakoon, S. Nimbalkar and C. Rujikiatkamjorn (2013). Behaviour of clay-fouled ballast under drained triaxial testing. *Géotechnique* 63(5): 410-419.
- Jensen, T., S. Chauhan, K. Haddad, W. Song and S. Junge (2015). Monitoring rail condition based on sound and vibration sensors installed on an operational train. *Noise and Vibration Mitigation for Rail Transportation Systems*, Springer: 205-212.
- Jiang, Y. and S. Nimbalkar (2019). Finite Element modeling of ballasted rail track capturing effects of geosynthetic inclusions. *Frontiers in Built Environment* 5: 69.
- Joh, S.-H., N. Abd Rahman, B. Ramli and K.-H. Han (2014). Alleviation of numerical instability in geophone-based measurement of track vibrations by utilizing a priori information. *KSCE Journal of Civil Engineering* 18(5): 1351-1358.
- Johansson, A., J. C. Nielsen, R. Bolmsvik, A. Karlström and R. Lundén (2008). Under sleeper pads—Influence on dynamic train–track interaction. *Wear* 265(9-10): 1479-1487.
- Johns, T. G., S. G. Sampath, J. C. Bell and K. B. Davies (1981). *Engineering Analysis of Stresses in Railroad Rails*. Office of Research and Development, Washington, D.C., Federal Railroad Administration
- Kaewunruen, S. and A. Remennikov (2004). A state-of-the-art review report on vibration testing of ballasted track components. Australia, CRC
- Railway Engineering and Technology.
- Kaewunruen, S. and A. Remennikov (2005). In-field dynamic testing and measurements of railway tracks in Central Queensland. Australia, CRC Railway Engineering and Technologies.
- Kaewunruen, S. and A. Remennikov (2005). Integrated Field measurements and track simulation for condition assessment of railway tracks. 1st international conference on structural condition assessment, monitoring, and improvement. Perth, Australia: 391–398.
- Kaewunruen, S. and A. Remennikov (2007). Field trials for dynamic characteristics of railway track and its components using impact excitation technique. *Nondestructive Testing and Evaluation International* 40(7): 510-519.
- Kaewunruen, S. and A. Remennikov (2007). Influence of voids and pockets on vibration characteristics of railway concrete sleepers.
- Kaewunruen, S. and A. Remennikov (2007). Investigation of free vibrations of voided concrete sleepers in railway track system. *Proceedings of the Institution of Mechanical Engineers, Part F: Journal of Rail and Rapid Transit* 221(4): 495-507.

- Kokusho, T., Y. Yoshida and Y. Esashi (1982). Dynamic properties of soft clay for wide strain range. *Soils and Foundations* 22(4): 1-18.
- Kouroussis, G., O. Verlinden and C. Conti (2010). On the interest of integrating vehicle dynamics for the ground propagation of vibrations: the case of urban railway traffic. *Vehicle System Dynamics* 48(12): 1553-1571.
- Kramer, S. L. (2008). Performance-based earthquake engineering: opportunities and implications for geotechnical engineering practice. *Geotechnical earthquake engineering and soil dynamics IV*: 1-32.
- Lackenby, J., B. Indraratna, G. McDowell and D. Christie (2007). Effect of confining pressure on ballast degradation and deformation under cyclic triaxial loading.
- Lamas-Lopez, F., Y.-J. Cui, N. Calon, S. C. D'Aguiar and T. Zhang (2017). Impact of train speed on the mechanical behaviours of track-bed materials. *Journal of Rock Mechanics and Geotechnical Engineering* 9(5): 818-829.
- Lamas-Lopez, F., Y.-J. Cui, N. Calon, S. C. D'Aguiar, M. P. De Oliveira and T. Zhang (2016). Track-bed mechanical behaviour under the impact of train at different speeds. *Soils and foundations* 56(4): 627-639.
- Lambe, T. W. and R. V. Whitman (1969). *Soil mechanics*, . New York, USA, Wiley.
- Lazorenko, G., A. Kasprzhitskii, Z. Khakiev and V. Yavna (2019). Dynamic behavior and stability of soil foundation in heavy haul railway tracks: A review. *Journal of Construction Building Materials* 205: 111-136.
- Le Pen, L., D. Milne, D. Thompson and W. Powrie (2016). Evaluating railway track support stiffness from trackside measurements in the absence of wheel load data. *Canadian Geotechnical Journal* 53(7): 1156-1166.
- Lee, H. (2009). Ballast evaluation and hot mixed asphalt performance. *Proc. BCR2A Conf.*
- Li, D., J. Hyslip, T. Sussmann and S. Chrismer (2015). *Railway geotechnics*, CRC Press.
- Li, D., J. Hyslip, T. Sussmann and S. Chrismer (2016). *Railway geotechnics*, CRC Press.
- Li, D. and E. T. Selig (1998). Method for railroad track foundation design. II: Applications. *Journal of geotechnical and geoenvironmental engineering* 124(4): 323-329.
- Li, T., Q. Su and S. Kaewunruen (2019). Saturated ground vibration analysis based on a three-dimensional coupled train-track-soil interaction model. *Applied Sciences* 9(23): 4991.
- Li, Y. (2013). Research on wireless monitoring system hardware for distributed rail stress. Dalian, China, Dalian University of Technology.

- Lichtberger, B. (2010). Track compendium, Eurail Press.
- Ling, X., P. Li, F. Zhang, Y. Zhao, Y. Li and L. An (2017). Permanent deformation characteristics of coarse grained subgrade soils under train-induced repeated load. *Advances in Materials Science Engineering*.
- Liu, G., H. Liu, A. Wei, J. Xiao, P. Wang and S. Li (2018). A new device for stress monitoring in continuously welded rails using bi-directional strain method. *Journal of Modern Transportation* 26(3): 179-188.
- Liu, J. and J. Xiao (2009). Experimental study on the stability of railroad silt subgrade with increasing train speed. *Journal of Geotechnical and Geoenvironmental Engineering* 136(6): 833-841.
- Liu, S., H. Huang, T. Qiu and B. Kerchof (2019). Characterization of ballast particle movement at mud spot. *Journal of Materials in Civil Engineering* 31(1): 04018339.
- Liu., S. H., J. Gao., Y. Q. Wang and L. Weng (2014). Experimental study on vibration reduction by using soil bags. *Geotextile and Geomembranes* 42(1): 52-62.
- Lombaert, G., G. Degrande, S. François and D. Thompson (2015). Ground-borne vibration due to railway traffic: a review of excitation mechanisms, prediction methods and mitigation measures. *Noise and vibration mitigation for rail transportation systems*, Springer: 253-287.
- Lombaert, G., G. Degrande, J. Kogut and S. François (2006). The experimental validation of a numerical model for the prediction of railway induced vibrations. *Journal of sound and vibration* 297(3-5): 512-535.
- Machii, K. (1978). Mud pumping on tracks--present state and countermeasures. *Japanese railway engineering* 17(4): 20-21.
- Marschi, N. D., C. K. Chan and H. B. Seed (1972). Evaluation of properties of rockfill materials. *Journal of the Soil Mechanics Foundations Division* 98(1): 95-114.
- Mehta, C. R. and N. R. Patel (2011). *IBM SPSS exact tests*. Armonk, NY: IBM Corporation.
- Mekonnen, A. (2019). Train induced pore water pressure generation model: numerical comparison. *Journal of Vibroengineering* 21(4): 952-961.
- Melke, J. (1988). Noise and vibration from underground railway lines: proposals for a prediction procedure. *Journal of Sound and Vibration* 120(2): 391-406.
- Milne, D., J. Harkness, L. Le Pen and W. Powrie (2019). The influence of variation in track level and support system stiffness over longer lengths of track for track performance and vehicle track interaction. *Vehicle System Dynamics*: 1-24.

- Milne, D., L. Le Pen, D. Thompson and W. Powrie (2017). Properties of train load frequencies and their applications. *Journal of sound and vibration* 397: 123-140.
- Milne, D., L. L. Pen, D. Thompson and W. Powrie (2018). Automated processing of railway track deflection signals obtained from velocity and acceleration measurements. *Proceedings of the Institution of Mechanical Engineers, Part F: Journal of Rail and Rapid Transit* 232(8): 2097-2110.
- National-Instruments (2020). Measuring Strain with Strain Gages. White Papers. www.nationalinstruments.com, National instruments
- Nelson, J. (1996). Recent developments in ground-borne noise and vibration control. *Journal of sound and vibration* 193(1): 367-376.
- Noorzaei, J., P. M. Pour, M. S. Jaafar, Y. C. Fong and W. A.-M. Thanoon (2012). Numerical simulation of railway track supporting system using finite-infinite and thin layer elements under impulsive loads. *Journal of Civil Engineering and Management* 18(2): 245-252.
- O'Geen, A. T. (2013). Soil Water Dynamics. *Journal of Nature Education Knowledge* 4(5): 9.
- Öberg, J. (2006). Track deterioration of ballasted tracks-marginal cost models for different railway vehicles. Stockholm, Sweden, Royal Institute of Technology.
- Ouakka, S., O. Verlinden and G. Kouroussis (2022). Railway ground vibration and mitigation measures: benchmarking of best practices. *Railway Engineering Science*: 1-22.
- Parsons, R. L., A. Rahman, J. Han and T. E. Glavinich (2014). Track ballast fouling and permeability characterization by using resistivity. *Journal of Transportation Research Record* 2448(1): 133-141.
- Peplow, A. T. and A. M. Kaynia (2007). Prediction and validation of traffic vibration reduction due to cement column stabilization. *Soil dynamics and earthquake engineering* 27(8): 793-802.
- Quagliata, A., M. Ahearn, E. Boeker, C. Roof, L. Meister and H. Singleton (2018). *Transit Noise and Vibration Impact Assessment Manual*.
- Rabbi, M. F., R. Bruzek, T. R. Sussmann, H. B. Thompson and D. Mishra (2022). A study of vertical tie reaction forces in ballasted railroad tracks through field instrumentation and numerical modeling. *Proceedings of the Institution of Mechanical Engineers, Part F: Journal of Rail and Rapid Transit*: 09544097221089406.
- Raut, A. K. (2006). Mathematical modelling of granular filters and constriction-based filter design criteria.
- Raymond, G. (1999). Railway rehabilitation geotextiles. *Geotextiles and geomembranes* 17(4): 213-230.

- Raymond, G. P. (1986). Geotextile Application for a branch line upgrading. *Geotextiles and Geomembranes* 3(2-3): 91-104.
- Richart, E. F. (1970). *Vibrations of soils and foundations*, Printed in the United States of America.
- Rossetti, M. A. (2002). Potential impacts of climate change on railroads. *The Potential Impacts of Climate Change on Transportation: Workshop Summary*.
- Santos, J. A. and G. C. A (2000). Shear modulus of soils under cyclic loading at small and medium strain level. *12th World Conference on Earthquake Engineering*: 1-8.
- Seed, H. B., R. T. Wong, I. Idriss and K. Tokimatsu (1986). Moduli and damping factors for dynamic analyses of cohesionless soils. *Journal of geotechnical engineering* 112(11): 1016-1032.
- Selig, E. T. and D. D. Cantrell (2001). Track substructure maintenance—from theory to practice. *Proc., American Railway Engineering and Maintenance-of-Way Association Annual Conference*.
- Selig, E. T. and D. Li (1994). Track modulus: Its meaning and factors influencing it. *Transportation Research Record*(1470).
- Selig, E. T. and J. M. Waters (1994). *Track geotechnology and substructure management*, Thomas Telford.
- Singh, D. and Y. Seth (2017). 3D Modelling of ground surface vibration induced by underground train movement. *Procedia Engineering* 173: 1580-1586.
- Stark, T. D. and S. T. Wilk (2016). Root cause of differential movement at bridge transition zones. *Proceedings of the Institution of Mechanical Engineers, Part F: Journal of Rail and Rapid Transit* 230(4): 1257-1269.
- Stark, T. D., S. T. Wilk and T. R. Sussmann Jr (2015). Evaluation of tie support at transition zones. *Transportation Research Record* 2476(1): 53-58.
- Su, Z., H. Huang and G. Jing (2015). Experimental analysis permeability characteristics of fouling railway ballast. *Journal of Metallurgical Mining Industry* 7(9): 992-997.
- Suiker, A. S., E. T. Selig and R. Frenkel (2005). Static and cyclic triaxial testing of ballast and subballast. *Journal of Geotechnical and Geoenvironmental Engineering* 131(6): 771-782.
- Sun, J. I., R. Golesorkhi and H. B. Seed (1988). Dynamic moduli and damping ratios for cohesive soils, *Earthquake Engineering Research Center, University of California Berkeley*.

- Sun, Q., B. Indraratna and S. Nimbalkar (2014). Effect of cyclic loading frequency on the permanent deformation and degradation of railway ballast. *Géotechnique* 64(9): 746-751.
- Sussmann, T. R., K. R. Maser, D. Kutrubes, F. Heyns and E. T. Selig (2001). Development of ground penetrating radar for railway infrastructure condition detection. 14th EEGS Symposium on the Application of Geophysics to Engineering and Environmental Problems, European Association of Geoscientists & Engineers.
- Takatoshi, I. (1997). Measure for the stabilization of railway earth structure. *Japan Railway Technical Service* 290.
- Tamrakar, P. (2017). Evaluation of Mechanical Parameters of Contaminated Road Base and Railway Ballast, The University of Texas at El Paso.
- Tennakoon, N., B. Indraratna, C. Rujikiatkamjorn, S. Nimbalkar and T. Neville (2012). The role of ballast-fouling characteristics on the drainage capacity of rail substructure. *Geotechnical Testing Journal* 35(4): 629-640.
- Terzaghi, K. (1925). *Soil mechanics*. Vienna, Franz Deuticke.
- Thiers, G. and H. Seed (1969). Strength and stress-strain characteristics of clays subjected to seismic loading conditions. *Vibration effects of earthquakes on soils and foundations*, ASTM International.
- Thompson, D. J., G. Kouroussis and E. Ntotsios (2019). Modelling, simulation and evaluation of ground vibration caused by rail vehicles. *Vehicle System Dynamics* 57(7): 936-983.
- Thompson, I., B. Hugh, R. Alturk and D. Mishra (2022). Field Validation of Vertical Tie Reaction Force Measurement Using Rail Strain Gauges [Research Results], United States. Department of Transportation. Federal Railroad Administration.
- Thompson, I., B. Hugh, R. Alturk and D. Mishra (2022). Rail-Mounted Strain Gauges for Tie Reaction Measurement Under Dynamic Loading [Research Results], United States. Department of Transportation. Federal Railroad Administration.
- Touqan, M., A. Ahmed, H. El Naggar and T. Stark (2020). Static and cyclic characterization of fouled railroad sub-ballast layer behaviour. *Soil Dynamics and Earthquake Engineering* 137: 106293.
- Tournay, H., X. Shu and P. Rakoczy (2017). The effect of high impact wheel loads on rail fracture from transverse defects. *Proceedings of 11th International Heavy Haul Conference IHHA*.
- Trinh, V. N., A. M. Tang, Y.-J. Cui, J.-C. Dupla, J. Canou, N. Calon, L. Lambert, A. Robinet and O. Schoen (2012). Mechanical characterisation of the fouled ballast in ancient railway track substructure by large-scale triaxial tests. *Soils and foundations* 52(3): 511-523.

- Tvrdek, R. (2015). The Effect of Matric Suction on Total Stability Evaluations in Clay. TVGT.
- Tzanakakis, K. (2013). The railway track and its long term behaviour: a handbook for a railway track of high quality, Springer Science & Business Media.
- Van Genuchten, M. T. (1980). A closed-form equation for predicting the hydraulic conductivity of unsaturated soils. Soil science society of America journal 44(5): 892-898.
- Vardoulakis, I. and J. Sulem (1995). Bifurcation analysis in geomechanics. London., Blackie.
- Volberg, G. (1983). Propagation of ground vibrations near railway tracks. Journal of Sound and Vibration 87(2): 371-376.
- Vucetic, M. and R. Dobry (1991). Effect of soil plasticity on cyclic response. Journal of geotechnical engineering 117(1): 89-107.
- Wang, P., K. Xie, L. Shao, L. Yan, J. Xu and R. Chen (2015). Longitudinal force measurement in continuous welded rail with bi-directional FBG strain sensors. Smart Materials and Structures 25(1): 015019.
- Wang, Y., L.-W. Kong and Y.-L. Wang (2014). Mechanism and control of subgrade mud pumping under the cyclic load of train. 2014 International Conference on Mechanics and Civil Engineering (icmce-14). Atlantis Press.
- White, B., R. Nilsson, U. Olofsson, A. Arnall, M. Evans, T. Armitage, J. Fisk, D. Fletcher and R. Lewis (2018). Effect of the presence of moisture at the wheel–rail interface during dew and damp conditions. Proceedings of the Institution of Mechanical Engineers, Part F: Journal of Rail and Rapid Transit 232(4): 979-989.
- Wilk, S. T. (2017). Mitigation of differential movements at railroad bridge transition zones, University of Illinois at Urbana-Champaign.
- Wilk, S. T., T. D. Stark and J. G. Rose (2016). Evaluating tie support at railway bridge transitions. Proceedings of the Institution of Mechanical Engineers, Part F: Journal of Rail and Rapid Transit 230(4): 1336-1350.
- Wilson, G., H. Saurenman and J. Nelson (1983). Control of ground-borne noise and vibration. Journal of sound and vibration 87(2): 339-350.
- Wolf, H. E. (2015). Flexural behavior of prestressed concrete monoblock crossties.
- Wood, D. M. (1990). Soil behaviour and critical state soil mechanics. Cambridge, U.K, Cambridge University Press.
- Wu, B., B. An, Z. Wen, W. Wang and T. Wu (2019). Wheel–rail low adhesion issues and its effect on wheel–rail material damage at high speed under different interfacial contaminations.

Proceedings of the Institution of Mechanical Engineers, Part C: Journal of Mechanical Engineering Science 233(15): 5477-5490.

Yasuda, N. and N. Matsumoto (1993). Dynamic deformation characteristics of sands and rockfill materials. Canadian Geotechnical Journal 30(5): 747-757.

Yu, S., L. Wu-ming, T. Ji-dong, N. Ru-song and Y. Qi (2016). Analysis of subgrade soil mud pumping model. Electronic Journal of Geotechnical Engineering 21(24): 7667-7678.

Zhang, T.-W., F. Lamas-Lopez, Y.-J. Cui, N. Calon and S. C. D'Aguiar (2017). Development of a simple 2D model for railway track-bed mechanical behaviour based on field data. Soil Dynamics and Earthquake Engineering 99: 203-212.

Zhu, Y., U. Olofsson and H. Chen (2013). Friction between wheel and rail: a pin-on-disc study of environmental conditions and iron oxides. Tribology letters 52(2): 327-339.

Curriculum Vitae

Name: Majid Touqan

Post-secondary Education and Degrees: The American University of Sharjah
University City, Sharjah, United Arab Emirates
2009-2013 B.Sc. in Civil Engineering

The American University of Sharjah
University City, Sharjah, United Arab Emirates
2013-2016 M.Sc. in Civil Engineering

The University of Sharjah
University City, Sharjah, United Arab Emirates
2013-2017 M.Sc. in Engineering Management

The University of Western Ontario
London, Ontario, Canada
2017-2022 Ph.D. in Civil and Environmental Engineering

Honours and Awards: The Milos Novak Memorial Award
2019

Douglas W. Muzyka Research Fellowship
2019

William E. & Ruth Lardner Award
2021

Related Work Experience Railway Geotechnics Research Assistant
Western University & University of Illinois at Urbana Champaign -
BNSF Railway
2017-2020

Engineer in Training
Lafarge Canada Inc.
2020-2021

Engineer in Training
Orbit Engineering Ltd.
2020-2021

Engineer in Training
Peto MacCallum Ltd.
2022-Present

Publications:

Touqan, M., El Naggar, M. H., & Stark, T. D. (2022). In-situ Assessment of Track Borne Vibrations Induced by Freight Trains. *Soil Dynamics and Earthquake Engineering*, Submitted.

Touqan, M., El Naggar, M. H., & Stark, T. D. (2022). In-situ performance assessment of track superstructure on fouled railroad. *Transportation Geotechnics*, 32, 100695.

Touqan, M., Ahmed, A., El Naggar, H., & Stark, T. (2020). Static and Cyclic Characterization of Fouled Railroad Sub-Ballast Layer Behaviour. *Soil Dynamics and Earthquake Engineering*, 137, 106293.

Touqan, M., Ojiako, U., Hamdan, B., Shamsuzzaman, M., & Bashir, H. (2020). The Impact of Adopting Project Management Standards on Project Success: Evidence from the Construction Industry of the United Arab Emirates. Proceedings of the 5th North American International Conference on Industrial Engineering and Operations Management, Detroit, Michigan, USA.

El-Emam, M., & Touqan, M. (2020). Experimental Modeling of Strip Footing Adjacent to Non-Yielding Retaining Wall. *Innovative Infrastructure Solutions*, 5, 1-17.

Zhang, X., Osinski, G. R., Newson, T., Ahmed, A., Touqan, M., Joshi, D., & Hill, H. (2019). A Comparative Study of Lunar Regolith Simulants in Relation to Terrestrial Tests of Lunar Exploration Missions. Proceedings of the 50th Lunar and Planetary Science Conference, Woodlands, Texas, USA.

Touqan, M., & El-Emam, M. (2018). Behaviour of Strip Footing in the Vicinity of Non-Yielding Wall. Proceedings of the 3rd World Congress on Civil, Structural, and Environmental Engineering, Budapest, Hungary.

El-Emam, M. and Touqan, M. (2017). Response of strip footing adjacent to nonyielding basement wall. In International Congress and Exhibition of Sustainable Civil Infrastructures: Innovative Infrastructure Geotechnology. Springer, Cham, 34-45.

Touqan, M., & El-Emam, M. (2016). Responses of Non-Yielding Basement Walls Adjacent to Strip Footing. Proceedings of the 2nd International Conference on Infrastructure Management, Assessment and Rehabilitation Techniques, Sharjah, UAE.